Université de Liège
Faculté des Sciences
Département de Physique
GRASP

LIÈGE université
Sciences

Self-organization of a monolayer of magnetized beads

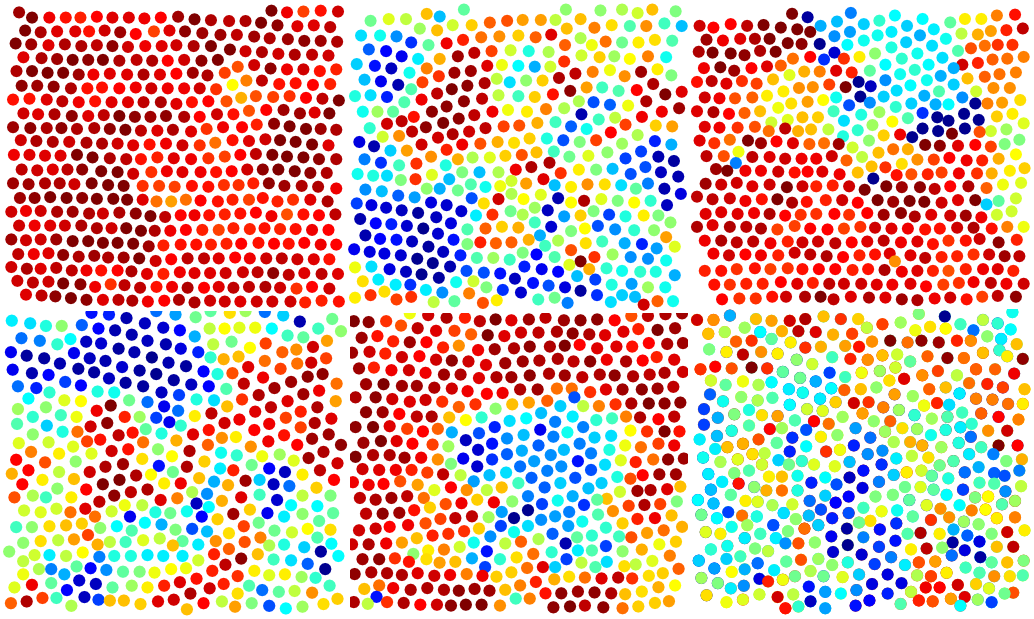

Dissertation présentée par
Julien Schockmel
en vue de l'obtention du titre de
Docteur en Sciences
Année académique 2018-2019

Tout d'abord un grand merci aux membres du jury Jean-Yves Raty, Alejandro Silhanek, Stéphane Dorbolo, Nicolas Vandewalle, Eric Falcon et René Messina pour l'intérêt porté à ce travail. Je vous remercie d'avance pour les remarques et la discussion qui suivront la lecture de ce manuscrit.

C'est donc ici que se finit ce voyage au terme duquel j'ai appris beaucoup de choses sur la physique et énormément sur moi-même. Je remercie chaleureusement chaque personne [1] qui y a contribué de près ou de loin.

Merci à Aurélie, Noah et Oscar. Nul n'est irremplaçable, sauf vous.

Sans le savoir à l'époque, l'envie de faire de la recherche est née en moi avec le cours d'un professeur dont le premier slide évoquait Pierre-Gilles de Gennes. Je souhaite logiquement conclure en le citant:

> "Le vrai point d'honneur n'est pas d'être toujours dans le vrai. Il est d'oser, de proposer des idées neuves, et ensuite de les vérifier."
>
> P.-G. De Gennes.

[1] Sauf Marti

Résumé

Nous présentons les résultats expérimentaux obtenus avec un système modèle expérimental dédié à l'étude des structures et des transitions de phases à 2D. Le système est composé d'une monocouche de billes soft-ferromagnétiques de taille millimétrique confinées dans une cellule 2D horizontale. Les billes sont plongées dans un champ magnétique vertical et homogène qui induit une interaction dipôle-dipôle entre elles. L'effet combiné du confinement et des interactions répulsives ordonne les billes. Celles-ci sont athermales, une agitation mécanique est donc utilisée afin de leur conférer un mouvement Brownien qui crée du désordre dans le système. Ajuster l'importance relative entre les effets de l'interaction et de l'agitation permet de contrôler l'ordre du système.

Grâce à ce dispositif expérimental, nous pouvons donc étudier la transition d'un état figé et très ordonné, dit cristallin, vers un état désordonné et dynamique semblable à un liquide. Nous montrons que cette transition se déroule en deux étapes, avec une phase intermédiaire appelée hexatique, comme cela est prédit par la théorie KTHNY de la fusion 2D. De plus, les structures observées sont identiques à celles obtenues à partir de systèmes colloïdaux et de simulations numériques. Notre expérience semble donc tout à fait adaptée à l'étude des systèmes 2D thermiques. Dans la suite de ce travail, nous avons décidé de nous concentrer sur l'étude des défauts topologiques car ils sont d'une importance cruciale en physique à basse dimensionnalité. Nous avons d'abord forcé les défauts topologiques dans le système en induisant une frustration venant du confinement. Nous montrons que la taille et la géométrie du confinement affectent significativement l'ordre global, ainsi que le type et le nombre de défauts observés dans le système. Ensuite, nous forçons des défauts ponctuels dans la structure en y introduisant des billes de tailles différentes, appelées impuretés. A l'échelle globale, l'augmentation du taux d'impureté permet d'empêcher la cristallisation du système. A l'échelle locale, nous observons que les impuretés induisent des frustrations géométriques très localisées, ce qui mène à l'apparition de défauts topologiques dont la nature est directement liée à la taille de l'impureté.

Abstract

We present experimental results obtained with a model experimental system dedicated to the study of 2D structures and phase transitions. The system is composed of a monolayer of millimetric soft ferromagnetic beads confined in a 2D horizontal cell. The beads are immersed in a vertical and homogeneous magnetic field inducing magnetic dipole-dipole interactions between beads. Due to the confinement, the repulsive interactions tend to order the system. As the system is athermal, a mechanical agitation is used to produce a Brownian motion of the beads which creates disorder. Adjusting the competition between the effects of the interaction and the agitation allows us to control the order of the system.

Thanks to this experimental setup, we can study the transition from a frozen and very ordered state, called a crystal, to a disordered and dynamic state similar to a liquid. As predicted by the KTHNY theory of 2D melting, a two-step transition is highlighted, including the so-called hexatic phase between crystal and liquid. In addition, the structures observed agree quantitatively with structures obtained in colloidal systems and in numerical simulations. Our experimental system is, therefore, a suitable model to study 2D thermal structures. In this work, we focus on the study of topological defects that are crucial in low-dimensional physics. We first forced topological defects into the system by inducing frustration from confinement. We show that the size and the geometry of the confinement strongly affect the global order, as well as the type and the number of topological defects observed in the systems. Finally, we force pointlike defects in the structure by introducing beads of different size, called impurities. At global scale, the increase of the impurity can prevent the crystallization. At local scale, we observe that an impurity induces a very localized geometrical frustration, which creates a topological defect whose nature is directly related to the size of the impurity.

Contents

1 Introduction

This thesis begins with one grain. What we call here a grain is a discrete piece of solid matter. Each grain has its own physical and chemical properties like size, shape, electronegativity, magnetic susceptibility, etc. However, the particularity of a grain is to be insensitive to thermal agitation, limiting its minimal size to few μm. Above this size, a single grain behaves in a very deterministic way, following Newton's equations. The true curiosity happens when we consider large assemblies of grains, they thus constitute a so-called granular material. The complex collective behavior of grains leads to very unusual properties compared to solids, liquids or gases [1]. The high number of constitutive particles and their mutual interactions make a deterministic description strictly impossible. Moreover, as thermal agitation is negligible, the granular system can not explore by itself the energy landscape to find the optimal configuration leading to stable but far from equilibrium materials. As an example, from P. G. De Gennes [2], an assembly of grain should spread into a monolayer to reach gravitational lowest energy but due to friction, grains tend to form rather a heap. By the way, the shape of the heap can be directly linked to friction coefficient between grains or other cohesive forces [3]. The usual tools of thermodynamics and statistical physics are therefore poorly adapted to granular media. Today, most of our knowledge about granular materials is empirical and valid under specific conditions. The modification of some parameters can dramatically change the behavior of the material and since there is no unified theory, the influence of each parameter must be studied case by case.

This poor global comprehension contrasts with the omnipresence of granular materials in daily life. Almost everything around you now has been once in granular form during its manufacture. The coffee you are drinking is an obvious example. Before being molded, the water bottle on your right was in the form of plastic pellet. The paper of this manuscript was originally woodchips, the words you are reading were printed using a toner that is actually powdered ink. To

reward you for the end of this reading, you will probably drink a beer brewed with malt grains and pellets of hops. As a beer brings another, the pill you'll take tomorrow for your headache is also made of compressed powder. Actually, except water, granular material is the most manipulated material in industry. Due to the huge interest of the industries, the subject has been regarded for a long time as engineering. It was not until the 90s that physicists seized the subject to study it from a more fundamental angle. Nowadays, granular materials are very popular in physics laboratories for two reasons: (i) the fundamental understanding of granular materials is far from being achieved and (ii) granular systems appear to be excellent model systems to study many others. Personally, granular systems have been a central topic for both reasons. Even if this is not the scope of this manuscript, let us just mention personal contribution to fundamental understanding of granular matter [4, 5, 6, 7, 8].

The first striking use of granular material as a model system is the sandpile metaphor to explain self-organized criticality introduced by Bak, Tand and Wiesenfeld [9, 10]. To build a sand pile, grains are added randomly one by one and slope of the heap increases until reaching its critical value which is the angle of repose. Adding a single grain can cause avalanches of any size. If the slope is initially too high, it collapses until reaching the angle of repose. Regardless of the initial conditions, the dynamics is attracted by its critical point. Actually, this phenomenon is typical of dissipative systems and thus is widely observed in nature or in society: semiconductors [11], superconductors [12], superfluids [13], ferromagnetic materials [14, 15], earthquake [16], population dynamics [17], neuroscience [18] and many others. However, the self-organized criticality in granular material has been debated because it was not systematically observed in granular experiments [19, 20], but whatever, because the idea of using granular materials to model complex systems entered in the minds of the physicists. Experiments in granular compaction pointed out that a slow relaxation process due to vibration is similar to disordered and frustrated systems like glasses and spin glasses [19, 21, 22, 23, 24]. More than the similarity about the relaxation times, glasses and excited granular systems share a phenomenologically similar transition: the rigidity increases and leads to an out of equilibrium freezing in a disordered state respectively called glass transition and jamming transition [25, 26, 27]. This observation is very surprising and counterintuitive because the nature of the two systems are fundamentally different: unlike a supercooled liquid, the granular system is athermal and dissipative. We can then ask this question: does the external agitation play a role similar to temperature?

Basically, one can just define a granular temperature proportional to the mean kinetic energy of the grains but comparing it to a molecular gas is not trivial at all due to inelastic collisions. Beside other exotic phenomenons like clustering or segregation, the dissipative behavior leads to non-Gaussian velocity distribution. To

maintained a non-equilibrium steady-state, energy must be continuously injected to compensate loss by collisions. If not, the system becomes progressively cool until dynamics stops. Moreover in 3D experiments, the external excitation is usually performed by vibrating boundaries and consequently the more a particle moves away from the container walls, the more it loses kinetic energy due to inelastic collisions thus the system can not be uniformly heated. To our knowledge, only one 3D experiment with uniform heating has been done [28]. But an additonnal problem with experimental 3D granular gas is the impossibility to track efficiently each particle's trajectories. Luckily, these 3D issues can be easily bypassed using a shaken horizontal monolayer of grains, called abusively 2D granular gas. First, using a simple camera it is possible to track each particle during all the time of the experiment. Then, the energy is injected by the substrate on which each particle lays, they are thus identically excited [29, 30, 31, 32, 33, 34]. The feature that particularly catches our attention is that, under appropriate agitation, a 2D granular steady-states system apparently behaves like thermal systems in equilibrium despite its deep out-of-equilibrium nature. However, note that these 2D granular gases display a non-gaussian velocity distribution due to inelastic collisions.

A careful study of the transition from hexagonal crystal to granular gas in a vibrated monolayer of beads [35, 36] pointed out a striking observation: the transition observed is perfectly reproduced by numerical simulations of an idealized 2D hard disks system in equilibrium [37] and consistent with the theory of 2D melting. One can therefore conclude that a uniformly agitated monolayer of beads is an excellent model system for studying 2D phases and transitions at equilibrium. Furthermore, it appears that the most important ingredient to make the analogy is not the energy conservation but the uniform injection of energy [36]. Note that this uniformly heated granular system also models successfully the complex behavior of glasses using polydisperse beads (glass transition, dynamic heterogeneities and Gardner transition) [27, 38, 39], liquid crystals using vibrated rods [40, 41], polymeric structure using granular chains [42].

The experiment presented in this thesis is built on the basis of 2D uniformly heated granular system. The difference with hard spheres systems previously described is the use of a repulsive and conservative pair interaction between beads leading to a quasi-elastic regime where the energy is only lost by contact with the substrate. Such a system with proper agitation exhibits a diffusive behavior as expected but also a Gaussian velocity distribution. The pair interaction, which is a magnetic dipole-dipole interaction, is tunable by an external magnetic field allowing us to control the stiffness of the bonds and thus go from a liquid-like to a crystal-like system.

The interest of granular systems for modeling 2D structure is now a matter fact. The 2D physics can, by many ways, be very different from 3D's. In the early 1970s, since the work of Mermin and Wagner [43, 44], who rigorously demonstrated the absence of long-range order in low-dimensional systems due to strong thermal fluctuations, it was thought that there was no transition to a finite-temperature ordered state. Kosterlitz and Thouless tackled this issue by introducing the new concepts of topological phase transitions and topological phases of matter where topological defects play a crucial role [45, 46]. At low temperature, defects are not free but assembled such that the system still presents a look alike order. When temperature increases, the loss of order is driven by defects behavior. In their former article, it was question of XY model, a two-dimensional spin lattice whose vector is contained in the plane and can take any orientation. Topological defects are there spin vortices. At low temperature, two opposite rotation vortices are paired and above the transition, isolated vortices proliferate. This is called Kosterlitz-Thouless (KT) transition. The powerful feature of this transition is its universality as it is observed in many 2D systems which are of different nature. Indeed, the KT transition perfectly describe the superfluid transition in thin film of He [47, 48] or in quasi-2D Bose-Einstein condensates [49], the loss of superconductivity in thin superconducting films [50, 51] and many other [52, 53, 54, 55]. This theory has been extended later by Halperin, Nelson and Young to propose the melting theory of 2D crystals [45, 46, 56, 57, 58] mentioned previously. This theory is detailed in Sec. 5.2 but in a few words the Kosteritz-Thouless-Halperin-Nelson-Young (KTHNY) theory predicts a two-stage melting mediated by topological defects, with an intermediate anisotropic liquid phase called hexatic. The KTHNY theory has been a matter of debate for a long time due to lack of experimental evidences. But thanks to the extensive experimental work of Maret's group who use magnetic colloids to model 2D crystals [59, 60, 61, 62, 63, 64], the consensus is now clear and the theory is widely accepted. The KTHNY also presents a universal feature as it has been observed in many experiments of different natures: colloids, granulars, block copolymers [65], ferrofluid [66].

Our experimental set-up is dedicated to the study of 2D systems. Consequently, the transition from liquid to crystal that we observe experimentally must be confronted to the KTHNY theory of melting. Using static and dynamic order parameters, we are able to identify the signature of the double transition and the hexatic phase is observed. We conclude that our experiment is an efficient model system to study 2D physics [67, 68].

But the study of 2D physics is not limited to melting. Far from it, the study of 2D materials is booming since the first synthesis of graphenes in 2004 by Geim and Novoselov [69]. The enthusiasm of the scientific community for this material is due to its exceptional properties: flexibility, mechanical resistance, conductivity, transparency, etc. However, lattice imperfections are inevitable during the graphene processing but impact significantly the properties of graphene which can be whether altered or improved [70, 71]. Indeed, defects decrease the thermal and electrical conductivity but increase the elasticity and modify the bandgap which is useful in the case of the use of graphene in electronics. Briefly, if you control the defects, you control the properties but the links are still poorly understood and more works are mandatory to improve defect engineering. A priori, the link between the structure and the electronic properties is specific to graphene, but graphene is just a famous example of 2D crystalline membrane. Thus, as suggested by the KT transition universality, we expect that the link between structure, geometry and defects also has universalities for all kind of 2D materials or considered as such. Defects appear naturally due temperature but are also the consequence of frustrations. In membranes, one can find (i) out-of-plane frustrations, (ii) boundaries frustrations or (iii) pointlike frustrations (iii).

(i) - One characteristic of membranes is the fact that they are not necessarily constrained in the plan and thus topological defects and curvature are reciprocally linked. The topography influences defects: if you want to make a football using hexagons, you imperatively need pentagons to close the sphere. But defects also influence the topography. Basically, a single defect can buckle a membrane in a conical shape or saddlelike shape but the sum of the deformations due to a large number of defects gives a complex morphology observed in lipid bilayer [72] or graphene [73, 74] for example.

(ii) - Systems composed of few hundreds of particles or less are far from

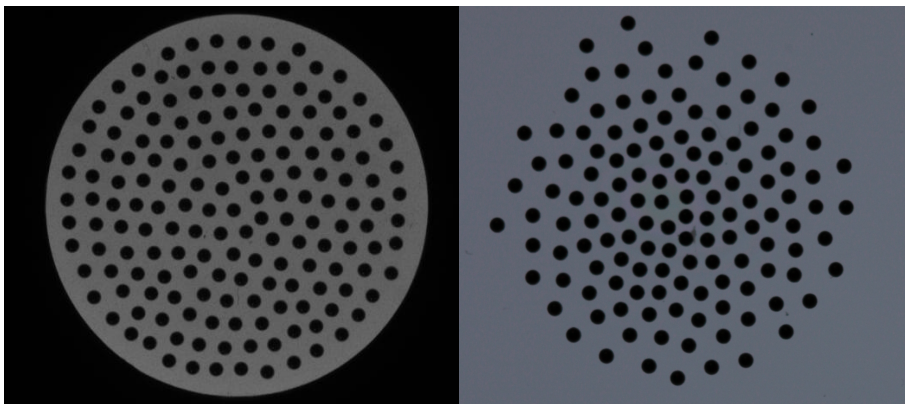

Figure 1.1 – Left - Hard confinement. Right - Soft confinement

the thermodynamics limit, thus finite size and boundaries effects are significant and their combined effects modify phase diagram, dynamics and structures [75, 76, 77, 78]. The question of the effect of confinement on crystals is aroused, among other, by the emergence of nanotechnologies, in particular of hollow nanostructures. For example, it is now possible to freeze water in nanoporous materials [79, 80, 81, 82, 83] and as expected, the phase diagram is unusual. Even though confined systems are more and more observed but they are far from being fully understood, especially the microscopic mechanisms leading to a change of behavior under confinement. Fundamentally, only two types of containment are retained here: adaptative boundaries or solid boundaries also called soft wall and hard wall respectively. Under a soft confinement, the boundaries adapt to the symmetry of the crystal and the shape of that finite crystal is dictated by topological defects inside[84]. On the contrary, in hard confinement, the confining geometry dictates the order of the crystal at boundaries. If this geometry is not commensurate with natural order of the crystal, it induces frustrations in the system that is causing topological defects and thus modify so the physical properties of the confined material.

Our experimental model system appears to be very suitable to study the role of boundaries frustrations on the order of the system because due to repulsive interaction between beads, a spatial confinement is mandatory. Therefore, we perform a systematic study of the organization of the system under various geometries of hard confinement. Triangular, square, pentagonal, hexagonal, heptagonal and circular geometries are tested and it appears that cell geometry strongly affects the ordering of the system. Moreover, many kinds of defects, whose observation rate is linked to the geometry, are observed: disclinations, dislocations, defects chain, and also more exotic defects. The influence of confinement size is also investigated, and we point out that no finite size effect occurs for a hexagonal cell but the finite size effect changes from a geometry to another [85].

(iii)- A point defect is a local disturbance due to a misposition of a particle in regards to the ideal lattice. Defect is either intrinsic or extrinsic. An intrinsic defect appears spontaneously in pure crystals due to thermal agitation or stresses. They are inherent to natural materials and even occur at low temperature. An extrinsic defect is forced by the introduction of a foreign particle, an impurity, that is characterized by different properties than regular particles of the crystal like mobility, size or interaction strength. Consequently, interdistances are modified near the impurity which generates a local geometrical frustration inducing a topo-

logical defect. These defects are naturally present in materials because perfectly pure crystals are rare. Moreover, impurities are positively used in many industrial applications to modify properties of a material like the doping of semiconductors or alloys manufacturing. In classical systems like colloidal or granular media, extrinsic defects are actively introduced using polydispersity. Nowadays, these systems are essentially used to study glassy behavior because introducing enough defects can prevent crystallization [86] even at low temperature or high density when the dynamics is frozen. One can also use this polydispersity or basically bidisperse systems, to study the structural and geometrical impact of topological defects on the order of a crystal.

To close this thesis, we study the influence of pointlike frustrations on a 2D crystal. To this purpose, we use binary mixture made of big and small beads. In this experiment, big beads are step by step replaced by small beads, and we observe that the global order of the system decreases. The order is at its lowest when there are as many small beads as big beads. This tendency is quantified using a model, freely inspired of an Ising model, that allows us to understand the mechanisms behind the loss of order. We also investigate the local geometrical frustration induced by a different sized bead. We find that statistically, topological defects carried by big beads are not the same than defects carried by small beads. This fact means that the nature of a defect can be tuned by the size of an extrinsic defect. Finally, it is shown that when a single defect is introduced, the lattice undergoes a series of local elastic deformations to restore order.

Outline

Each chapter of this manuscript aims to be self-consistent. Many points are therefore regularly recalled.

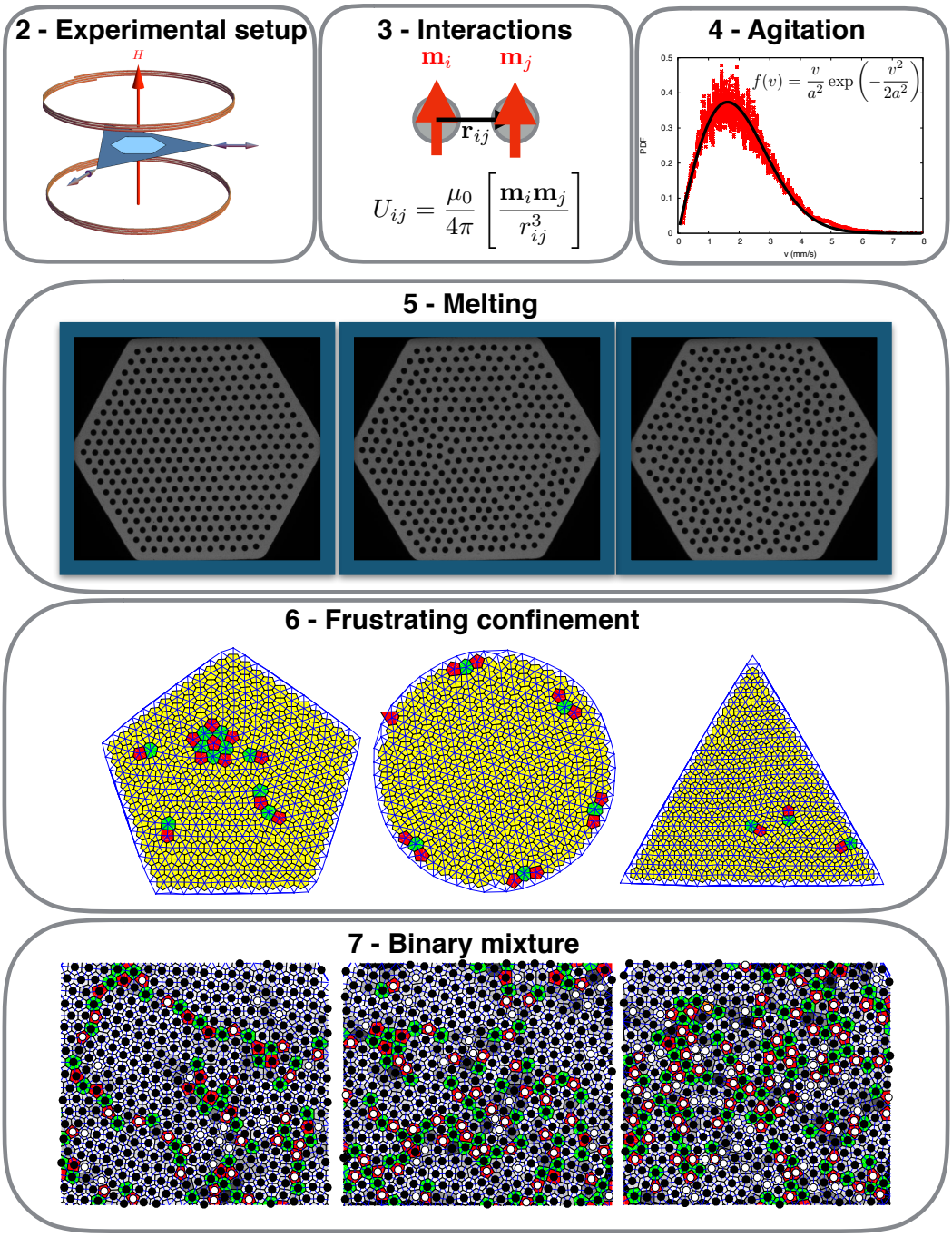

2 Experimental setup

2.1 General overview

The sketch of the experimental setup is presented in Fig 2.1. A set of spherical soft ferromagnetic beads, whose size and number can be chosen, is placed on a rough glass plate and confined in a 2D horizontal cell with ferromagnetic walls. The thickness of the cell is close to the size of the bead such as no overlap between two beads is possible, they therefore form a monolayer. The horizontal monolayer of beads is immersed in a vertical and homogeneous external magnetic field H_0 which induces a repulsive magnetic dipole-dipole interaction between the beads and between the beads and the walls. The repulsion spreads the beads until filling all the free space. The set of beads presents then a self-organized structure whose order is tunable by adjusting the strength of the external magnetic field H_0. The cell is horizontally excited by two perpendicular electromagnetic shakers. This agitation is communicated to the beads by the glass plate which induces an erratic motion of the beads. A camera at the top of the setup records the position of each bead along the time. With a suitable frame rate, one can track the beads during the experiment and gets the positions and velocities at each time. Depending on the measurement to be performed, a specific protocol is defined. All measurement can be automatized using a Labview routine.

2.2 Beads

The beads used are spherical and made of AISI 52100 chrome steel having a density $\rho = 7800$ kg/m^3. In most experiments presented here, the selected diameter is $\sigma = 1$ mm giving a volume $V = 5.23 \times 10^{-10}$ m^3 and a mass $m = 4.07 \times 10^{-6}$ kg. In industry, these beads are mainly used in ball bearings for their high precision of their sphericity, an error of 0.08μm is certified by the manufacturer, but we selected

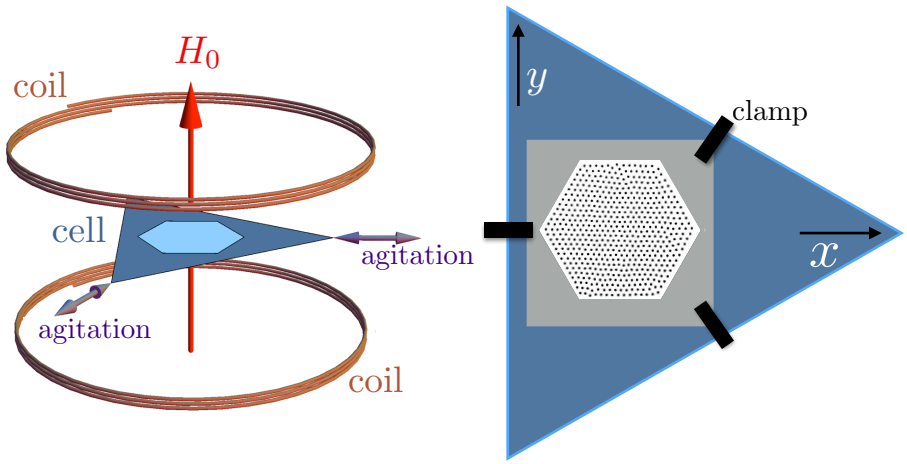

Figure 2.1 – (Left) Sketch of the experimental setup composed of two coils used to produce a vertical homogeneous magnetic field H_0. (Right) Horizontal cell, filled with soft-ferromagnetic beads, agitated by two perpendicular shakers.

them for their magnetic properties. Fig. 2.2 represents the magnetization M of one single bead in response to an external magnetic field H_0 at room temperature, namely the magnetization curve. The magnetization of a bead presents a linear response to the external magnetic field

$$M = \chi H_0, \tag{2.1}$$

for $|H_0| < 0.5 \times 10^5$ A/m. In this range, the slope is the effective susceptibility of the bead ans is found to be $\chi = 3$. As detailed in Sec. 3.2, χ is linked to the relative magnetic permeability of the material μ_r and for a uniformely magnetized sphere,

$$\chi = 3\frac{\mu_r - 1}{\mu_r + 2}. \tag{2.2}$$

Actually, $\chi = 3$ is the limit value corresponding to a sphere made with a high relative magnetic permeability material. Let us also notice that the magnetization saturates when $H_0 > 0.7 \times 10^5$ A/m. In all experiments performed, we use an external magnetic field lower than this value. The saturation of the magnetization for such a value and the high relative magnetic permeability are the signature of a ferromagnetic material. But usually ferromagnetic materials do not present this linear response but rather a hysteretic behaviour, meaning that AISI52100 chrome steel corresponds to a kind of material called *soft ferromagnetic*.

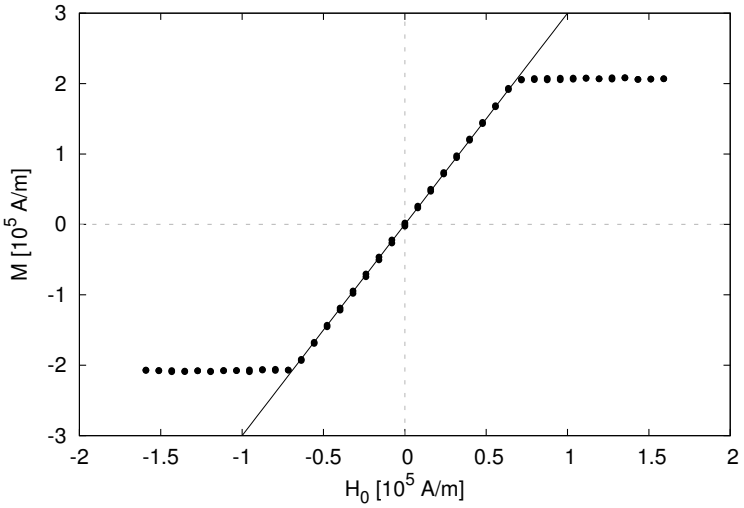

Figure 2.2 – Magnetization M of one bead in function of an external magnetic field H_0. The line whose slope is equal to 3 corresponds to the fit of the linear region of this magnetization curve.

2.3 External magnetic field

The external magnetic field H_0 in which the beads are immersed is produced by two similar N-turn circular coils of radius R in Helmholtz configuration. In this configuration, the two coils are placed symmetrically along a common axis passing through their center. The coils are separated by a distance h equal to the radius R. The same direct current I flows in each coil in the same direction. The magnetic field produced at each point of the space by the two coils can be estimated using the Biot and Savart law. We performed this calculation to determine rigorously the area where the magnetic field can be considered as homogeneous. For that, we consider a cartesian coordinate system xyz centered at a distance $R/2$ of each coil along the common symmetry axis. In the yz plane,

$$H_x(y,z) = 0, \tag{2.3}$$

$$H_y(y,z) = \frac{INR}{4\pi}\left([(z-R/2)\int_0^{2\pi} \frac{\sin\phi d\phi}{[R^2+y^2+(z-R/2)^2-2yR\sin\phi]^{\frac{3}{2}}} + (z+R/2)\int_0^{2\pi} \frac{\sin\phi d\phi}{[R^2+y^2+(z+R/2)^2-2yR\sin\phi]^{\frac{3}{2}}} \right) \tag{2.4}$$

and

$$H_z(y,z) = \frac{INR}{4\pi}\left(\int_0^{2\pi} \frac{(R - y\sin\phi)d\phi}{[R^2 + y^2 + (z - R/2)^2 - 2yR\sin\phi]^{\frac{3}{2}}} + \int_0^{2\pi} \frac{(R - y\sin\phi)d\phi}{[R^2 + y^2 + (z + R/2)^2 - 2yR\sin\phi]^{\frac{3}{2}}}\right). \quad (2.5)$$

The magnetic field at the center of the system is purely vertical because $H_y(0,0) = 0$ and

$$H_z(0,0) = H_0 = \left(\frac{4}{5}\right)^{\frac{3}{2}} \frac{NI}{R}. \quad (2.6)$$

Fig. 2.3 represents the mapping of the magnetic field obtained by solving numerically Eqs. (2.4) and (2.5) for coils with a radius $R = 0.095$ m, a number of turns $N = 155$ and carried by a current $I = 12$ A. In this configuration, $H_0 = 14000$ A/m. Colors correspond to the magnitude of the magnetic field, and the arrows indicate the direction of the field. The red contour marks the region in betwen the coils where the fluctuations of H_y and H_Z are less than 1% of H_0. As we ensure that the monolayer of beads is confined in this region, we can properly consider that the beads are immersed in a homogeneous magnetic field of magnitude H_0. Approximatively, the width of this area corresponds to the radius of the coils.

In this work, two different configurations have been used. The very first coils used have a radius $R = 0.065$ cm and $N = 320$ turns. The copper wire used to make these coils is thin enough to allow a large number of turns in a small radius. But consequently, the resistance of the wire is high and the intensity of the current in the coil is limited due to a substantial joule effect. For these coils, the maximum current used is $I_{max} = 5$A and for no longer than 3 minutes to avoid overheating. With this configuration, it is possible to reach a homogeneous magnetic field with a magnitude of 17600 A/m but the beads must be confined in a cell whose diameter is less than 0.065m. Thus, to study larger systems, we made new larger coils, of radius $R = 0.095$m, able to generate a magnetic field of magnitude comparable to the previous coils. To find such a compromise, we used copper wire with a larger diameter, and we only made $N = 155$ turns, limiting the resistance of the coil and allowing us to use a current that can reach $I_{max} = 12A$ for more than 6 minutes without overheating which can cause the melting of the insulating coating. With such a configuration, the homogeneous magnetic field has a maximum magnitude of 14000 A/m. The DC current in the coils is provided by a *Keithley 2260B* DC power supplies, this device is programmable and is driven by a Labview routine. This power supply has a constant current mode, meaning that even if the resistance of the coils increases due to the heating, the voltage is automatically adjusted guaranteeing the stability of the current and thus the magnetic field.

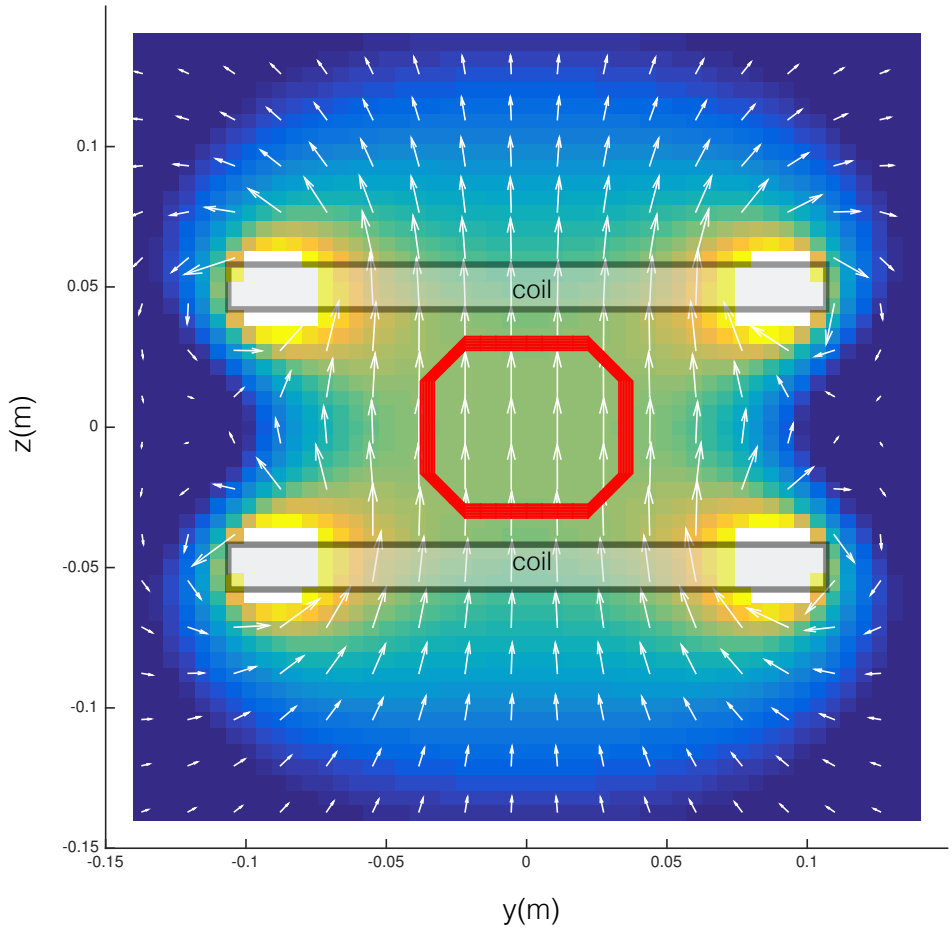

Figure 2.3 – Colormap of the magnetic field produced by two Helmholtz coils. Colors indicate the magnitude of the magnetic field, and the arrows indicate the direction of the field. The red outline delimits the region in which the magnetic field fluctuates by 1% from its center value H_0. Chosen parameters are $R = 0.095$ m, $N = 155$, $I = 12$A.

2.4 Confinement

Theoretically, under a magnetic field, the beads are supposed to repel each other to infinity, hence the importance of keeping the set of beads in a confined surface. In that case, the beads repel each other until all the free space is occupied. As beads interact by a central force, they minimize their energy by self-organizing in a hexagonal lattice. Therefore, the combination of repulsion and confinement creates order in the system. The walls of the cell are magnetizable and so repulsive to avoid inelastic collisions between beads and the cell, preventing thus clusters of

beads at the edges.

In practice, the confinement cell is machined within a square steel sheet of 10 cm on the side and 1 mm thick. For all the works presented here, a large number of cells have been machined of different size or geometry in order to meet the specific needs of the experiments performed. Fortunately, the repulsive walls are such that, in any case, beads are distributed homogeneously within the cell. To illustrate it, the cumulated radial distribution of the particle number $N(r)$ in function of the distance r from the center of the cell is presented in Fig. 2.4 for different geometries of the cell (hexagonal, square, pentagonal, heptagonal, and circular). Data presented here are all obtained with identical filling fraction and external magnetic field. The quadratic behaviour of $N(r)$, pointed out by the black curve, ensures that the beads are homogeneously distributed, whatever the geometry of the confinement.

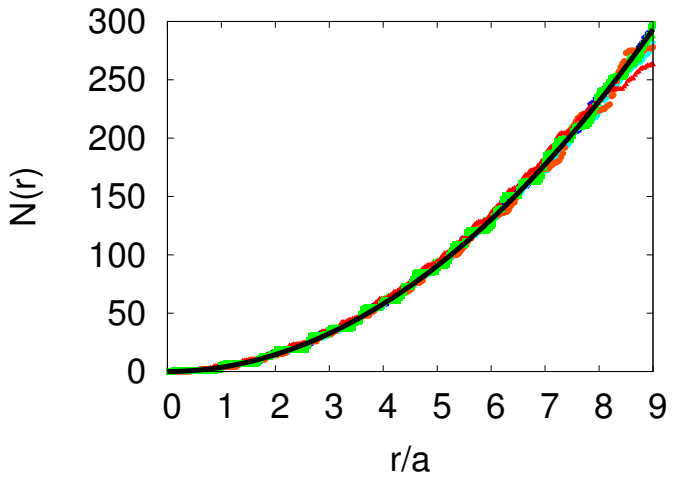

Figure 2.4 – Cumulated radial distribution of the particle number $N(r)$; the black curve corresponds to an ideally homogeneous distribution. The distance r from the center is normalized by the mean distance a between two beads in the system.

The bottom of the cell is a rough surface made of a sandblasted glass plate. This surface is selected for its rigidity, to avoid vertical deformation of the cell, and its roughness, to optimize the impulsion transfer from the vibrating plate to the beads. With a smooth bottom surface, frictions with beads are weak, so they slip over the surface and the motion of the vibrating plate is not correctly communicated to the beads. The role of the rough surface is thus essential. Moreover, since the experiment is illuminated from the bottom, sandblasted glass has the advantage to diffuse the light efficiently, improving the quality of the images. The top of the cell is made of a simple transparent glass plate to confine the beads in

the same horizontal plane. The top is not free because when the magnetic field is high, the beads can overlap vertically and form vertical structures. The gap between the layer of beads and the top glass plate is approximately 10 % of a bead diameter.

The entire structure of the cell is placed on a flat plexiglass support, thick enough to be rigid and to avoid parasite waves due to deformation. This support is fixed in 3 points, each mounted on a structure whose height is adjustable using a micrometric screw. Adjusting the height of these three points allows to adjust the horizontality of the cell. Unfortunately, the beads are much more sensitive to horizontality than any of our levels. Thus, in order to adjust the horizontality, the cell is filled with beads, the magnetic field and the agitation are switched on, then the micrometric screws are adjusted until the area density of beads appears homogeneous and stationary.

2.5 Mechanical agitation

The role of the mechanical agitation is to produce an erratic motion of the beads similar to a thermal agitation. For that purpose, the cell is attached with clamps on a triangular plexiglass support (see Fig. 2.1) subjected to horizontal vibrations. These are generated by two electromagnetic shakers *SignalForce GW-V2*. Both shakers are mounted to produce horizontal agitation, and their relative orientation is such that their axis of agitation are perpendicular. Two corners of the plexiglass support are directly screwed at the output of the shakers. The third corner is left free, to reduce mechanical stress on the shakers, and rest on a rubber block to damp vertical residual vibrations. The input voltage in the amplifier of each shaker is generated by a function generator *Tektronix AFG 3022*. The function generator is itself driven by a Labview routine with which the waveform of the input is computed. The input of each shaker is a sinusoidal function modulated in amplitude by a red noise $\eta(t)$, whose power spectral density decays as $1/\omega^2$,

$$x(t) = (A + \eta_x(t)) \sin(2\pi f t), \tag{2.7}$$

$$y(t) = (A + \eta_y(t)) \sin(2\pi f t) + \phi). \tag{2.8}$$

This waveform and the appropriate amplitude A, frequency f and phase ϕ, which induce erratic motion of the beads, has been found empirically after many tests. It is not excluded that other functions are also effective. We must use an empirical approach because the relationship between the parameters of vibration and the motion of the beads is not explicit at all. Indeed, the inertia of the beads, the roughness of the bottom of the cell and all the mechanical stresses of the experiment constantly inject mechanical noise into the cell which is not commensurable. The amplitude modulation of the signal by a noise enables to accentuate

this effect. All these mechanical constraints are actually very useful to generate an erratic movement of the beads. In Chapter 4, we show how close this agitation mimics a thermal agitation. The negative part of this random mechanical noise is that the characterization of the motion of the beads must be done a posteriori on the basis of the analysis of the images. Moreover mechanical constraints are not under control and can change from a set of experiments to another. Thus, it makes a calibration curve useless, and the motion of the beads must be characterized before each set of experiments. Despite the poor understanding of the effect of the vibration on the beads, we still observe some tendency. An increase in amplitude A is correlated with an increase in the mean kinetic energy of the beads. The isotropy of the agitation is obtained by adjusting the phase ϕ. Finally, it is observed that the mechanical response of the system to the excitation is always maximum at a frequency $f = 35$Hz, which is the frequency used in each experiment.

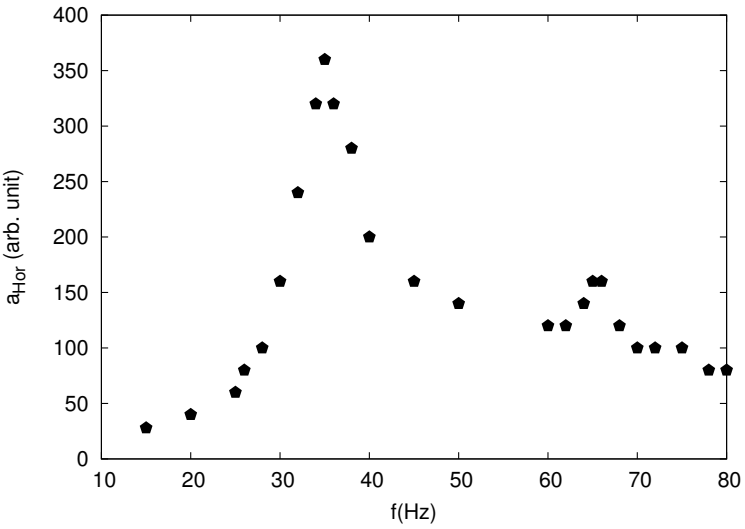

Figure 2.5 – Horizontal acceleration of the cell recorded with an accelerometer, as a function of the excitation frequency f at constant amplitude A and phase ϕ. The mechanical response of the setup is maximum at 35 Hz.

2.6 Image acquisition and processing

Image acquisition is done with a camera mounted vertically above the cell, on a structure independent of the rest of the system. In this thesis, two different cameras have been used. The first camera used is a *Thorlabs* CCD camera that

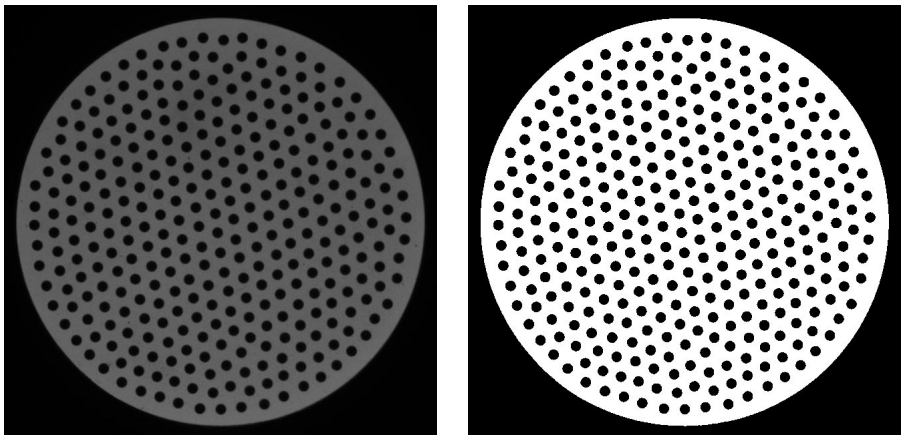

Figure 2.6 – (Left)Raw image. (Right) Binarized image.

allows a resolution of 1024 × 1024 pixels and a maximum acquisition frequency of 15 Hz. The second camera used is a high speed camera *IDT NX4* with an identical resolution and a maximum acquisition frequency of 1000 Hz. Most of the experiments has been performed with the *Thorlabs* camera. The frequency of acquisition may seem low but it is enough to track precisely the trajectory of each bead in the system and allow us to make data acquisitions over period of several minutes. The high speed camera is used to study phenomena that appear at shorter times, such as the transition between the ballistic and diffusive regime predicted by the Langevin equation and detailed in Chapter 4. The ideal time step to measure the velocity of the particles corresponds to this characteristic ballistic-diffusive transition time, so if this time is less than 1/15th of a second, the measurement of the particle velocity must be done with the high speed camera. However, in most experiments, 15 fps are largely sufficient, as demonstrated by the quantitative agreement obtained with the numerical simulations performed by Messina *et al.* [68].

Images are then processed using the *ImageJ* software. First of all, the images are binarized. Thanks to intense and diffuse lighting coming from below the cell, raw images have a good contrast, the loss of information during the application of the threshold is thus limited as shown in Figure 2.6.

Then the center of each bead is determined using a centroid algorithm. This is a simple algorithm that consists of calculating the barycenter of all the pixels that constitute the image of the bead.

$$x_c = \frac{\sum w_i x_i}{\sum w_i} + \frac{1}{2}, \tag{2.9}$$

$$y_c = \frac{\sum w_i y_i}{\sum w_i} + \frac{1}{2}. \tag{2.10}$$

The sum carried out over all the pixels of the image of the bead and (x_i, y_i) and w_i are respectively the position and the weight of the ith pixel. The weight corresponds to the intensity of the pixel but as the image is thresholded, the weight w_i is equal to 0 or 1 only. As the coordinate of a pixel is given by its top left corner, the term 1/2 is added to consider the center of the pixel. The estimation of the error on the position depends on many factors such as the spatial resolution (sampling), the number of grey levels (quantization) and the thresholding. From the work of Patwardhan [87], for an object with a radius of about 10 pixels, one can expect an error that can reach 0.01 pixel corresponding to an error of 0.0005 mm.

With the position of each bead on each image, we can only measure structural and static parameters like the pair correlation function. If we want to access to the dynamics of the system, like the mean square displacement, we need to know the trajectories of each particle. To that end, we use a tracking algorithm to reconstruct the trajectories of each particle. The tracking algorithm consists in comparing the position of the particle i in an image k with the position of each particle in the image $k+1$. The particle in the image $k+1$ whose distance with the particle i in the image k is the shortest is therefore considered as the particle i in the image $k+1$. This algorithm is reliable if the displacement of a particle between two images is much smaller than the diameter of a particle and if the number of particles is constant over time.

3 Interactions

3.1 Dipole-dipole interaction

Basically, a dipole is a system composed of two separated poles. In electromagnetism, there are two kinds of dipoles: electrical and magnetic dipole. The electrical dipole is easier to understand intuitively. Indeed, the two poles are two opposite charges, $+q$ and $-q$, separated by a distance d. At each point of the space, the electrical fields produced by these charges are

$$\boldsymbol{E}_+(\boldsymbol{r}_+) = \frac{q\hat{\boldsymbol{r}_+}}{4\pi\epsilon_0 r_+^2}, \tag{3.1}$$

$$\boldsymbol{E}_-(\boldsymbol{r}_-) = -\frac{q\hat{\boldsymbol{r}_-}}{4\pi\epsilon_0 r_-^2}. \tag{3.2}$$

Thus, the total electrical field produced by the dipole is the superposition of Eqs. (3.1) and (3.2) and after a few operations, it can be written

$$\boldsymbol{E}(\boldsymbol{r}) = \frac{1}{4\pi\epsilon_0}\left(-\frac{\boldsymbol{p}}{r^3} + \frac{3(\boldsymbol{p}\cdot\boldsymbol{r})\cdot\boldsymbol{r}}{r^5}\right) \tag{3.3}$$

where the vector $\boldsymbol{r}$ has its origin at the center of mass of the dipole and the electric dipole moment is introduced and is defined as $\boldsymbol{p} = q\boldsymbol{d}$ where $\boldsymbol{d}$ is the vector linking the negative charge to the positive charge.

The magnetic dipole is less intuitive because magnetic monopoles do not exist. This statement is mathematically translated in the Maxwell's equations by the Gauss law for magnetic field $\boldsymbol{\nabla}\cdot\boldsymbol{B} = 0$. This law means that the net magnetic flux through a closed surface is proportional to the net magnetic charge within that closed surface which is actually equal to zero. However, one can still consider a physical object composed of two opposite poles associated to a hypothetical magnetic charges $+q_M$ (noth pole) and $-q_M$ (south pole) whose net sum is zero.

These supposed magnetic charges would produce at each point of the space a magnetic field

$$\boldsymbol{B}_+(\boldsymbol{r}_+) = \frac{\mu_0 q_M \hat{\boldsymbol{r}_+}}{4\pi r_+^2}, \tag{3.4}$$

$$\boldsymbol{B}_-(\boldsymbol{r}_-) = -\frac{\mu_0 q_M \hat{\boldsymbol{r}_-}}{4\pi r_-^2}. \tag{3.5}$$

The superposition of Eqs. (3.4) and (3.5) give the magnetic field produced by the magnetic dipole

$$\boldsymbol{B}(\boldsymbol{r}) = \frac{\mu_0}{4\pi}\left(-\frac{\boldsymbol{m}}{r^3} + \frac{3(\boldsymbol{m}\cdot\boldsymbol{r})\cdot\boldsymbol{r}}{r^5}\right) \tag{3.6}$$

with $\boldsymbol{m} = q_M\boldsymbol{d}$, the magnetic dipole moment. Note that, using the Biot and Savart law, it is found that the magnetic field produced by a current loop is identical to (3.6) if the magnetic moment is defined as $\boldsymbol{m} = S\hat{n}i$ where S is the surface of the current loop, $\hat{n}$ the normal vector of the surface and i the current in te loop. Thus, two different interpretations of the magnetic dipoles can be done. The Coulombian approach where the magnetic dipole is made of a north pole and a south pole. The Amperian approach where the magnetic dipole is made of current loop. The two approaches are described by the same equations and are therefore equivalent.

When a magnetic dipole is immersed in an external magnetic field, the net force acting on the dipole is

$$\boldsymbol{F} = \boldsymbol{\nabla}(\boldsymbol{m}\cdot\boldsymbol{B}). \tag{3.7}$$

This force being conservative, the associated potential energy is

$$U = -\boldsymbol{m}\cdot\boldsymbol{B}. \tag{3.8}$$

Note that in a uniform external field, the net force is zero and there is only a torque acting on the dipole which has the effect of aligning the moment of the dipole to the external field.

The interaction between two magnetic dipoles corresponds to the potential energy of a magnetic dipole, of moment $\boldsymbol{m_1}$, immersed in the magnetic field produced by another magnetic dipole of moment $\boldsymbol{m_2}$. Using Eqs. (3.6) and (3.8), the interaction can be written

$$U(\boldsymbol{r}) = \frac{\mu_0}{4\pi}\left(\frac{\boldsymbol{m_1}\cdot\boldsymbol{m_2}}{r^3} - \frac{3(\boldsymbol{m_1}\cdot\boldsymbol{r})(\boldsymbol{m_2}\cdot\boldsymbol{r})}{r^5}\right) \tag{3.9}$$

The vector $\boldsymbol{r}$ connects the center of the two dipoles. If the dipoles are oriented along the same direction (see Fig. 3.3), Eq. (3.9) becomes

$$U(r) = \frac{\mu_0 m_1 m_2}{4\pi r^3}\left(1 - 3\cos^2(\theta)\right), \tag{3.10}$$

where r is the distance between the centers of the two dipoles and θ is the angle between $\boldsymbol{m_1}$ (or $\boldsymbol{m_2}$), and $\boldsymbol{r}$.

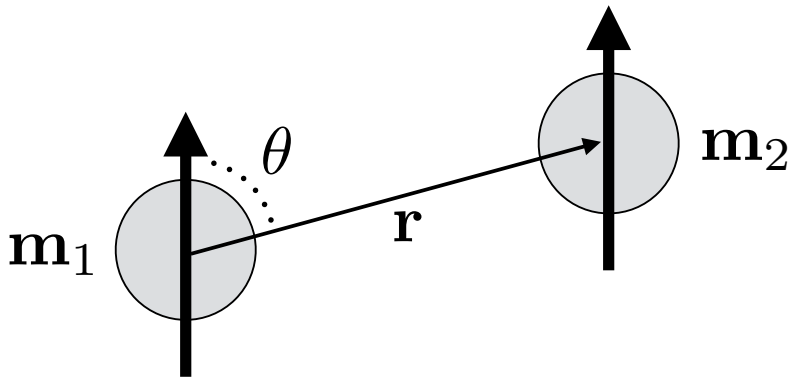

Figure 3.1 – Two magnetic dipoles characterized by their magnetic moment $\boldsymbol{m_1}$ and $\boldsymbol{m_2}$. Their relative position is given by $\boldsymbol{r}$ and θ.

3.2 Sphere-dipole equivalence

In the present work, spherical soft-ferromagnetic beads are immersed in an external magnetic field inducing magnetization of the beads. That magnetization has the effect of generating interactions, repulsive or attractive, between the beads. The aim of this section is to precisely understand the behavior a magnetizable spherical material under an external magnetic field.

Without electrical field or time-dependent magnetic field, the Maxwell's equations can be reduced to the fundamental equations of magnetostatics

$$\boldsymbol{\nabla} \cdot \boldsymbol{B} = 0, \tag{3.11}$$

$$\boldsymbol{\nabla} \times \boldsymbol{B} = \mu_0 \boldsymbol{J}, \tag{3.12}$$

for which the law of Biot and Savart law is the solution. Thus, if we precisely know the current density $\boldsymbol{J}$, we can calculate the magnetic field $\boldsymbol{B}$ at each point of the space. However, in a material, currents at atomic scale are too numerous and fluctuate too quickly, making impossible to take them all into account. To simplify the problem, the current density is splitted in two terms, a current from microscopic sources and a current from macroscopic sources.

$$\boldsymbol{J} = \boldsymbol{J}_{\text{micro}} + \boldsymbol{J}_{\text{macro}}. \tag{3.13}$$

For the microscopic contribution, we do not consider each localized current distribution but rather the macroscopic resultant of their effect: the bound current density $\boldsymbol{J}_{\text{micro}}$. It can be shown that the bound current is related to a macroscopic field $\boldsymbol{M}$, called the magnetization, by the relation

$$\boldsymbol{J}_{\text{micro}} = \boldsymbol{\nabla} \times \boldsymbol{M}. \tag{3.14}$$

Actually, the magnetization of a material corresponds to the volume density of magnetic dipole

$$\boldsymbol{M} = \frac{d\boldsymbol{m}}{dV} \tag{3.15}$$

The macroscopic current density $\boldsymbol{J}_{\text{macro}}$, due to the flow of free charges in the material, is related to a new macroscopic field $\boldsymbol{H}$, also called magnetic field, by the relation

$$\boldsymbol{J}_{\text{macro}} = \boldsymbol{\nabla} \times \boldsymbol{H}. \tag{3.16}$$

. Consequently, Eq. (3.12) becomes

$$\boldsymbol{\nabla} \times \boldsymbol{B} = \mu_0 \left[\boldsymbol{\nabla} \times \boldsymbol{H} + \boldsymbol{\nabla} \times \boldsymbol{M}\right] \tag{3.17}$$

giving

$$\boldsymbol{B} = \mu_0 \left[\boldsymbol{H} + \boldsymbol{M}\right]. \tag{3.18}$$

The most general constitutive equation linking the $\boldsymbol{B}$ and $\boldsymbol{H}$ is

$$\boldsymbol{B} = \mu \boldsymbol{H} \tag{3.19}$$

where μ is the permeability of the material and $\mu_r = \mu/\mu_0$ is the relative permeability of the material.The permeability is a scalar if the material is isotropic, a tensor otherwise. If μ does not depends on $\boldsymbol{H}$, one has a strictly linear relation between $\boldsymbol{B}$ and $\boldsymbol{H}$ and the material is said to be linear. In this case, with Eqs.(3.18) and (3.19) we can also write a linear relation between $\boldsymbol{M}$ and $\boldsymbol{H}$,

$$\boldsymbol{M} = \chi_m \boldsymbol{H}, \tag{3.20}$$

where

$$\chi_m = \mu_r - 1 \tag{3.21}$$

is the magnetic susceptibility. Note that, diamagnetic, paramagnetic and soft-ferromagnetic materials are linear. If magnetic field within a material is strong, the previous linear relations fail leading to nonlinear magnetism like in hard-ferromagnetic materials.

In our experiment, the beads are made of a linear material as shown is Sec. 2.2. Except Helmholtz coils that produce a homogeneous, and therefore, irrotational magnetic field, there is no macroscopic current thus

$$\boldsymbol{\nabla} \times \boldsymbol{H} = 0. \tag{3.22}$$

Hence we can introduce a magnetic scalar potential ϕ_m such as

$$\boldsymbol{H} = -\boldsymbol{\nabla} \phi_m \tag{3.23}$$

Using Eqs. (3.11), (3.18), (3.23), we can show that the magnetic scalar potential satisfies the Poisson equation

$$\nabla^2 \phi_m = \boldsymbol{\nabla} \cdot \boldsymbol{M}. \tag{3.24}$$

From now, we consider our bead as a sphere of radius σ with a vertical uniform magnetization $\boldsymbol{M} = M_0 \boldsymbol{e_z}$ and immersed in an external uniform vertical magnetic field $\boldsymbol{H_0} = H_0 \boldsymbol{e_z}$. The sphere is surrounded by a non-magnetic medium, meaning that $\boldsymbol{M} = 0$ outside of the sphere. Thus, $\boldsymbol{\nabla} \cdot \boldsymbol{M} = 0$ inside and outside of the sphere and the Poisson equation becomes the Laplace equation

$$\nabla^2 \phi_m = 0 \tag{3.25}$$

giving the magnetic scalar potential throughout of space. In spherical coordinates

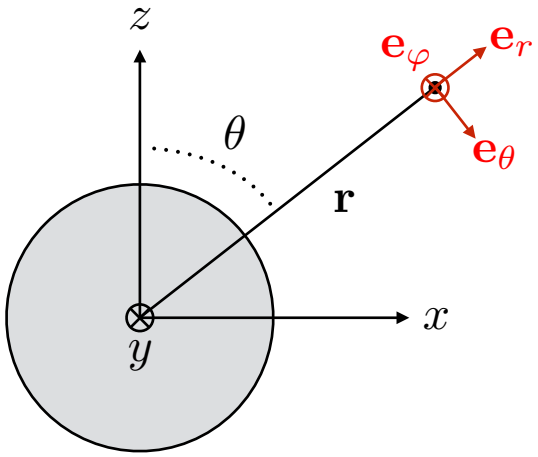

Figure 3.2 – Spherical coordinates (r,θ,φ) and related unit vectors $(\boldsymbol{e_r}, \boldsymbol{e_\theta}, \boldsymbol{e_\varphi})$.

(r, θ, φ) (see Fig. 3.2), the Laplace equation is written

$$\nabla^2 \phi_m = \frac{1}{r} \frac{\partial}{\partial r} \left(r^2 \frac{\partial \phi_m}{\partial r} \right) + \frac{1}{r^2 \sin\theta} \frac{\partial}{\partial \theta} \left(\sin\theta \frac{\partial \phi_m}{\partial \theta} \right) + \frac{1}{r^2 \sin^2\theta} \frac{\partial^2 \phi_m}{\partial \varphi^2} = 0. \tag{3.26}$$

To solve this equation, we use the separation of variable method, assuming that the magnetic potential is the product of three independent functions

$$\phi_m(r, \theta, \varphi) = R(r)\Theta(\theta)\Phi(\varphi). \tag{3.27}$$

Dividing (3.26) by (3.27) and multplying it by $r^2 \sin^2\theta$ gives

$$\frac{\sin^2\theta}{R} \frac{d}{dr} \left(r^2 \frac{dR}{dr} \right) + \frac{\sin\theta}{\Theta} \frac{d}{d\theta} \left(\sin\theta \frac{d\Theta}{d\theta} \right) + \frac{1}{\Phi} \frac{d^2\Phi}{d\varphi^2} = 0. \tag{3.28}$$

The φ dependence is isolated in the third term, so we can set it equal to an arbitrary constant value

$$\frac{1}{\Phi}\frac{d^2\Phi}{d\varphi^2} = -m^2. \tag{3.29}$$

The solutions of Eq. (3.29) are

$$\Phi(\varphi) = \begin{cases} \sin(m\varphi) \\ \cos(m\varphi) \end{cases} \tag{3.30}$$

Dividing (3.28) by $\sin^2\theta$ gives

$$\frac{1}{R}\frac{d}{dr}\left(r^2\frac{dR}{dr}\right) + \frac{1}{\Theta\sin\theta}\frac{d}{d\theta}\left(\sin\theta\frac{d\Theta}{d\theta}\right) - \frac{m^2}{\sin^2\theta} = 0 \tag{3.31}$$

The r dependence is isolated in the first term, so we set it equal to an arbitrary constant

$$\frac{1}{R}\frac{d}{dr}\left(r^2\frac{dR}{dr}\right) = l(l+1). \tag{3.32}$$

Therefore, the solutions Eq. 3.32 are

$$R(r) = \begin{cases} r^l \\ r^{-l-1} \end{cases} \tag{3.33}$$

Multiplying (3.31) by Θ gives

$$\frac{1}{\sin\theta}\frac{d}{d\theta}\left(\sin\theta\frac{d\Theta}{d\theta}\right) + \left(l(l+1) - \frac{m^2}{\sin^2\theta}\right)\Theta = 0. \tag{3.34}$$

The substitution $x = \cos\theta$ brings out the generalized Legendre equation

$$(1-x^2)\frac{d^2\Theta}{dx^2} - 2x\frac{d\Theta}{dx} + \left(l(l+1) - \frac{m^2}{1-x^2}\right)\Theta = 0 \tag{3.35}$$

whose solutions are the associated Legendre functions $\Theta(x) = P_l^m(x)$ and thus

$$\Theta(\theta) = P_l^m(\cos\theta) \tag{3.36}$$

Gathering solutions (3.30), (3.33), (3.36), particular solutions for the magnetic potential are

$$\phi_m = R(r)\Theta(\theta)\Phi(\varphi) = \begin{cases} r^l P_l^m(\cos\theta)\cos(m\varphi) \\ r^{-l-1} P_l^m(\cos\theta)\cos(m\varphi) \end{cases} \tag{3.37}$$

The problem treated here presents an azimuthal symmetry setting $m = 0$. Particular solutions for the magnetic potential become

$$\phi_m = \begin{cases} r^l P_l(\cos\theta) \\ r^{-l-1} P_l(\cos\theta) \end{cases} \tag{3.38}$$

and the general solution is

$$\phi_m = \sum_{l=0}^{\infty} A_l r^l P_l(\cos\theta) + \sum_{l=0}^{\infty} \frac{B_l}{r^{l+1}} P_l(\cos\theta) \tag{3.39}$$

- **Inside the sphere** $r < \sigma$.

The only constant term in Eq. (3.39) is arbitrarily set to zero, $A_0 = 0$, because a constant in Eq. (3.23) does not influence the expression of the magnetic field $\boldsymbol{H}$. The magnetic field must be finite inside the sphere, therefore $B_l = 0$ for all l, otherwise the potential would diverge at the center of the sphere. Finally, as a uniform magnetization of the sphere is assumed, the magnetic field $\boldsymbol{H}$ does not depend on r or θ. The Eq. (3.39) only respects this condition for $l = 1$. The magnetic scalar potential inside the sphere becomes

$$\phi_{in}(r,\theta) = A_1 r \cos\theta. \tag{3.40}$$

- **Outside the sphere** $r > \sigma$.

For identical reasons as the previous case $A_0 = 0$. Far from the sphere, the magnetic field must be finite and equal to the external magnetic field $\boldsymbol{H_0}$ setting $A_1 = -H_0$ and $A_l = 0$ for $l > 1$. To determine the value of each B_l, we use the boundary conditions for the magnetic field at an interface between two materials. These boundary conditions can be derived by applying Eqs. (3.22) and ((3.11)) at the frontier between the two media giving respectively

$$\boldsymbol{H_1} \times \boldsymbol{n_{12}} = \boldsymbol{H_2} \times \boldsymbol{n_{21}} \tag{3.41}$$

$$\boldsymbol{B_1} \cdot \boldsymbol{n_{12}} = \boldsymbol{B_2} \cdot \boldsymbol{n_{21}} \tag{3.42}$$

where $\boldsymbol{n_{12}}$ is the normal vector from a medium 1 to a medium 2.

The condition parallel to the boundary (3.41) can be expressed as

$$\left.\frac{\partial \phi_{in}}{\partial \theta}\right|_{r=\sigma} = \left.\frac{\partial \phi_{out}}{\partial \theta}\right|_{r=\sigma} \tag{3.43}$$

giving

$$A_1 \sin\theta = -H_0 \sin\theta + \frac{B_1}{\sigma^3} \sin\theta + \sum_{l=2}^{\infty} \frac{B_l}{\sigma^{l+2}} \frac{dP_l(\cos\theta)}{d\theta}. \tag{3.44}$$

Consequently $B_l = 0$ for $l > 1$ to satisfy the equation for each value of θ.

The condition 3.42 perpendicular to the interface between the magnetized sphere and the non-magnetic medium can be expressed

$$\mu_r \mu_0 \frac{\partial \phi_{in}}{\partial r}\bigg|_{r=\sigma} = \mu_0 \frac{\partial \phi_{out}}{\partial r}\bigg|_{r=\sigma} \tag{3.45}$$

giving

$$\mu_r \mu_0 A_1 \cos\theta = -\mu_0 H_0 \cos\theta - \mu_0 \frac{B_0}{\sigma^2} - \mu_0 \frac{2B_1 \cos\theta}{\sigma^3}. \tag{3.46}$$

B_0 must be set to zero because this equation must be valid for each value of θ.

Using (3.44) and (3.46) we find

$$A_1 = -\frac{3H_0}{2+\mu_r} \tag{3.47}$$

and

$$B_1 = -\frac{H_0 \sigma^3 (1-\mu_r)}{2+\mu_r}, \tag{3.48}$$

meaning that the magnetic scalar potential is explicitly known everywhere.

An interesting result can be extracted from the magnetic field inside the sphere. Indeed, the magnetic scalar potential inside the sphere is

$$\phi_{in} = -\frac{3H_0}{\mu_r + 2} r \cos\theta, \tag{3.49}$$

giving the magnetic field inside the sphere

$$\boldsymbol{H_{in}} = \frac{3}{\mu_r + 1} \boldsymbol{H_0}. \tag{3.50}$$

and the magnetization inside the sphere

$$\boldsymbol{M} = \frac{3(\mu_r - 1)}{2+\mu_r} \boldsymbol{H_0}. \tag{3.51}$$

The effective susceptibility of the material is therein introduced

$$\chi = \frac{3(\mu_r - 1)}{2+\mu_r}. \tag{3.52}$$

This quantity links the magnetization of the medium $\boldsymbol{M}$ and the external magnetic field $\boldsymbol{H_0}$, contrary to equation (3.20) which links the magnetization to the total magnetic field $\boldsymbol{H}$ in the sphere. Moreover for material with a high magnetic

permeability, like our soft-ferromagnetic beads, the effective susceptibility of a sphere is

$$\lim_{\mu_r \to +\infty} \chi = 3. \tag{3.53}$$

This theoretical result is experimentally observed in Fig. 2.2.

Using the effective susceptibility, the magnetic scalar potential outside of the sphere is

$$\phi_{out} = -H_0 r \cos\theta - \frac{H_0 \sigma^3 \chi \cos\theta}{3r^2}, \tag{3.54}$$

giving

$$\boldsymbol{H_{out}} = \boldsymbol{H_0} + \frac{H_0 \sigma^3 \chi}{3r^3} \left[2\cos\theta \boldsymbol{e_r} + \sin\theta \boldsymbol{e_\theta} \right]. \tag{3.55}$$

The magnetic field outside of the sphere is composed of two contributions, the external magnetic field $\boldsymbol{H_0}$ and the magnetic field due to the sphere

$$\boldsymbol{H_S} = \frac{H_0 \sigma^3 \chi}{3r^3} \left[2\cos\theta \boldsymbol{e_r} + \sin\theta \boldsymbol{e_\theta} \right]. \tag{3.56}$$

The uniform magnetization, Eqs. (3.15) and (3.51) give

$$\boldsymbol{m} = V\boldsymbol{M} = 4/3\pi\sigma^3 \chi \boldsymbol{H_0}, \tag{3.57}$$

with $\boldsymbol{e_z} = \cos\theta \boldsymbol{e_r} - \sin\theta \boldsymbol{e_\theta}$ Eq. (3.56) becomes

$$\boldsymbol{H_S} = \frac{m}{4\pi r^3} \left[3\cos\theta \boldsymbol{e_r} - \boldsymbol{e_z} \right]. \tag{3.58}$$

With $m\cos\theta = \boldsymbol{m} \cdot \boldsymbol{e_r}$ and $\boldsymbol{e_r} = \frac{\boldsymbol{r}}{r}$ and $\boldsymbol{m} = m\boldsymbol{e_z}$, the magnetic field produced by a uniformly magnetized sphere is written

$$\boldsymbol{H_S} = \frac{1}{4\pi} \left[-\frac{\boldsymbol{m}}{r^3} + \frac{3(\boldsymbol{m} \cdot \boldsymbol{r}) \cdot \boldsymbol{r}}{r^5} \right] \tag{3.59}$$

and the associated magnetic $\boldsymbol{B}$-field

$$\boldsymbol{B_S} = \frac{\mu_0}{4\pi} \left[-\frac{\boldsymbol{m}}{r^3} + \frac{3(\boldsymbol{m} \cdot \boldsymbol{r}) \cdot \boldsymbol{r}}{r^5} \right] \tag{3.60}$$

which correspond exactly to the relation (3.6) describing the magnetic field generated by a magnetic dipole.

3.3 Bead-bead interaction

The beads of our experiments are assimilated to magnetized spheres. As the magnetic field of a magnetic sphere is perfectly equivalent to a dipole one, the interaction between two beads is mathematically identical to Eq. (3.8)

$$U(r,\theta) = \frac{\mu_0}{4\pi}\frac{m_1 m_2}{r^3}\left[1 - 3\cos^2\theta\right]. \tag{3.61}$$

This interaction is illustrated in Fig. 3.3 using a color mapping of the interaction throughout the space between a bead and a reference bead. Note that here, the external magnetic field $\boldsymbol{H_0}$ is not taken into account because it is homogeneous and given Eq. (3.7), it is effectless on the bead. Actually, $\boldsymbol{H_0}$ is only applied to magnetize beads. Experimentally, two distinct cases were considered. A monodisperse case where the cell is filled with identical beads and a bidisperse case where two types of beads are used. In the monodisperse each bead carries the same magnetic dipole moment $\boldsymbol{m} = \chi V \boldsymbol{H_0}$. Moreover, the center of mass of each bead is contained in the same plane and thus the vector $\boldsymbol{r}$ linking two spheres and their magnetic moment $\boldsymbol{m}$ are perpendicular meaning that $\cos\theta = 1$. The interaction between two beads is

$$U(r) = \frac{\mu_0}{4\pi}\frac{\chi^2 V^2 H_0^2}{r^3}, \tag{3.62}$$

corresponding to a repulsive and purely radial interaction. To estimate the typical pair interaction within the system, we define a mean pair interaction

$$\langle U \rangle = \frac{\mu_0}{4\pi}\chi^2 V^2 H_0^2 \left(\frac{\sqrt{3}}{2}\rho\right)^{3/2} \tag{3.63}$$

where $\left(\frac{\sqrt{3}}{2}\rho\right)^{-1/2}$ is the lattice spacing of a perfect hexagonal lattice which has a particle area density ρ.

In the bidisperse case, the experimental cell is filled with two types of beads, made of the same material but with different volumes V_1 and V_2. Therefore, the magnetic dipole moments are parallel but don't have the same magnitude $m_1 \neq m_2$. Moreover, the difference in volume has the consequence that the centers of mass of two different beads are not contained in the same plane. Consequently the vector linking two spheres of different size and their magnetic moment are not perpendicular, so $\cos(\theta) \neq 1$. Using $\boldsymbol{m_i} = \chi V_i \boldsymbol{H_0}$, with $i = 1, 2$, the interaction between two different beads is

$$U(r) = \frac{\mu_0}{4\pi}\frac{\chi^2 H_0^2 V_1 V_2}{r^3}\left[1 - 3\cos^2\theta\right]. \tag{3.64}$$

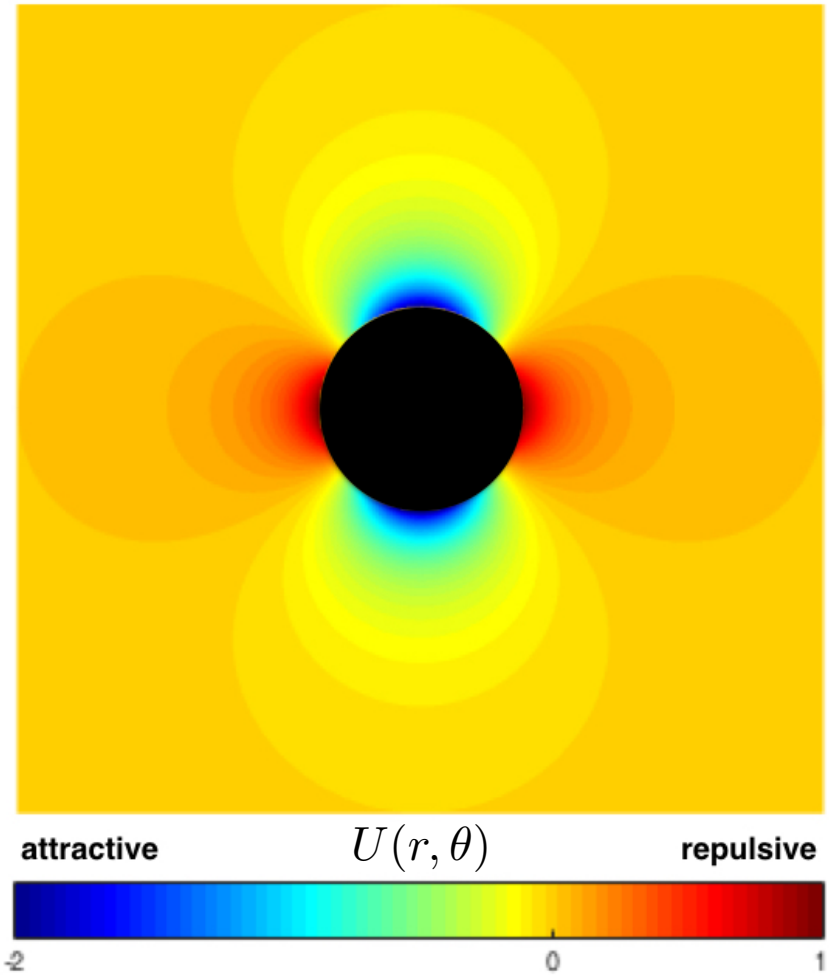

Figure 3.3 – Mapping of the dimensionless potential interaction energy $U(r,\theta)$ (in arb. unit) between a reference bead (in black) and another bead the same magnetic moment that the refrence beads, $m_1 = m_2$. The radius of the beads is set to 1.

As illustrated in Fig. 3.4, the angle θ, the distance r and the radius difference of the beads $\Delta\sigma$ are linked with a basic trigonometric relation $\cos\theta = \Delta\sigma/r$ giving

$$1 - 3\cos^2\theta = 1 - 3\left(\frac{\Delta\sigma}{r}\right)^2. \tag{3.65}$$

In experimental conditions, $r \sim 10\Delta\sigma$, so Eq. (3.65) is close to1. Consequently, we neglect the angular dependence in Eq. (3.64), this approximation represents an error on the energy of the order of 3%. Actually, the significant influence of

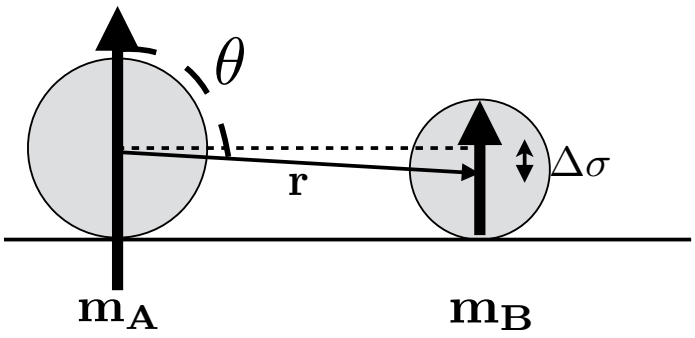

Figure 3.4 – Schematic representation of the bidisperse case.

the bidispersity on pair interactions results from the fact that both types of beads have a different magnetic dipole moment. We introduce the dipolar ratio

$$\upsilon = \frac{m_2}{m_1} = \frac{V_2}{V_1}, \tag{3.66}$$

which can be written as the ratio of the volumes using Eq. (3.57). The interactions between each possible pair become

$$U_{11}(r) = \frac{\mu_0}{4\pi}\frac{\chi^2 V_1^2 H_0^2}{r^3}, \tag{3.67}$$

$$U_{12}(r) = \upsilon U_{11}(r), \tag{3.68}$$

$$U_{22}(r) = \upsilon^2 U_{11}(r). \tag{3.69}$$

Each individual pair interaction can be now quantified, but the mean pair interaction in the system depends on the composition of the mixture. The composition of a bidisperse mixture containing N_1 beads of size V_1 and N_2 beads of size V_2 is characterized by its stochiometry

$$\xi = \frac{N2}{N1 + N2}. \tag{3.70}$$

In a bidisperse system, the most likely pair interaction between two beads separated by a distance r is

$$U(r) = p_{11}U_{11}(r) + p_{12}U_{12}(r) + p_{22}U_{22}(r) \tag{3.71}$$

which corresponds to the average of Eqs. (3.67), (3.68) and (3.69) weighted by the probability p_{ij} to find a pair i, j among all the pairs. Using Eq. (3.70) and

assuming a large number of beads we find

$$p_{11} = \frac{C_{N_1}^2}{C_{N_{tot}}^2} = (1-\xi)^2, \tag{3.72}$$

$$p_{12} = \frac{C_{N_1}^1 C_{N_2}^1}{C_{N_{tot}}^2} = \xi(1-\xi), \tag{3.73}$$

$$p_{22} = \frac{C_{N_2}^2}{C_{N_{tot}}^2} = \xi^2. \tag{3.74}$$

Combining Eqs. (3.67) to (3.74) gives the most likely pair interaction between two beads at distance r

$$U(r) = \frac{\mu_0}{4\pi}\frac{\chi^2 V_1^2 H_0^2}{r^3}\left[\upsilon\xi + (1-\xi)\right]^2. \tag{3.75}$$

As previously for the monodisperse case, we use $\left(\frac{\sqrt{3}}{2}\rho\right)^{-1/2}$ to estimate the average distance between two paired beads, we define the mean pair interaction for a bidisperse system as

$$\langle U\rangle = \frac{\mu_0}{4\pi}\chi^2 V_1^2 H_0^2\left[\upsilon\xi + (1-\xi)\right]^2\left(\frac{\sqrt{3}}{2}\rho\right)^{3/2}. \tag{3.76}$$

Throughout this section the magnetic moment of the beads is assumed to be only induced by the external magnetic field $\boldsymbol{H_0}$, as shown in Eq. (3.51). But when there is more than one bead, the magnetization of a bead is due to the external magnetic field and the magnetic field from other beads. If we consider only two beads, the local magnetic field at the position of a bead is the superposition of the external magnetic field $\boldsymbol{H_0}$ and the magnetic field produced by the other beads H_S given by Eq. (3.56). To simplify, $\chi = 3$ and $\theta = \pi/2$, thus we can write the local field

$$\boldsymbol{H_{loc}} = \boldsymbol{H_0} + \boldsymbol{H_i} = \boldsymbol{H_0}\left[1 - \frac{\sigma^3}{r^3}\right]. \tag{3.77}$$

Practically, this relation is incomplete because if a magnetic dipole influences another one, the reciprocal is true and one must take into account a non-trivial coupling. However, let us use Eq. (3.77) to estimate the order of magnitude of this demagnetizing field. At contact $r = 2\sigma$, the local field at the center of a bead is $H_{loc} = \frac{7}{8}H_0$ but quickly tends to H_0 when the distance between beads increases. Indeed, at the typical distance between two beads in our experiments, which is $r \sim 4\sigma$, the local magnetic field is about 98% of the external magnetic field. When the beads are not in contact, the demagnetizing effect is weak enough to neglect it in the estimation of the interaction between beads.

3.4 Bead-wall interaction

The beads are contained within a horizontal cell. To avoid parasitic effects, such as inhomogeneities due to inelastic collisions, the cell is made of a ferromagnetic material. As a consequence, the walls of the cell are repulsive to the beads. An analytic characterization of the bead-wall interaction is an arduous mathematical problem due to, among others, the symmetry of the problem which corresponds here to a polygonal hole in a ferromagnetic sheet. In addition, the alloy in which the cell is machined is not well characterized. The material appears to be ferromagnetic, but it is difficult to know its magnetic properties such as the saturation, the remanence or the coercivity. We don't even know if the magnetic response is isotropic. To estimate the interaction between a bead and the cell, we thus use a toy model considering the wall of the cell as a row of independent imaginary beads at contact, each bearing the same magnetic dipole moment $\boldsymbol{m}$ as the real beads of the bulk. The interaction between a bead and the wall is the sum of the interactions between a bead and all the imaginary beads forming the wall.

$$U_{b,w} = \sum_{i \in \text{wall}} \frac{\mu_0}{4\pi} \frac{m^2}{r_i^3}. \tag{3.78}$$

The model is represented in Fig. 3.5 for a square cell, the red dots correspond to the imaginary beads that form the wall of the cell and the white dots represent the position of real beads in the cell, in the monodisperse case. The color mapping inside the cell corresponds to the energetic landscape of the interaction between the wall and a reference bead. The interaction is normalized by the mean pair interaction$< U >$ and the color cut off is fixed to $15 < U >$. The energy carried by a bead i due to other beads $j \neq i$ can be written as the sum of the pair interaction with them

$$U_{i,b} = \sum_{j \neq i} \frac{\mu_0}{4\pi} \frac{m^2}{r_{ij}^3}. \tag{3.79}$$

The total magnetic energy carried by a bead i is due to the other beads and the cell, respectively given by Eqs. (3.78) and (3.79). Our observations point out a homogeneous density distribution meaning that each particle of the system carries the same amount of magnetic energy, meaning that

$$U_i = U_{i,b} + U_{i,w} \tag{3.80}$$

must be constant for each bead. Considering a perfect hexagonal lattice, we numerically find that for a bead far from the boundaries $U_{i,b} = 11.00 < U >$ and $U_{i,w} = 0$. For a bead situated at the first outer layer of a finite hexagonal lattice we find numerically $U_{i,b} = 6.75 < U >$, this layer is thus supposed to be at a distance from the wall such that $U_{i,w} = 4.25 < U >$. Similarly for the second outer

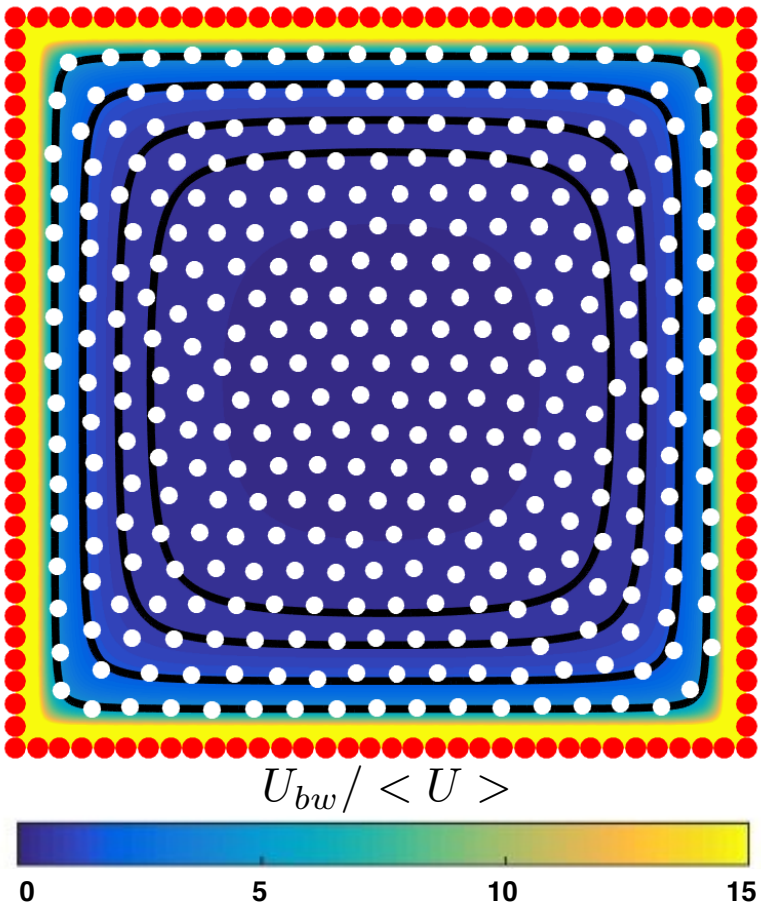

Figure 3.5 – Color mapping of the interaction $U_{b,w}$ between the cell and a reference bead according to the model. The boundaries of the cell are substituted by imaginary balls indicated by red dots. The experimental position of the beads is indicated by white dots. Black curves correspond to the predicted position of the four-first layers of beads of the system.

layer, we find $U_{i,b} = 9.35 < U >$ which give $U_{i,w} = 1.65 < U >$, and so on for the next layers. In Fig. 3.5, black curves indicates the positions of the predicted equipotentials $U_{b,w} = 4.75 < U >$, $U_{b,w} = 1.65 < U >$, and so on. The match between the predicted position of the equipotentials and the real position of the beads is made without any adjustment which allows us to validate the model.

4 Agitation

The Brownian motion takes its name from the naturalist Robert Brown, who noticed the random motion of pollen grains in water. This observation was explained theoretically many years later by Albert Einstein and confirmed experimentally by Jean Perrin. The pollen grain or more generally a Brownian particle, is immersed in a fluid composed of much smaller particles and undergoes a lot of collisions by these particles. The high frequency of collisions caused by a large number of molecules explains the random nature of the motion. The degree of agitation of the particle is quantified by the temperature T using the relation

$$\frac{1}{2}m < v^2 >= \frac{D}{2}k_B T \tag{4.1}$$

where $< v^2 >$ is the mean square velocity of the particle over time, d is the dimensionality of space and k_B is the Boltzmann constant. A particle of size σ presents a Brownian motion if it is sensitive to the thermal agitation, meaning that at the scale of the particle, the thermal agitation must be more important than the work of the gravitational forces

$$(\rho g \sigma^3)\sigma < k_B T, \tag{4.2}$$

and thus

$$\sigma < \left(\frac{k_B T}{\rho g}\right)^{1/4}. \tag{4.3}$$

Our experimental setup is composed of millimetric beads which do not respect this condition. The system is thus athermal, meaning that thermal agitation is not sufficient to move the beads. Therefore, an external source of agitation is needed, whose technical aspects are detailed in Chapter 2. Our mechanical agitation aims to mimic a Brownian motion with athermal beads. This would allow us to use the equivalence between the mean kinetic energy of the beads and

the temperature as evoked in the Eq. (4.1). Consequently, some conditions must be verified concerning the diffusivity and the velocity distribution. Experimental results presented in this Chapter are all performed with a set of 250 interacting beads of one millimeter diameter, with a particle area density $\rho = 230000$ beads per m^2. The agitation is studied here for three different interaction strengths between beads, characterized by the external magnetic field H_0. Under an external magnetic fields of 5000, 7000 and 10000 A/m, the interactions are respectively considered as weak, intermediate and strong. The motion of the beads is recorded with a high-speed camera at a rate of 500 frames per second in order to study the short time scale behavior of the system.

4.1 Mean square displacement

A microscopic description of the diffusion of a Brownian particle in a fluid is provided by the Langevin equation

$$m\frac{d\mathbf{v}}{dt} = -\gamma\mathbf{v} + \mathbf{f}, \tag{4.4}$$

where m and $\mathbf{v}$ are the mass and the velocity of the particle, γ a viscous friction coefficient and $\mathbf{f}$ is a force corresponding to random kicks due to the environment, thus its average over a lot of kicks is $\langle\mathbf{f}\rangle = 0$. To characterize how a Brownian particle explores space during a time interval τ, we define the mean square displacement (MSD)

$$\Delta r^2(\tau) = \langle[\mathbf{r}(t+\tau) - \mathbf{r}(t)]^2\rangle_t, \tag{4.5}$$

where $\langle.\rangle$is the average over all possible intervals τ of the trajectory. If the studied system includes several particles, the MSD is also averaged over all the particles. From Eq. (4.4) and using Eq. (4.1) for 2D space, one can write the MSD of a free particle

$$\Delta r^2(\tau) = \frac{2k_BT}{\gamma}\left[\tau + \frac{m}{\gamma}\exp(\frac{-\gamma\tau}{m}) - \frac{m}{\gamma}\right], \tag{4.6}$$

giving

$$\lim_{\tau\to 0}\Delta r^2(\tau) = \frac{2k_BT}{m}\tau^2, \tag{4.7}$$

$$\lim_{\tau\to\infty}\Delta r^2(\tau) = \frac{4k_BT}{\gamma}\tau. \tag{4.8}$$

The MSD displays a ballistic motion at short time scale, corresponding to a uniform rectilinear motion between two successive collisions with its environment.

The MSD presents a diffusive motion at long time scale which is a consequence of the many random collisions. The diffusion coefficient of such a motion is

$$D = \frac{k_B T}{\gamma}. \tag{4.9}$$

Considering a Brownian particle constrained to move in a harmonic potential [88, 89] one has

$$\lim_{\tau \to 0} \Delta r^2(\tau) = \frac{2 k_B T}{m} \tau^2 \tag{4.10}$$

exactly like a free Brownian particle. This means that the particle does not suffer from the effect of the confining potential at short time scale, but only of the effect of the thermal bath. At long time scale

$$\lim_{\tau \to \infty} \Delta r^2(\tau) = \frac{4 k_B T}{K}, \tag{4.11}$$

where K is a constant depending on the harmonic potential strength. This result means that the Brownian particle is locally trapped and can not explore freely the space. The particle is said to be caged.

Fig. 4.1 shows our experimental MSD. Depending on the strength of the pair interaction between the beads, we observe whether a diffusive behavior or a caged behavior at long time scale which is in agreement with Eqs. (4.8) and (4.11).Actually, each bead is immersed in a magnetic energetic landscape generated by other beads. At weak pair interaction, this landscape is quite flat and beads can move freely within it, leading to the diffusive motion. Oppositely, at strong pair interaction, this landscape is hilly and particles are trapped. From weak to strong interaction, the landscape becomes less flat, making the diffusion less effective. The MSD of such an intermediate situation is therefore a combination of Eqs. (4.8) and (4.11). We also observe that, at short time scale, the ballistic motion of the particles does not depend on the interaction strength, in agreement with Eqs. (4.7) and (4.10). The transition from ballistic to diffusive motion occurs near a characteristic time $\tau_c = 0.1$s. The MSD of the mechanically agitated beads reproduces closely the behavior of thermal particles, both at short and long time scale. Moreover, using Eq. (4.1) for $D = 2$, MSD at short time scale is directly related to the mean square velocity $< v^2 >$ of the system and consequently, a kind of temperature.

The behavior of the system is successfully described by Eq. (4.4) but the nature of the random force $\boldsymbol{f}$ in our experiment is still elusive. Is this force directly applied by the mechanical vibration or is it due to collisions with other beads? To answer this question, the MSD of a very diluted system composed of only 10 beads is compared to the previous MSD obtained with 250 beads (see insert of Fig. 4.1). Both measurements are performed under identical condition of

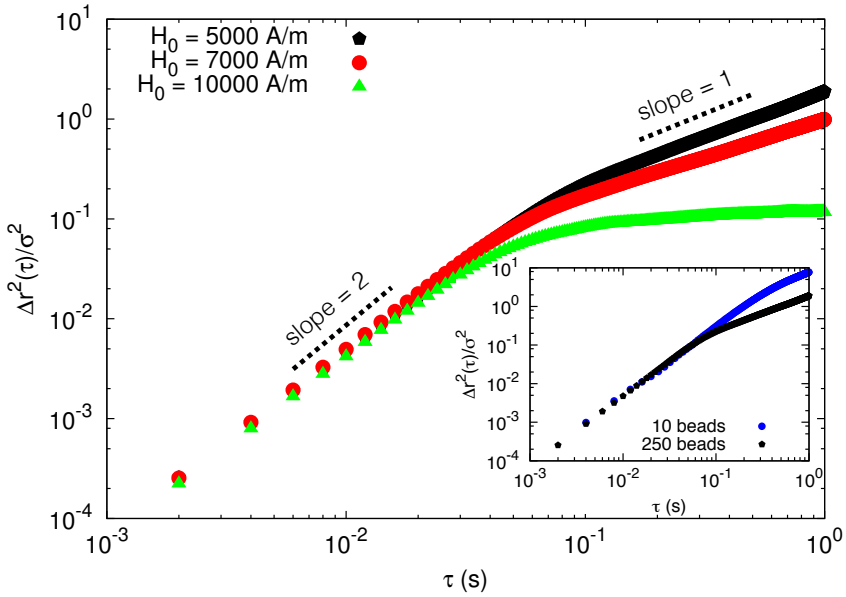

Figure 4.1 – Mean square displacement of interacting beads submitted to a mechanical agitation. Black, red and green curves represent the MSD of the beads under external magnetic fields H_0 respectively equal to 5000 A/m, 7000 A/m and 10000 A/m. In the insert: MSD of two systems composed of 10 and 250 beads under an external magnetic field $H_0 = 5000$ A/m and subjected to an identical mechanical agitation.

agitation, confinement and magnetic field ($H_0 = 5000$ A/m). In the very diluted case, where collisions between beads are rare, we observe a later establishment of the diffusive regime compared to the case with 250 beads, where collisions are frequent. This indicates that the diffusive motion is driven by successive collisions between beads rather than by the mechanical vibration itself.

4.2 Velocity distribution

In a 2D thermal system, the velocity of a particle follows a Maxwell-Boltzmann distribution

$$f(v) = \frac{v}{\alpha^2} \exp\left(-\frac{v^2}{2\alpha^2}\right), \tag{4.12}$$

where

$$\alpha^2 = \frac{k_B T}{m} \tag{4.13}$$

which can be written using Eq. (4.1)

$$\alpha^2 = \frac{< v^2 >}{2}. \tag{4.14}$$

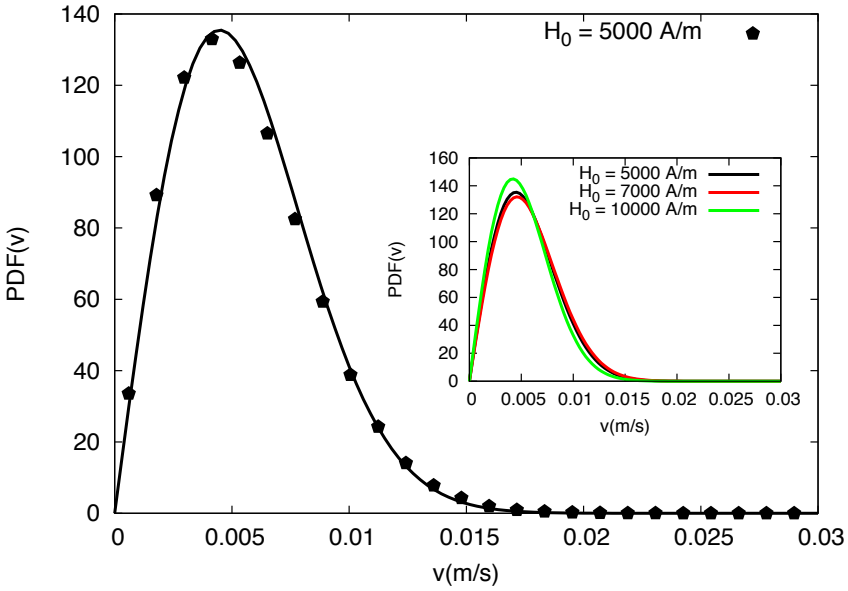

Figure 4.2 – Probability distribution function of particles velocity for an applied magnetic field $H_0 = 5000$ A/m. Dots correspond to the experimental distribution, and the solid line corresponds to the Maxwell-Boltzmann distribution given by Eq. (4.12). Insert: black, red and green curves are velocity distributions of the beads under external magnetic fields H_0 respectively equal to 5000 A/m, 7000 A/m and 10000 A/m.

As a remark, a Maxwellian distribution of the velocity v is the consequence of a Gaussian distribution of the velocity projected along each direction of the plane v_x and v_y. Usually, in granular systems, the velocity distribution deviates from a Maxwellian distribution due to dissipative collisions. However, thanks to the dipole-dipole interaction between beads, collisions are elastic. In Fig. 4.2 is presented the experimental velocity distribution of the beads for a weak interacting system ($H_0 = 5000$A/m). The solid line corresponds to Eq. (4.12) where the parameter α is calculated from the experimental measurement of $< v^2 >$, which is extracted from the tracking of the beads. The excellent agreement between the theoretical curve and data confirms that our mechanical agitation mimics closely a thermal agitation. This successful analogy with an equilibrium thermal system also suggests that the energy injected mechanically into the cell and the dissipation

due to friction with the bottom of the cell are balanced, so that the kinetic energy remains constant in the system. Note that our pseudo-thermal bath does not depend on the interaction between the beads as shown in the insert of Fig. 4.2.

The velocity is measured here by comparing the position of the beads between two images separated by a time interval $\tau = 0.05$s. The choice of this interval is discussed in the following Section.

4.3 Discussion

The measure of the instantaneous velocity of a Brownian particle is a delicate problem because it depends on the interval of time τ used to compare the position of the particle [88, 90]. However, an accurate measurement of the mean square velocity is required to define a temperature in our system. The Langevin equation in Eq. (4.4), teaches us that the motion of a Brownian particle has two distinct regimes, ballistic at short time scale and diffusive at long time scale. The transition between the two regimes occurs near a characteristic time τ_c. If, experimentally, the acquisition time between two images is $\tau > \tau_c$, we can only observe the motion of the particles in the diffusive regime because a single particle undergoes too many collisions between two successive images. One can use Eq. (4.8) to make a rough estimation of the mean velocity in the diffusive regime

$$\frac{\sqrt{\Delta r^2(\tau)}}{\tau} = \sqrt{\frac{2D}{\tau}}. \tag{4.15}$$

This relation depends explicitly on the time interval meaning that it is impossible to estimate the velocity of a particles if $\tau > \tau_c$. Therefore the velocity of a particle must be measured at $\tau < \tau_c$ to be in the ballistic regime where the velocity is supposed to be constant between two collisions. As the transition occurs around $\tau_c = 0.1$s, working at 10 frames per seconds (fps) is a minimum to measure the velocity. Fig 4.3 shows the mean velocity in our system as a function of the interval τ. Note that the same ballistic-diffusive transition is observed. At long time scale, the slope in log scale is equal to $-1/2$ which is in agreement with the estimation made in Eq. (4.15). However, for short time scale the slope is not strictly zero as expected. A careful look at the MSD at short time scale reveals that the slope in log scale is slightly lower than 2, meaning that the motion is not strictly ballistic. Indeed, the average time between two successive collisions, given by τ_c, is higher than the period of the mechanical excitation which is 1/35s (see Sec. 2.5). Thus the uniform rectilinear trajectory between two collisions is disturbed by high frequency fluctuations from mechanical vibrations.

Despite this technical issue, it is possible to determine the optimal time interval τ to measure the velocity and consequently the best frame rate for data acquisition.

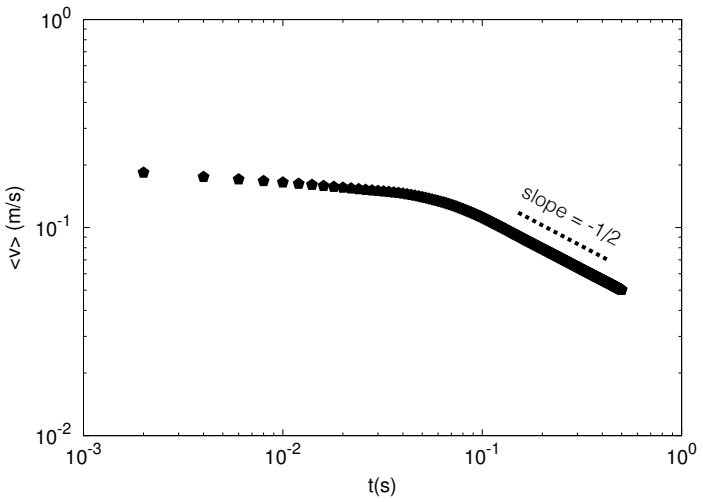

Figure 4.3 – Experimental measurement of the mean velocity as a function of the time interval τ used to compare the position of the particle.

As previously mentioned, the log scale slope of the MSD at short time scale is supposed to be equal to $< v^2 >$. Thus, the mean square velocity $< v^2 >$ of the beads is measured using different time interval and compared to the MSD at short time scale. The best agreement is obtained with a time interval $\tau = 0.05$s. In other words, it is when the system is observed at 20 fps that it looks the most like a real thermal system. As an example, studying the dynamics of the system at 10 fps induces a relative error on the temperature of about 36% compared to the temperature estimated at 20 fps.

As a concluding remark, the results presented in this section are obtained from a specific sequence of experiments dedicated to understanding the nature of the agitation produced by our mechanical vibration. We point out a thermal-like behavior of the beads and extract characteristic parameters of the agitation like the ballistic-diffusive transition time τ_c and the best frame rate to use. However, any mechanical change in the experimental device, even slight like a change in the tightening of a screw, alters the response of the beads to the vibration. After some empirical adjustments, it is always possible to find back a thermal-like behavior of the beads. But unfortunately, the characteristic parameters of the agitation strongly depend, without any apparent causal link, on the experimental conditions and the mechanical state of the device. Therefore, a general calibration of the agitation is impossible, and the agitation should be characterized case by case.

5 Melting

J. Schockmel, E. Mersch, N. Vandewalle and G. Lumay,
Melting of a confined monolayer of magnetized beads
Phys. Rev. E **87**, 062201 (2013).

5.1 Introduction

In three dimensions, crystals are characterized by both long range translational and orientational order. The melting in 3D occurs by simultaneous loss of both translational and orientational order in a single phase transition. The situation is different for two dimensional systems. Indeed, Mermin and Wagner [43] pointed out that, in 2D systems with short-range interactions, spontaneous breaking of continuous symmetries is forbidden at finite temperature. This can also be viewed as an instability of the system against thermal fluctuations. A direct consequence of this statement is the lack of strictly long range translational order, the term quasi-long range is then used for 2D crystals. On the contrary, Mermin [44] proved that long range orientational order is preserved. These properties lead to a different melting scenario in 2D than in 3D.

Many theoretical models have been developed to understand the melting process in two dimensions. The most popular one is the Kosterlitz-Thouless-Halperin-Nelson-Young (KTHNY) theory [45, 46, 56, 57, 58, 91], which predicts a melting from solid to liquid in two stages. During the first transition, translational order is completely lost but orientational order becomes a quasi-long range order. During the second transition, the orientational order is also completely lost. The intermediate phase is called hexatic for a hexagonal lattice. For details about the different phases and their order according to the KTHNY theory, see Section 5.2.

This theory has been a continuous matter of debates during the last 40 years. Many numerical and experimental studies have been carried out [34, 35, 36, 37, 59, 60, 61, 62, 63, 64, 66, 92, 93, 94, 95, 96, 97]. Most of them agree with the KTHNY

theory without excluding other theories. Previous experiments concerning 2D melting have been performed with thermal model systems such as colloids with hard-sphere interactions [93, 94] and with magnetic dipole-dipole interactions [59, 60]. The two-step transition from liquid to solid is observed as predicted by the KTHNY theory. These results have been confirmed by numerical simulations [95, 98]. In addition, experiments have been performed with athermal systems with hard-sphere interaction [35, 36, 34] (confirmed numerically [37]) and with Coulomb interactions [96, 97]. To our knowledge, no athermal system with short-range interaction has been experimentally explored. Let us also point out another experiment that has been performed with a system of ferrofluid spikes [66]. Each work mentioned noticed that 2D crystals melt according to the KTHNY theory, even in clearly finite sized systems [96, 66]. Between all these systems, the only difference is related to the nature of the interaction. Indeed, considering a power-law interaction r^{-n}, for $n < 6$ the liquid-hexatic transition is continuous as strictly predicted by the KTHNY theory while for $n \geq 6$ the liquid-hexatic transition is a first-order transition with phase coexistence [92]. In this chapter, we confront our experimental model system to the well-known KTHNY theory, whose main keys are recalled, with the use of both static and dynamic order parameters in order to identify the signature of the double phase transition and the intermediate hexatic phase.

5.2 KTHNY theory

In this section, we outline KTHNY's theory and previous results that led to it. The focus is on the intuitive understanding of the underlying concepts. For this purpose, we do not enter into the details of calculations, unless they improve the understanding of the phenomenon. For details see [45, 56, 57, 58, 99].

5.2.1 Mermin-Wagner theorem

Roughly, the Mermin-Wagner theorem can be stated as follows: a spontaneous break of continuous symmetry is impossible in a 1D and 2D system at finite temperature. At macroscopic scale a fluid is homogeneous in space and so invariant according to any translation or rotation. The fluid is said to have continuous symmetry of translation and rotation. But, during a usual crystalization at 3D the degrees of freedom are restricted, translational and rotational symmetries become discrete and respect specific groups of symmetry, it is a spontaneous break of symmetry occurs.

Let us first begin with an argument exposed by Peierls to catch the great

importance of the dimensionality in the order of a crystal. Considering a square spin lattice of size N^D, where D is the dimension of the space, it is possible to calculate the Hamiltonian of the lattice travelled by a spin wave. If a spin is a unitary vector $\mid \boldsymbol{S_i} \mid = 1$ that can take all possible directions in the plane (XY model), the Hamiltonian is

$$H = -J \sum_{<i,j>} \cos(\theta_i - \theta_j), \tag{5.1}$$

where $J > 0$ is the spin coupling constant, the sum over $< i, j >$ corresponds to the sum over pairs of nearest neighbors, θ_i is the orientation of the ith spin of the lattice. In the case of the longest wavelength in a finite spin lattice (see Fig. 5.1(top)), the difference of angle between two neighboring spins is $\theta_i - \theta_j = 2\pi/N$ and for large systems, this value is small enough to expand equation (5.1) in Taylor series at order 1 (harmonic approximation) and make the sum over each neighboring spins

$$H = E_0 + \frac{J}{2} N^D \left(\frac{2\pi}{N}\right)^2, \tag{5.2}$$

with E_0 the ground state energy where spins are aligned. The probability to observe a spin lattice travelled by a wave of spin of given by the Boltzmann distribution $P \sim \exp(-H/k_B T)$. For $D = 3$, the Hamiltonian diverges for large number of spin ($N \to \infty$), the wave configuration is thus impossible leading to long-range order at low temperature. But for $D = 1, 2$, the long wavelength mode is accessible at finite temperature. Indeed, at 1D the Hamiltionan converges towards the energy of the ground state E_0, making the wave configuration as favorable as the ground state and thus very probable. The 2D case corresponds to a borderline case where the wave configuration is less favorable than the ground state but still accessible at finite temperature.

The 2D spin lattice has been studied in more detail by Mermin and Wagner (1966). Beyond saying that a spin wave configuration is probable, they rigorously proved that a spontaneous magnetization, or sublattice magnetization, is impossible in a 1D and 2D isotropic XY model with short-range interactions at temperature $T > 0$ [43]. This can be viewed as the consequence of the low cost of energy to produce long-range fluctuations in the system, making the ground state unstable. Later (1968), Mermin generalized this observation to 2D crystal. At ground state, particle of the crystal should be localized at the site of the ideal lattice given by $\boldsymbol{R} = n_1 \boldsymbol{a_1} + n_2 \boldsymbol{a_2}$. However, thermal fluctuations induce instability of the order, the displacement $\boldsymbol{u}(\boldsymbol{R})$ of a particle compared to its ideal position diverges with distance

$$\langle [\boldsymbol{u}(\boldsymbol{R}) - \boldsymbol{u}(\boldsymbol{R'})] \rangle \sim \ln[\boldsymbol{R} - \boldsymbol{R'}]. \tag{5.3}$$

This divergence excludes strictly long range translational order. But due to the weak logarithmic divergence, it is still considered a crystal, but now we speak about quasi-long range order.

5.2.2 KT transition

Even if no conventional long-range order exists in 2D systems, Kosterlitz and Thouless (1972) pointed out the existence of a low temperature phase transition, without break of continuous symmetry, whose origin is purely topological. This transition is observed in many systems (XY model, 2D crystals or thin films of helium) highlighting the universal nature of this transition. They proposed a new definition of order called topological order. Kosterlitz, Thouless won the 2016 Nobel prize in physics for this study of topological phase transitions [91]. Now, let us focus on the case of the KT transition in the XY model because it is the most intuitive way to understand the physics behind topological phase transition. It can be caught by a simple calculation concerning a spin lattice in XY model. In that model, the topological defect take the form of a vortex. We speak about a vortex, of vorticity q, if the sum of the angle differences between spins along a closed loop γ in the discrete lattice is

$$\sum_{i,j\in\gamma} (\phi_i - \phi_j) = 2\pi q, \tag{5.4}$$

with $q = 0, \pm 1, \pm 2$, and so on. In Fig. 5.1(left) is represented the simplest vortex, characterized by the field of angle

$$\phi(x, y) = \arctan(y/x), \tag{5.5}$$

where (x, y) is the position of the spins in the lattice, the vortex is assumed to be at $(0, 0)$. The vorticity of such a vortex is ± 1, depending on the orientation of the loop. The energy of this configuration corresponds to the Eq. (5.1) which can be written in a continuous form

$$H = -J \int_x \int_y \cos(\boldsymbol{\nabla}\phi) dy dx \approx -J \int_x \int_y \left(1 - \frac{1}{2}(\boldsymbol{\nabla}\phi)^2\right)) dy dx, \tag{5.6}$$

where the integrals run over the whole lattice. Using the field of angle of Eq. (5.5), one can find that $(\boldsymbol{\nabla}\phi)^2 = 1/r^2$ where r is the distance between a spin in the lattice and the center of the vortex. By passing in cylindrical coordinates, one finds the cost of energy of an isolated vortex in a lattice of size L with spacing lattice a

$$H - E_0 = J\pi \ln(L/a). \tag{5.7}$$

Even if the energy seems to diverge for large systems, one can use a free energy argument to show the existence of a phase transition. Indeed, the number of

possible positions of the core of the vortex in the lattice is $(L/a)^2$, giving the entropic contribution of the vortex

$$S = 2k_B \ln(L/a). \tag{5.8}$$

Consequently, the free energy is

$$F = \ln(L/a)\,[J\pi - 2k_B T] \tag{5.9}$$

and predicts a phase transition at a temperature $T_c = J\pi/2k_B$. When $T > T_c$, the thermal energy is more important than the energy cost of an isolated vortex which is therefore favorable and causes disorder in the system. Oppositely, when $T < T_c$, an isolated vortex is forbidden.

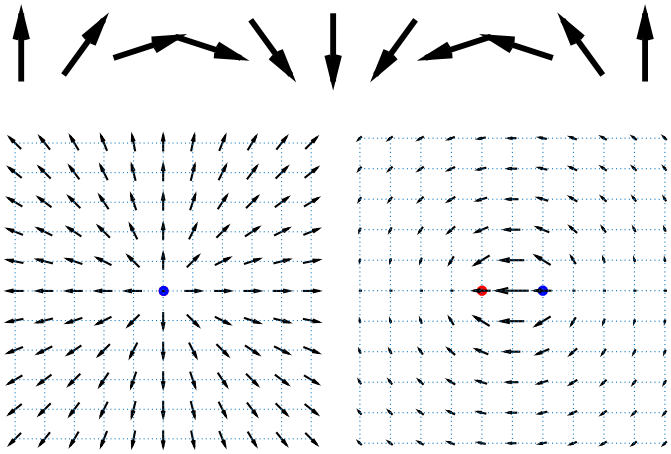

Figure 5.1 – (Top) Illustration of a spin wave. (Left) Positive vortex described by Eq. 5.5. Right: two vortices of opposite vorticity. Blue and red dots correspond to the core of respectively positive and negative vortex.

Below T_c, any macroscopic magnetization occurs, but pairs of opposite vortices appear. Indeed, this configuration has a finite energy so that the configuration is accessible at low temperature. The pair energy of two opposite vortices, separated by a distance r can be calculated and is equal to

$$E(r) = J\pi \ln\left(\frac{r}{a}\right). \tag{5.10}$$

The more two opposite vortices are close, the more the configuration is stable. In addition, two opposite vortices act like two opposite charges in a plasma which leads to screening effect far from the pair. Therefore, a pair of opposite vortices does not affect significantly the whole lattice as illustrated in Fig. 5.1(right). Briefly, the KT transition, the low temperature state of a XY spin lattice is composed of paired opposite vortices which unbind at the KT transition.

5.2.3 2D Crystal melting

In 2D crystal, Kosterlitz and Thouless also predicted a topological phase transition whose mechanisms are perfectly analogous to the KT transition in the XY model. With the difference that the concerned topological defect is no longer a vortex but a dislocation. While the vortex is defined from the orientation field ϕ and characterized by a vorticity q, the dislocation is defined from the displacement field $\boldsymbol{u}$ and characterized by the Burger vector $\boldsymbol{b}$. The displacement field corresponds to the displacement of the lattice sites from their ideal position and the Burger vector $\boldsymbol{b}$ corresponds to the missing distance to close a contour integral of the displacement field enclosing a dislocation, formally written

$$\boldsymbol{b} = \oint d\boldsymbol{u}. \tag{5.11}$$

In the following, we assume a 2D crystal whose ideal lattice is hexagonal. The Hamiltonian of a 2D crystal with a non-zero the displacement field is determined from the theory of the elasticity and corresponds to the cost in elastic energy to move an atom from its ideal position. One can find that the energy of two dislocations, with opposite Burger vector, separated by a distance r is logarithmic similarly to Eq. (5.10) meaning that at low temperature, pairs of opposite dislocations correspond to a favorable configuration. Moreover, a pair of dislocations does not altered order. Nevertheless, one can not speak about long range order due to the instability of the crystal to thermal fluctuations. Actually, a 2D crystal can be seen as random distribution of bound dislocations coupled with low energy thermal phonons. Above a transition temperature, single dislocations become energetically favourable, pairs split up and single dislocations are randomly distributed in the crystal, destroying the order at long range. At that moment (1973) Kosterlitz and Thouless concluded that the dislocation unbinding leads to a perfectly isotropic fluid but, according to their own words, it was an unfortunate mistake [91]. From this basis, Nelson, Haperin (1978) and Young (1979) developed a complete theory about 2D crystal melting. They pointed out that melting is a two-step process with an intermediate phase called *hexatic*. This phase is not a crystal nor an isotropic liquid but an anisotropic liquid with a six-fold symmetry. To understand this two-step melting scenario, it is important to distinguish two types of order: translational order and orientational order. Both are characterized by their own order parameter.

The translational order parameter of an atom at position $\boldsymbol{r}$ in the system is

$$\rho_{\boldsymbol{G}}(\boldsymbol{r}) = e^{i\boldsymbol{G}\cdot\boldsymbol{r}}. \tag{5.12}$$

The position $\boldsymbol{r}$ can be decomposed as the position of the ideal position of the atom in the lattice $\boldsymbol{R}$ and the displacement field $\boldsymbol{u}$ such that $\boldsymbol{r} = \boldsymbol{R} + \boldsymbol{u}(\boldsymbol{r})$. The vector

$\boldsymbol{G}$ is a vector of the reciprocal lattice linked to the ideal lattice, as a consequence $e^{i\boldsymbol{G}\cdot\boldsymbol{R}} = 1$. The correlation of translational order parameter over the whole lattice, called here translational correlation function, is defined as

$$g_{\boldsymbol{G}}(\mid \boldsymbol{r} - \boldsymbol{r'} \mid) = \langle \rho^{\star}_{\boldsymbol{G}}(\boldsymbol{r}) \rho_{\boldsymbol{G}}(\boldsymbol{r'}) \rangle = \left\langle e^{i\boldsymbol{G}\cdot[\boldsymbol{u}(\boldsymbol{r}) - \boldsymbol{u}(\boldsymbol{r'})]} \right\rangle. \tag{5.13}$$

Thermal fluctuations at low temperature induce a logarithmic divergence of the displacement field, mentioned in Eq. (5.3), and consequently the translational correlation function decays algebraically to zero

$$g_{\boldsymbol{G}}(r) \sim r^{-\eta_{\boldsymbol{G}}(T)}. \tag{5.14}$$

For simplicity, we note r instead of $\mid \boldsymbol{r} - \boldsymbol{r'} \mid$. The exponent $\eta_{\boldsymbol{G}}(T)$ is linked to elastic constants of the crystal and depends on the temperature. The maximum value of the exponent is obtained at the melting point $\eta_{\boldsymbol{G}}(T_m) = 1/3$. The behaviour of $g_{\boldsymbol{G}}(r)$ is the sign of no translational long-range order, but the decay is slow enough to speak about quasi-long range order. Above the melting transition $T > T_m$, when pairs of dislocations split up to move freely in the system, the translational correlation function decays exponentially

$$g_{\boldsymbol{G}}(r) \sim e^{-r/\xi(T)}, \tag{5.15}$$

where $\xi(T)$ is the correlation length of the translational order. This exponential decay is the signature of a total loss a translational order in the system. However, this correlation function is rarely used due to the lack of translational order. Consequently, the vector $\boldsymbol{G}$ of the reciprocal ideal lattice cannot be found precisely. Indeed, for a perfectly ordered crystal, the static structure factor

$$S(\boldsymbol{q}) = \left\langle \mid \hat{\rho}(\boldsymbol{q}) \mid^2 \right\rangle \tag{5.16}$$

presents δ Bragg peaks at $\boldsymbol{q} = \boldsymbol{G}$, but with only quasi long range order, these peaks are broad, decreasing the precision on the vector $\boldsymbol{G}$. Note that $\hat{\rho}(\boldsymbol{q})$ is the Fourier transform of the density of the system.

The bond orientational order parameter of an atom with n nearest neighbours is

$$\psi_6(\boldsymbol{r}) = \frac{1}{n} \sum_{i=1}^{n} e^{i6\theta_i(\boldsymbol{r})}, \tag{5.17}$$

where $\theta_i(\boldsymbol{r})$ is the angle formed between the bond linking an atom at position $\boldsymbol{r}$ to its i^{th} nearest neighbor and an arbitrary reference axis. The norm $|\psi_6|$ gives information about the six-fold symmetry of the unit cell composed of an atom and its nearest neighbors. Then $|\psi_6| = 1$ for a perfect hexagonal lattice, $|\psi_{6,i}| < 1$ if the symmetry deviates from the perfect six-fold symmetry and finally, $|\psi_{6,i}| = 0$ if

neighbors of the atom are randomly orientated. This parameter is used to quantify local orientational order. The orientational correlation function is defined as

$$g_6\left(r = \mid \boldsymbol{r_j} - \boldsymbol{r_k} \mid\right) = \left\langle \psi_6^\star(\boldsymbol{r_j})\psi_6(\boldsymbol{r_k})\right\rangle, \tag{5.18}$$

corresponding to the average correlation of the order parameter of two atoms separated by a distance r, $< . >$ denotes an average over each pair of particles.

Mermin [44] studied the influence of a harmonic phonon on the displacement field $\boldsymbol{u}$ of a 2D crystal at low temperature. Interestingly, while the phonon affects order at long range, the orientations of bonds connecting atoms are still correlated at long-range. Consequently, one finds orientational order at long range below the melting point $T < T_m$. This result was confirmed by Nelson and Halperin [57]. Consequently,

$$\lim_{r\to\infty} g_6(r) = c(T), \tag{5.19}$$

where $c(T)$ is constant which depends on the temperature and present a singularity at $T = T_m$. Above the melting transition $T > T_m$, Nelson and Halperin shown that free dislocations in the liquid affect the orientation of atomic bonds. Without going into the details of calculation, they showed a algebraically decay of the orientational correlation function

$$g_6(r) \sim r^{-\eta_6(T)}. \tag{5.20}$$

with $0 < \eta_6(T) < 1/4$. The decay is slow, signature of a quasi-long range orientational order. Surprisingly, above the melting point T_m, Eqs. (5.15) and (5.20) indicate that the system exhibits no translational order but still an orientational order. This phase is a six-fold anisotropic liquid, in between a solid and a purely isotropic liquid. This intermediate phase is called hexatic phase.

However, this orientational order does not persist when temperature increases. A new transition occurs at a temperature T_i. To understand the mechanisms behind the transition, a new kind of topological defect, called disclination, is introduced. In a hexagonal lattice, an atom has six nearest neigbors. As illustrated in Fig. 5.2. An atom with respectively seven (resp. five) nearest neigbors corresponds to a disclination of charge $s = +1$ (resp. $s = -1$). More generally, the disclinity of an atom at point $\boldsymbol{r}$ is

$$s(\boldsymbol{r}) = n(\boldsymbol{r}) - 6 \tag{5.21}$$

with $n(\boldsymbol{r})$ the number of neighbors of the atom at $\boldsymbol{r}$. The transition at T_i is actually perfectly analogous to the KT transition in XY model where the vorticity is replaced by the disclinity. Indeed, the Hamiltonian of a set of disclinations is mathematically similar to the Hamiltonian of a set of vortices in XY model. Thus at $T < T_i$, pairs of opposite disclinations are energetically favorable. Note

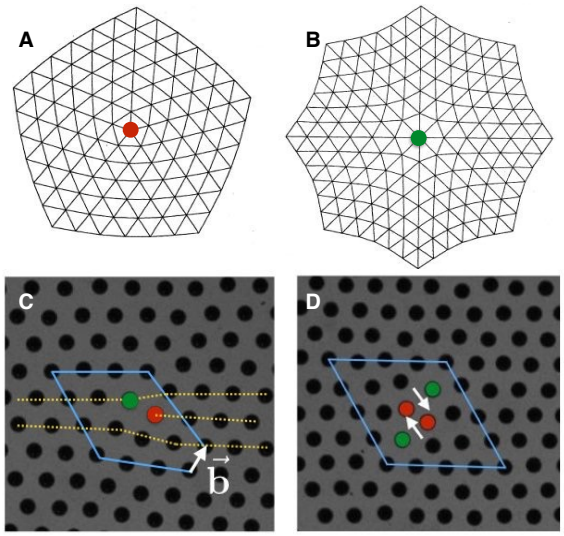

Figure 5.2 – A-B) Five-fold disclination with $s = -1$ and Seven-fold disclination with $s = +1$ (from [100]). C) Pair of opposite disclinations forming a dislocation characterized by a Burger vector $\boldsymbol{b}$. D) Quadruplet of disclinations or a pair of dislocation of opposite Burger vectors.

that such a pair of opposite disclinations is a dislocation (see Fig. 5.2). For $T > T_i$, isolated disclinations in the system become energetically favorable so the free dislocations split to become free disclinations in the system. The result is a perfectly isotropic fluid characterized by an exponential decay of the orientational correlation function

$$g_6(r) \sim e^{-r/\xi_6(T)} \tag{5.22}$$

with ξ_6 the orientational correlation length.

In summary, the KTNHY theory predicts the melting of a 2D crystals in two stages whose origin is topological. During a first transition, translational order is lost due to dislocations unbinding but orientational order remains. A new state of matter is introduced: hexatic phase. At the second transition, orientational order is lost due to disclinations unbinding. The main results of that theory are reported in Table 5.1. In the following, the transition from crystal to liquid that we observe experimentally is confronted to the KTHNY theory of 2D melting.

Table 5.1 – Summary of translational and orientational order, given with respective correlation function, for the different phases according to the KTHNY theory. The last row presents 2D pattern illustrating these phases.

Solid	**Hexatic**	**Liquid**
Quasi-long range translational order $g_G(r) \sim r^{-\eta_G}$ $\eta_G(T_m) = 1/3$	Short range translational order $g_G(r) \sim \exp(-r)$ -	Short range translational order $g_G(r) \sim \exp(-r)$ -
Long range orientational order $g_6(r) = c$ -	Quasi-long range orientational order $g_6(r) \sim r^{-\eta_6}$ $\eta_6(T_i) = 1/4$	Short range orientational order $g_6(r) \sim \exp(-r)$ -
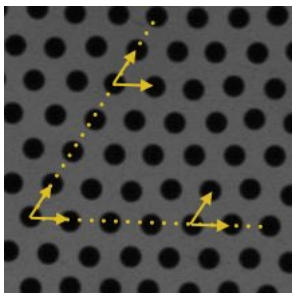	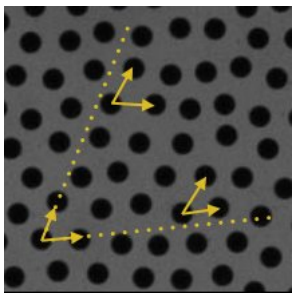	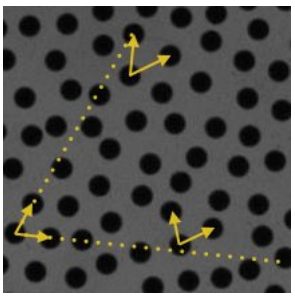

5.3 Experimental details

The experimental setup is presented in detail in Chapter 2, thus in this section are only described the technical aspects specific to the study discussed in this chapter. A set of $N = 547$ spherical metallic beads of diameter $d = 1$mm is placed on a horizontal frosted glass plate and confined in a 3 cm side length hexagonal ferromagnetic cell. Taking into account the repulsion by the wall of the cell, this configuration leads to a particle area density $\rho = 218000$ beads per m^2 corresponding to a filling fraction $\phi = 0.18$.

The plate is shaken horizontally by two shakers oriented in two orthogonal directions, producing two 35 Hz sinusoidal noisy signals. It has been checked that this configuration leads to an erratic motion of each bead in the plane. The set

of beads is placed in the center of two 13 cm diameter coils, with 320 turns, in Helmholz configuration, supplied by a current between 0 and 5A. The strength of the external magnetic field H_0 can be adjusted from 0 to 14000 A/m.

In order to obtain reproducible initial conditions, the beads are placed in a perfect hexagonal configuration, as shown in Fig. 5.3(a), with a lattice parameter set to

$$a = (\frac{2}{\sqrt{3}}\frac{1}{\rho})^{1/2} \tag{5.23}$$

corresponding to the typical distance between two beads in a 2D hexagonal lattice with a particle area density ρ. To form a perfect finite hexagonal lattice with a finite number of beads, the number N of beads has to follow the relation $N = 3p^2 - 3p + 1$, where p is the number of beads on an edge. The experiments are performed with 547 beads which correspond to $p = 14$ beads per edge in the initial state. The initial hexagonal lattice is manually built. For this purpose, we machined a hexagonal piece with the same size as the cell, in which there are 547 holes, each filled by a bead, arrange in a perfect hexagon. This piece is then lifted slowly using screws, leaving the beads perfectly ordered in the cell. The operation is done without agitation and under a strong magnetic field $H_0 = 10000$ A/m to stabilize the assembly of beads.

After the initialization process, the agitation is switched on. After a relaxation time of 200 seconds, a CCD camera records a series of images at a fixed rate of 10 frames per second during 100 seconds. The resolution of the camera in the region of interest is 500×500 pixels. The system is backlighted with a lattice of LEDs and a diffuser. Therefore, the grains and the background appear respectively in black and white. A basic tracking method allows one to determine the position and the trajectory of each bead during the whole experiment. From the beads trajectories, one can measure each static and dynamical parameter. Nearest neighbors are determined using the Voronoi tesselation.

The fundamental principle of this experiment is the competition between the magnetic interaction that induces order and the agitation that generates disorder. To quantify this competition, we introduce the coupling parameter Γ. This dimensionless number is the ratio between the mean pair interactions between beads at a typical separation

$$\langle U \rangle = \frac{\mu_0}{4\pi}\chi^2 V^2 H_0^2 \left(\frac{\sqrt{3}}{2}\rho\right)^{3/2} \tag{5.24}$$

and the mean kinetic energy of the beads

$$\Gamma = \frac{< U >}{\frac{1}{2}m < v^2 >}. \tag{5.25}$$

Note that the coupling parameter can be viewed as the inverse of a dimensionless

temperature. In all experiments of this chapter, the settings of the agitation are fixed, and the control parameter is the external magnetic field strength.

5.4 Results

The different states observed with the 2D assembly of magnetized beads are shown in Fig. 5.3 for typical values of the coupling parameter Γ. The initial state of the system (Fig. 5.3(a)) can be considered at zero temperature and thus $\Gamma = \infty$ because of the lack of agitation. This configuration presents a perfect translational symmetry and a six-fold symmetry which means a perfect translational and orientational order. A clear structural change is observed from $\Gamma = 50$ to $\Gamma = 10$. Indeed, for $\Gamma = 50$ and $\Gamma = 33$ (Fig. 5.3(b-c)), the system exhibits a structure close to the perfect hexagonal lattice with a six-fold symmetry and with a translational symmetry at quasi-long range. For $\Gamma = 16$ and $\Gamma = 12$ (Fig. 5.3(d-e)), the six-fold symmetry persists, but the translational symmetry vanishes. Finally, for $\Gamma = 10$ (Fig. 5.3(f)) the system is completely disordered like a liquid state. A fast Fourier transform of the real lattice obtained from snapshots in Fig. 5.3 enables us to study the pattern of Bragg scattering of the system in Fig. 5.4. For $\Gamma = \infty$ (Fig. 5.4(a)), the reciprocal lattice is hexagonal with a 30° rotation in comparison with the real lattice. At high coupling parameter $\Gamma = 50$ and $\Gamma = 30$ (Fig. 5.4(b-c)), the pattern is close to a perfect hexagonal reciprocal lattice which indicates that the system has a six-fold symmetry. When Γ (Fig. 5.4(d-e)) decreases, a six-fold symmetry is still observable but the spots become more blurred due to the loss of translation symmetry. For $\Gamma = 10$ (Fig. 5.4(f)), spots become a ring, being the sign of the loss of six-fold symmetry as well. These observations are purely qualitative but allow one to observe the phase transitions which will be quantified in the following.

According to the KTHNY theory, the different states of a 2D system can be distinguished by translational and orientational order as summarized in Table 5.1. Predictions about the translational order are made on the behavior of the translational correlation function $g_{\boldsymbol{G}}(r)$ defined in Eq. (5.13). For 2D infinite crystals, the translational correlation function is expected to decrease algebraically but in the hexatic and liquid phase, an exponentially decay is expected. However, the translational correlation function is not often computed in the literature because the reciprocal lattice is not precisely defined due to the lack of translational long-range order [94]. Consequently, the reciprocal vector $\vec{G}$ cannot be determined precisely and $g_G(r)$ neither. In this study, the translational order and the structure are

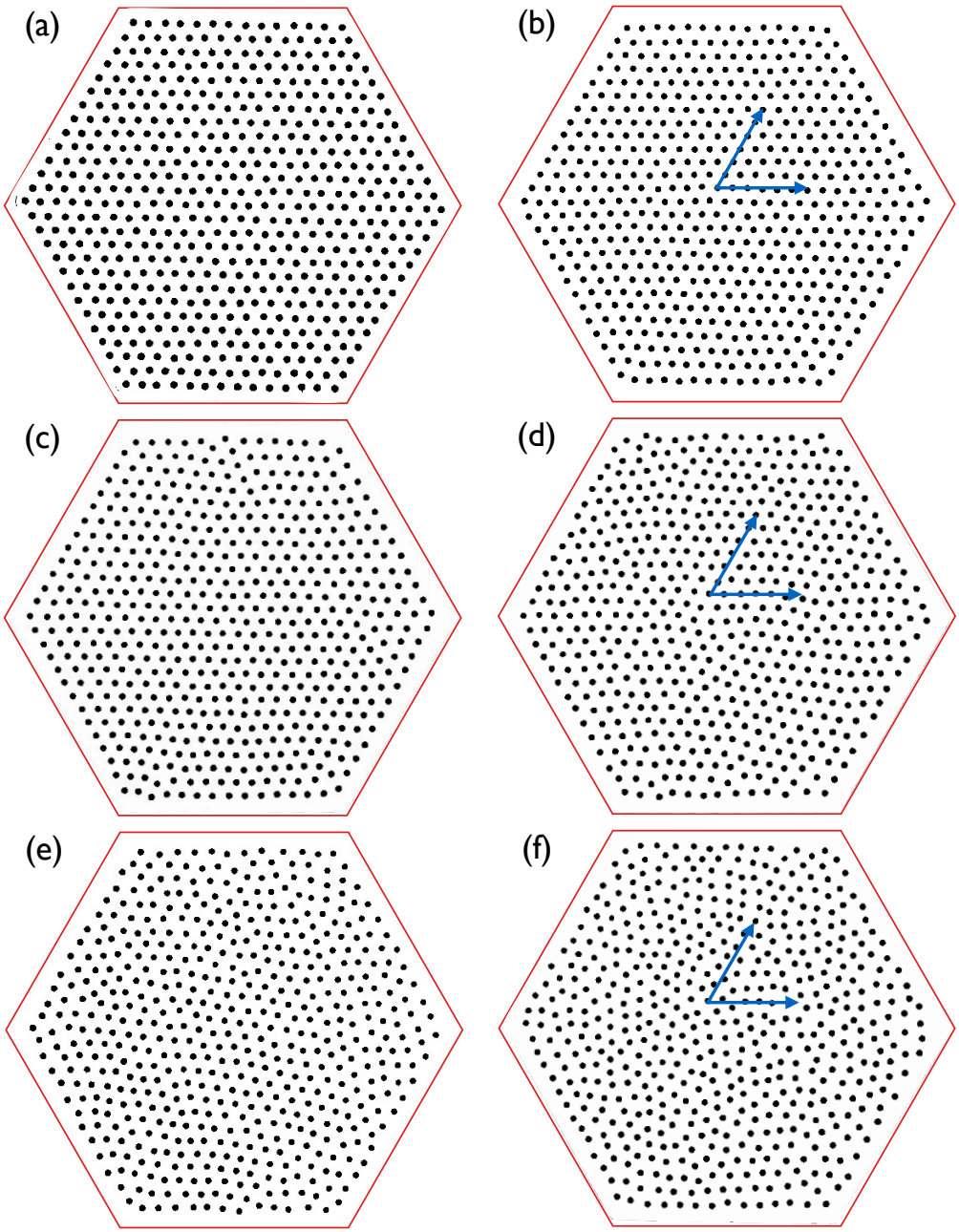

Figure 5.3 – Snapshots of the system for the initial condition considered as $\Gamma = \infty$ (a) and for typical reduced temperature $\Gamma = 50$ (b), $\Gamma = 33$ (c), $\Gamma = 16$ (d), $\Gamma = 12$ (e), $\Gamma = 10$ (f). Blue arrows in (b),(d),(e) form a 60° angle and are drawn to enhance the qualitative lecture of the order for respectively solid , hexatic and liquid phases.

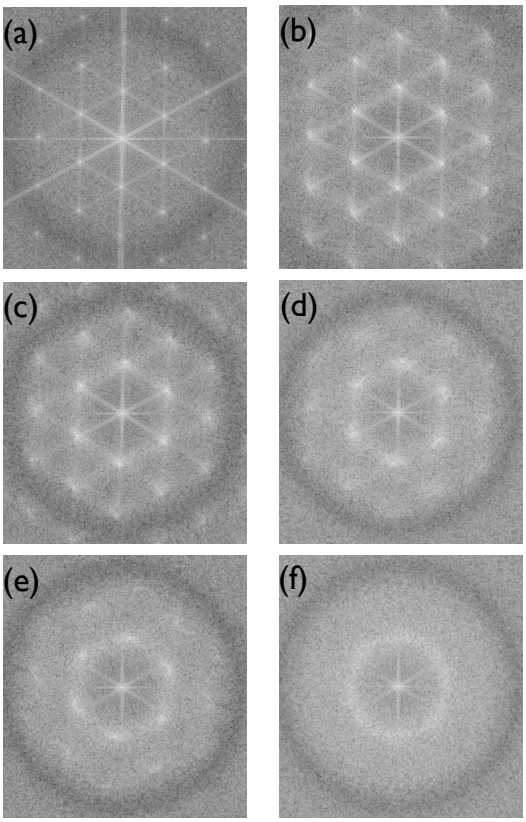

Figure 5.4 – Pattern of Bragg scattering, obtained by Fourier transform of the direct lattice, of the system for the initial condition (a) and for typical coupling parameter $\Gamma = 50$ (b), $\Gamma = 33$ (c), $\Gamma = 16$ (d), $\Gamma = 12$ (e), $\Gamma = 10$ (f).

characterized by the pair correlation function

$$g(r) = \frac{1}{2\pi r N' \rho} \left\langle \sum_{i=0}^{N'} \sum_{\substack{j=0 \\ j \neq i}}^{N'} \delta(r - r_{ij}) \right\rangle, \tag{5.26}$$

This correlation function is linked to the probability to find two particles separated by a distance r. Concretely, $g(r)$ is calculated by counting the number of particles included in a ring of radius r, infinitesimal thickness dr and centered on a reference particle. Then the local area density in that ring is normalized by the global area density ρ. The operation is repeated for all the possible reference particles N' and then averaged. To improve accuracy, a time average is also performed. As a consequence of the normalization, in the case of a homogeneous fluid $g(r) = 1$ meaning that the local density is equal to the global density everywhere. The number N' of particles are used instead of the total number of particle N because particles near the edges are not taken into account because of significant boundary

effect. A region of interest is delimited and corresponds to a circle at the center of the cell, whose radius is half the radius of the cell. The advantage of $g(r)$ over $g_G(r)$ is that it is directly measured in real space, it is thus widely used to study translational order or structural changes upon a phase transition [94, 101, 36]. Fig. 5.5 shows the pair correlation function $g(r)$ for typical coupling parameters Γ. Vertical lines represent the six-first theoretical peaks of $g(r)$ for a perfect hexagonal lattice and follow the sequence $r_1 = a, r_2 = \sqrt{3}a, r_3 = 2a, r_4 = \sqrt{7}a, r_5 = 3a, r_6 = \sqrt{13}a$ with a defined in Eq. 5.23. For strong coupling $\Gamma = 50$ and $\Gamma = 33$, the first peaks are well defined. Nevertheless, peaks widen for longer distance. This behaviour is related to a quasi-long range translational order. When Γ decreases, the peaks get broader and shorter because the probability tends to be uniform like a liquid. Thus, the second and the third peaks merge for $\Gamma < 33$ and the curve becomes flatter at long distance. Therefore, the incertitude on the position increases such that the position of the particles can not be determined even at a short distance so the system is assumed melted. According to this criterion, the pair correlation function shows the loss of translational order, and so the melting, for a coupling Γ included between $\Gamma = 33$ and $\Gamma = 16$.

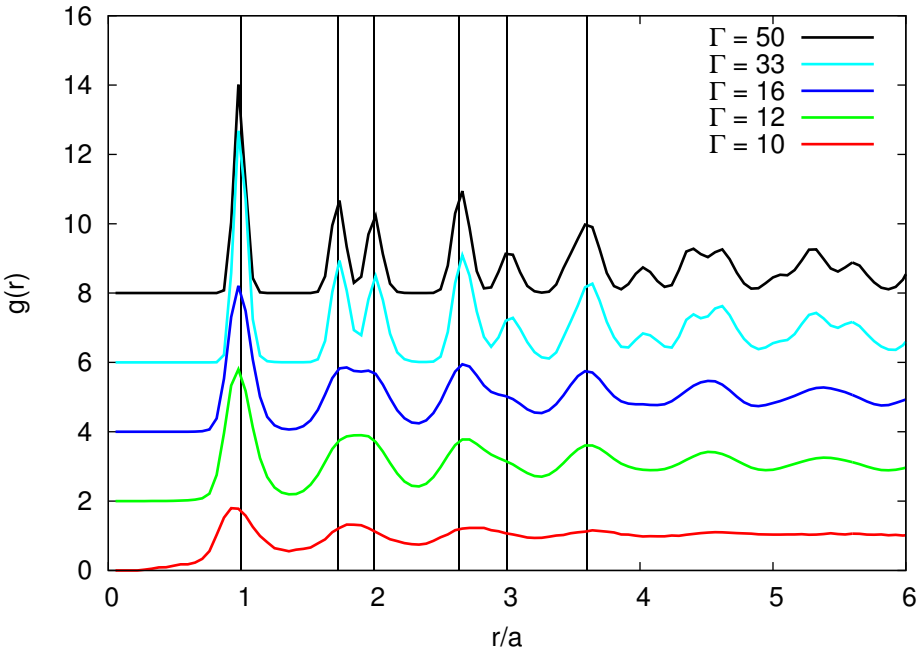

Figure 5.5 – Pair correlation function $g(r)$ for typical coupling parameter Γ. The vertical lines correspond to the theoretical peaks of a perfect hexagonal lattice. Curves are shifted upwards when Γ increases.

The orientational order is quantified by the orientational correlation function $g_6(r)$, used to be defined in literature by Eq. (5.18). In practice, this function is

computed as follows

$$g_6(r) = \frac{\left\langle \sum_i^N \sum_{j\neq i}^N \mathrm{Re}(\psi_6^\star(\boldsymbol{r_i}).\psi_6(\boldsymbol{r_j}))\delta(r-r_{ij}) \right\rangle}{\left\langle \sum_i^N \sum_{j\neq i}^N \delta(r-r_{ij}) \right\rangle}. \tag{5.27}$$

The average is done over each pair and over the time to improve statistic. Let us consider a unit cell (an atom and its nearest neighbors), the norm of the complex number ψ_6, defined in Eq (5.17), gives the degree of local six-fold symmetry, its projection along the real or imaginary axis is related to the local orientation of the unit cell along an arbitrary direction. As the function $g_6(r)$ aims to quantify the mean relative orientation between two unit cells separated by a distance r, we use the real part $\mathrm{Re}(\psi_6^\star(\boldsymbol{r_i}).\psi_6(\boldsymbol{r_j}))$. The imaginary part would give identical results because the system is isotropic. As summed up in Table 5.1, for 2D infinite crystals, $g_6(r)$ tends toward a finite value. In the hexatic phase, an algebraic decay for $g_6(r) \sim r^{-\eta_6}$ is expected where $\eta_6 < 1/4$. In the liquid phase, $g_6(r)$ decreases exponentially. The orientational correlation function is represented in Fig. 5.6(top). One can see that for $\Gamma = 50$ and $\Gamma = 33$, $g_6(r)$ tends toward a constant like a crystal. For $\Gamma = 12$ and $\Gamma = 16$, $g_6(r)$ decays algebraically sign of quasi-long range orientational order which is one of the signatures of the hexatic phase. For $\Gamma = 10$, $g_6(r)$ decays exponentially sign of a liquid state. The green solid line in Fig. 5.6, which corresponds to the algebraic decay with the critical exponent of the hexatic-liquid transition $\eta_6 = 1/4$, is very close to the experimental measurement at $\Gamma = 12$ and suggests so that the transition occurs at this coupling. However, one must be careful because the finite size of the system restricts the quantitative comparison with the theoretical critical exponent. Moreover, a clear distinction between the algebraic decay and the constant behavior appears to be tricky. Fortunately, the acquisition time is far less limited and a temporal orientational correlation function $g_6(t)$ proposed by [60, 99] enables a clear distinction between the solid and hexatic phase, even for a limited number of particles [102]. This correlation function is in fact the temporal counterpart of the orientational correlation function $g_6(r)$ defined as

$$g_6(t) =< \psi_6^\star(t_0+t)\psi_6(t_0) >, \tag{5.28}$$

where the average is over each possible interval time t between two images and over each particles in the system. Here again, the real part is considered to measure the tendency of the orientation of a unit cell to deviate from a reference direction during time. The behavior of $g_6(t)$ as a function of Γ are identical to those of $g_6(r)$, except that in the hexatic phase $g_6(t)$ decreases with an exponent $\eta_6/2$ instead of η_6 [99]. In Fig. 5.6(bottom), $g_6(t)$ is plotted for typical values of Γ. The three

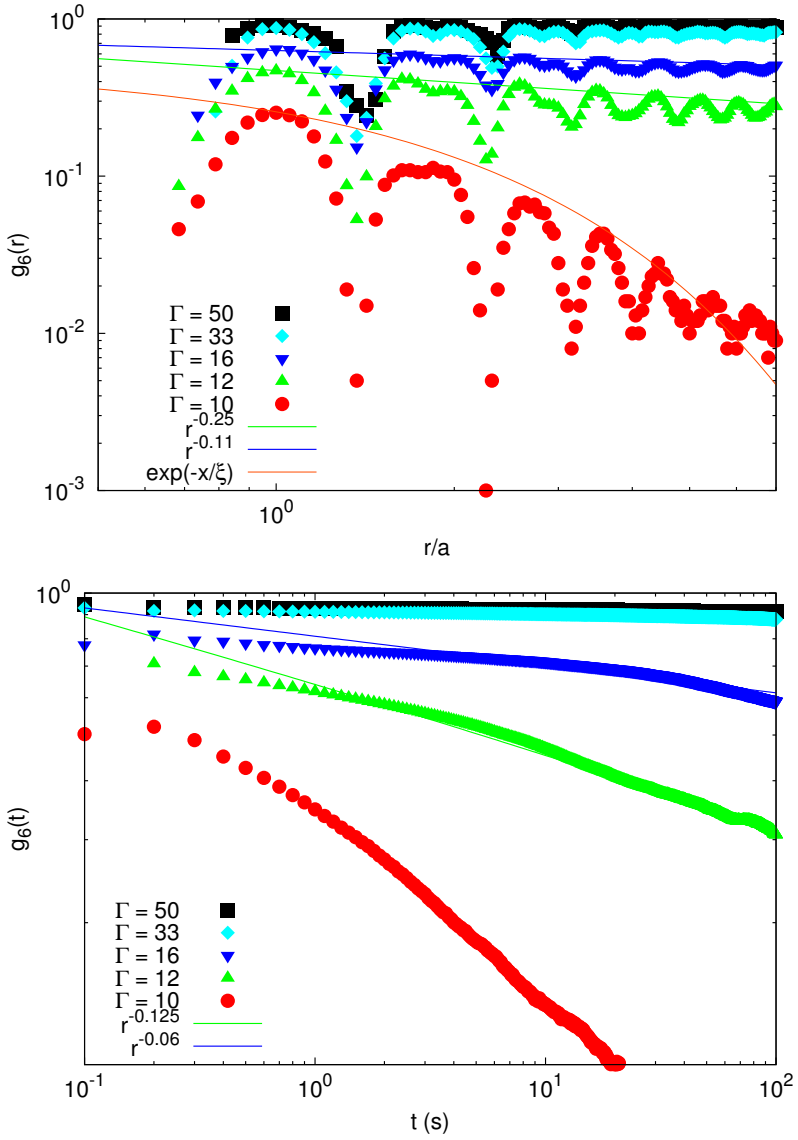

Figure 5.6 – The orientational spatial correlation function $g_6(r)$ (top) for typical coupling parameter Γ. The red curve represents an exponential, and the green curve represents decay with an exponent equal to 1/4 which is the theoretical exponent at the hexatic-liquid transition for an infinite system. Bottom: the temporal orientational correlation function $g_6(t)$ for typical coupling parameters Γ. The green curve represents an algebraical decay with an exponent equal to $\frac{1}{8}$ which is the theoretical exponent at the hexatic-liquid transition for an infinite system.

phases are identically identified as with $g_6(r)$ but the distinction between solid and hexatic is more apparent which disperse any doubt. Moreover, the exponents $\eta_6(\Gamma)$ of $g_6(r)$ perfectly match with exponents $\eta_6(\Gamma)/2$ of $g_6(t)$ as shown by solid lines in Fig. 5.6

Finally, the dynamical transition from solid to non-solid is usually detected using the Lindemann criterion of melting [103]. This is defined as

$$\gamma_M = \langle (\boldsymbol{u}_j - \boldsymbol{u}_{j+1})^2 \rangle / a^2, \tag{5.29}$$

where $\boldsymbol{u}$ is the particle displacement from its ideal position in the lattice. The index j and $j+1$ are corresponding to two neighboring particles and a is the spacing lattice. In 2D system at equilibrium, a system is melted for critical value $\gamma_M^c \geq 0.033$ [104]. The Lindeman criterion can be generalized to a time-dependent criterion [59, 60]

$$\gamma_L(t) = \langle (\Delta \boldsymbol{u}_j(t) - \Delta \boldsymbol{u}_{j+1}(t))^2 \rangle / a^2, \tag{5.30}$$

where $\Delta \boldsymbol{u}(t) = \boldsymbol{u}(t) - \boldsymbol{u}(0)$ is the displacement at time t compared to the initial displacement field. After a long time, equilibrium is reached and the limit of $\gamma_L(t)$ corresponds to γ_M. In a melted state, the particles motion is diffusive and $\gamma_L(t)$ diverges. In a solid state, a particle does not keep away from its neighbors, thus $\gamma_L(t)$ converges to a finite value. At the melting point, $\gamma_L(t)$ converges to the critical value $\gamma_M^c = 0.033$. Fig. 5.7 shows the behavior of such a function for typical Γ. For $\Gamma = 50$ and $\Gamma = 33$, the system is in a solid state because $\gamma_L(t)$ tends to a finite value which is close to γ_M^c indicating that our system presents an equilibrium-like behavior. For higher coupling parameters, $\gamma_L(t)$ diverges. Then the system is considered as melted but not necessarily in an isotropic liquid state.

5.5 Discussion

The association of these correlation functions allows one to determine the state of the system and the phase transitions. For high coupling ($\Gamma = 50$ and $\Gamma = 33$), the behavior of $\gamma_L(t)$ gives a quantitative criterion to detect a solid state. Actually, the system is in an ordered state. Indeed, using the pair correlation function $g(r)$, we have determined that there is a translational order in the system because the positions of the beads match with the positions of atoms in a hexagonal lattice. Nevertheless, peaks become wider at long distance, increasing inaccuracies in the position at long-range, so we have a quasi-long range translational order. And in addition, both orientational correlation functions $g_6(r)$ and $g_6(t)$ tend to a constant indicating a long-range orientational order. Therefore, according to the key statement of the KTHNY theory (see Table 5.1), the system is in a 2D crystals state.

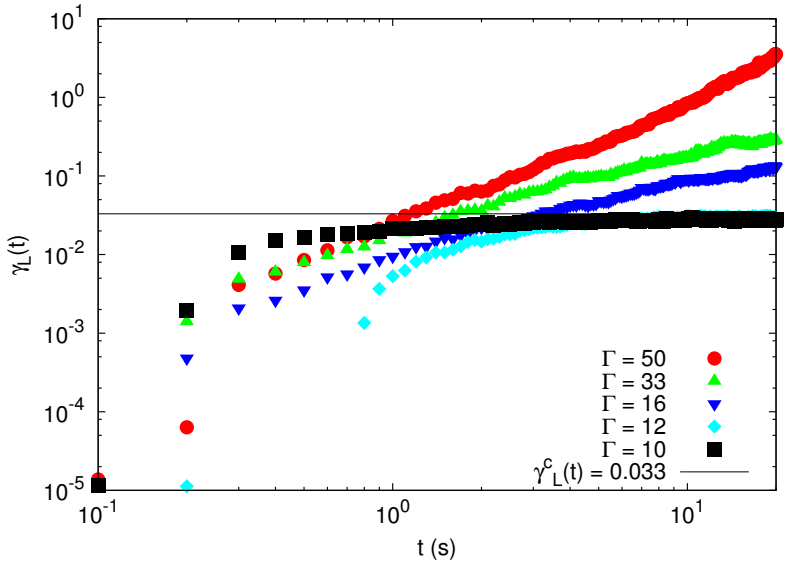

Figure 5.7 – The dynamical Lindemann parameter for typical reduced temperature T^*. The black curve represents the critical value $\gamma_M^c = 0.033$ above which the system is considered melted.

For intermediate coupling parameter $\Gamma = 16$ and $\Gamma = 12$, the system is considered melted due to the divergence of $\gamma_L(t)$. However, the orientational correlation functions $g_6(r)$ and $g_6(t)$ present a slow algebraical decay which is the signature of a quasi-long range orientational order. The state of the system corresponds to an anisotropic liquid, called phase hexatic, which is halfway between the crystal and the isotropic liquid as predicted by Nelson and Halperin. Moreover, the transition from the hexatic phase to the isotropic liquid appears when $g_6(r)$ and $g_6(t)$ decay from algebraically to exponentially with a critical exponent at transition equal to, respectively, 1/4 and 1/8. That transition appears close to the value $\Gamma = 12$.

Finally, for low coupling ($\Gamma = 10$), the correlation functions $g_6(r)$ and $g_6(t)$ decay exponentially. The pair correlation function $g(r)$ shows a liquid-like structure. Moreover, the slope of $\gamma_L(t)$ is close to 1 as a perfect diffusive system. This corresponds to the isotrope liquid phase in the KTHNY theory.

Our experiments bears out that the key results of the KTHNY theory are observable with an athermal system. To go further in the analogy between our experiment and thermal systems, we present in Appendix A a study realized by R. Messina *et. al.*. Our experimental results are compared to computer simulations and experiments performed with a thermal colloidal system, both at equilibrium. Excellent quantitative agreement throughout our range of the coupling parameter Γ is found for $g(r)$ and $g_6(r)$. Thus, our experimental model system appears to be

very effective to mimic thermal systems at equilibrium.

5.6 Conclusion

In conclusion, we have developed a set-up to study an athermal system where the magnetic dipole-dipole pair interaction and the agitation are controlled. Moreover, care has been taken to agitation which leads to an erratic movement of the beads in agreement with the kinetic theory of gases. By adjusting the ratio between the pair interaction and the kinetic energy of each bead, the signature of the three phases (solid-hexatic-liquid) predicted by the KTHNY theory have been observed through both dynamic and static parameters.

Despite its athermal and out of equilibrium character, the system described here is in agreement with the KTHNY 2D melting theory. Thus, our experiment can be considered as a model system to study 2D systems.

5.7 What about defects?

In this study, the key predictions of the KTHNY theory are observed but what about the assumptions underlying this theory, namely, the transition by defects unbinding? Actually, this represents a delicate point in many experiments and simulations. Indeed, many systems reproduce the predicted behaviour of the correlation functions and thus a two-step melting including the hexatic phase. However, observed topological defects are complex and not consistent with the simple KTHNY scenario because defects tend to cluster together rather than being sprayed in the system [105, 106, 107]. Our observations agree with these studies. In the left column of Fig. 5.8, the Voronoi and Delaunay tesselation are used to visualize defects and order. Contrary to the KTHNY theory picture for liquid, defects in the system do not take the form of a gas of isolate disclinations but agglomerate as clusters of defects, sign of a more complex and collective behaviour than predicted. However, in the hexatic phase we find back the predicted picture, a majority of isolated dislocations and the Delaunay triangulation does not display straight lines throughout the system, a clear sign of the loss of translational order. In the solid phase, dislocations are few but still isolated which should destroy the translational order but it is not the case. Therefore, it seems that only characterizing a defect by its number of neighbors is not sufficient to describe its effect on the system. In that purpose, the right column of Fig. 5.8 displays the norm of the bond order parameter of each bead, represented as a color scale from white for $\mid \psi_6 \mid = 1$ to black for $\mid \psi_6 \mid = 0$, allowing us to visualise the distortion of a cell compared to a perfect hexagon. Defects remains colored in red and green. In the solid phase, very close to the isolated dislocations, weak deformations are observed but not enough to change the coordinate number but enough to restore the translational order locally. On the contrary, the deformations are more important in the hexatic phase, and they spread far from the defects. Significant distortions are also observed in between two distant defects. Although the majority of the cells are not deformed, sign of global orientational order, they are still deformed in many places, even far from defects.

An open question remains: are these configurations of defects as well as their non-agreement with the KTHNY picture due to confinement and the finite size effect? Our intuition is that the size and the geometry of the confinement plays a crucial role in the number and location of defects in the system. Chapter 6 is dedicated to this thematic and the study of topological defects in confined geometry near the ground state.

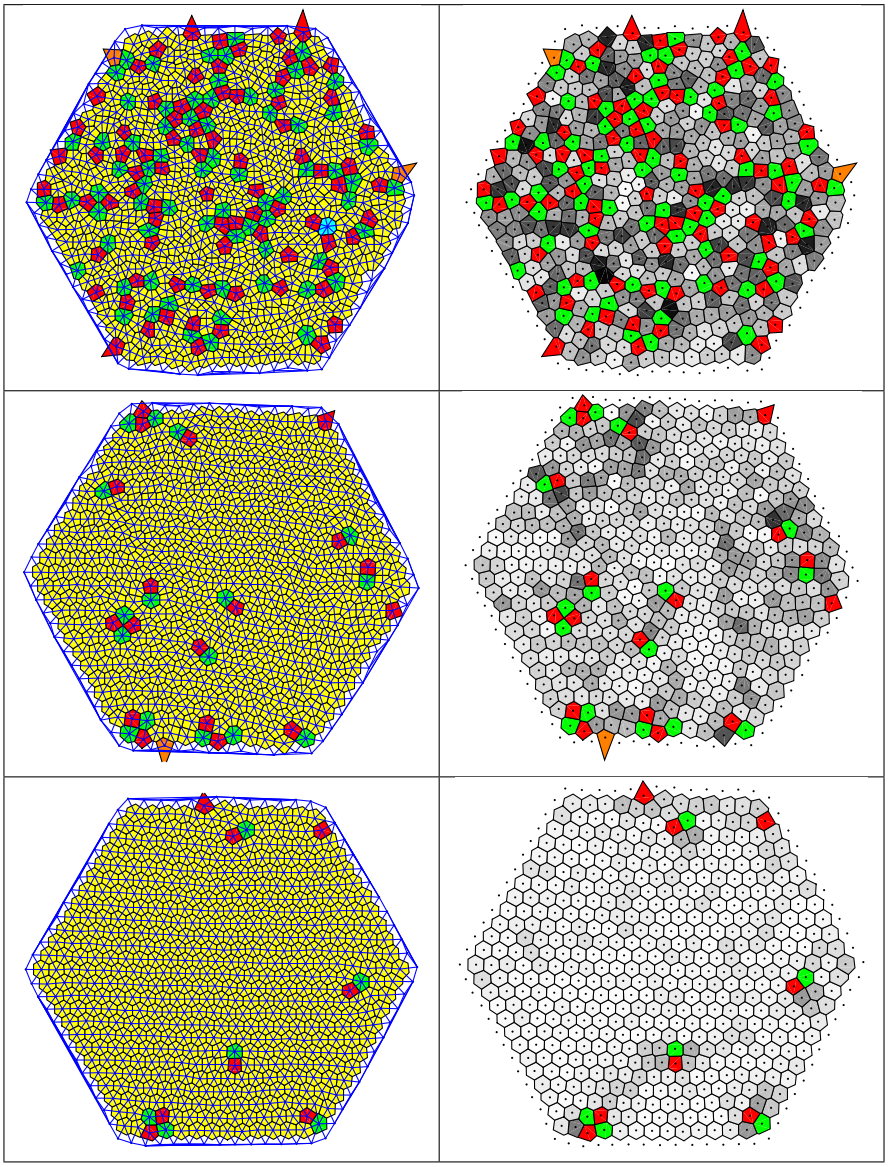

Figure 5.8 – Left column: Voronoi diagrams and Delaunay triangulations for, from top to bottom, liquid ($\Gamma = 10$), hexatic ($\Gamma = 21$) and solid ($\Gamma = 41$). Beads with respectively fivefold, sixfold and sevenfold coordination are colored in red, yellow and green in the Voronoi diagram. Voronoi cells for beads at the boundary are not shown for clarity. Right column: bond order parameter $\mid \psi_6 \mid$ color mapping of the system from white for $\mid \psi_6 \mid = 1$ to black for $\mid \psi_6 \mid = 0$.

6 Frustrating confinement

J. Schockmel, N. Vandewalle, E. Opsomer and G. Lumay,
Frustrated crystallization of a monolayer of magnetized beads under geometrical confinement
Phys. Rev. E **95**, 062120 (2017).

6.1 Introduction

For an infinite assembly of identical particles with isotropic interaction, the hexagonal lattice without defects represents the fundamental structure of a crystal. Topological defects play a key role in the study of the melting of 2D systems [45, 46, 56, 57, 58], the morphology of cells colonies [84], the propagation of cracks [108], and the physical properties of materials [109, 110, 111, 112] such as mechanical properties, electrical and thermal transport. Thus, controlling the number and the type of defects offers an interesting way to tune material properties. Curved surfaces, polydispersity or geometrical confinement lead to the appearance of defects. Due to the large number of biological and physical systems formed on curved backgrounds, the link between defects in 2D crystals and curved surfaces has been extensively studied, adopting two different points of view. On the one hand, the crystal is wrapped on a fixed curved surface (spheres, paraboloids, tori and others), imposing defects [113, 114, 115, 116]. On the other hand, defects are frozen within the crystal inducing the buckling of the surface [73, 117]. In flat geometry, defects are statistically introduced by temperature [62] or forced by frustrations, like polydispersity [118, 119] or with geometrical confinement [120, 121, 122]. The study of the structure and the behavior of confined systems, with strong finite size effect, is new and motivated by the emergence of new technologies such as quantum dots [123, 124] or nanomaterials leading to nanoconfinement [75, 79, 125, 126, 127].

Many studies have shown that the nature, the size, and the geometry of the spatial confinement can affect the dynamics of the system near the boundaries

[128, 129, 78], the melting scenario [122, 130, 131, 132, 133] and the structure of the system [121, 122, 130, 131, 133, 134, 135, 136, 137]. Moreover, the low-energy configuration of small systems, composed of a few dozen particles, is dominated by the geometry of the confinement, whether for a circular, square, hexagonal or pentagonal geometry [122, 135]. To our knowledge, only circular and hexagonal confinements have been studied for larger systems, composed of few hundred particles [121, 132, 133, 134, 136, 137]. In Chapter 5, we show that our experimental setup is suitable to study this issue.

In this chapter, we present a systematic study of the effect of the confinement on the low-energy state of the system composed of few hundreds of millimeter-scale beads, with magnetic dipole-dipole interaction, for a triangular, square, pentagonal, hexagonal, heptagonal and circular geometries of confinement with a homogeneous distribution of the particles within the cell.

6.2 Experimental details

The experimental setup is detailed in Chapter 2. In this section, main characteristics of the set-up are recalled, and settings linked particularly to the study of this chapter are explained. A monolayer of $N = 331$ soft ferromagnetic beads of diameter $d = 1$mm is confined in 2D horizontal cells of different geometries but identical surfaces $S = 1050$ mm^2. The beads are immersed in a vertical and homogeneous magnetic field H_0, produced by two 19 cm diameter coils in Helmholtz configuration, inducing magnetic dipole moments. The mean magnetic interaction energy between two beads is therefore

$$\langle U \rangle = \frac{\mu_0}{4\pi} V^2 \chi_m^2 H_0^2 \left(\frac{\sqrt{3}}{2} \rho \right)^{3/2}, \tag{6.1}$$

where ρ is the particle area density and $\left(\frac{2}{\sqrt{3}}\frac{1}{\rho}\right)^{1/2}$ is the typical distance between two beads. The interactions are therefore well controlled by adjusting the strength of the external magnetic field H_0 ranging from 5000 A/m to 12000 A/m. Moreover, under an external magnetic field, the walls are repulsive and confine the beads with a homogeneous area density. The cell is horizontally excited by two perpendicular electromagnetic shakers producing a 2D Brownian motion of the beads as shown in Chapter 4. In a preliminary work of this study, the mean kinetic energy of the beads is measured at an appropriate frame rate allowing us to estimate the coupling parameter

$$\Gamma = \frac{\langle U \rangle}{\frac{1}{2} m \langle v^2 \rangle}. \tag{6.2}$$

All experiments are fully controlled by a Labview routine and follow the same protocol: during two seconds, a 12000 A/m magnetic field is generated to spread

homogeneously the set of beads in the cell. Then, simultaneously, the agitation is switched on and the magnetic field starts a linear increase from 5000 A/m to 12000 A/m during 200 seconds, corresponding to a slow cooling of the system from $\Gamma = 10$ to 70. Afterward, the magnetic field remains at 12000 A/m during 30 seconds. This slow cooling allows the system to reach its stationary and equilibrium-like state, considered a crystal phase. Otherwise, the system would solidify in an amorphous state. A CCD camera records a series of images at a fixed rate of 1 frame per second during the cooling process described above. The experimental protocol is the same for the complete set of shown in the present chapter. Two parameters are investigated: (i) the shape of the cell and (ii) the size of the cell. For the size effect study, the numbers of beads chosen are N =169, 331 and 721, satisfying the relationship giving the number of grains needed to fill a finite hexagonal lattice

$$N = 3p^2 - 3p + 1, \tag{6.3}$$

where p is the number of beads on an edge. Depending on the number of beads, the surface of the cell is adjusted such that for each experiment, the filling fraction is fixed to $\phi = 0.24$ and the particle area density is $\rho = 315250$ beads per m^2.

6.3 Results

6.3.1 Degree of ordering

The local order is characterized by the bond order parameter of a bead k

$$\psi_{6,k} = \frac{1}{n} \sum_{j=1}^{n} e^{i6\theta_{kj}}, \tag{6.4}$$

where the sum is carried out over the n nearest neighbors and θ_{kj} is the angle between the horizontal axis and the bond linking the particle k and its neighbor j. The modulus of the bond order parameter $\left|\psi_{6,k}\right|$ gives information about the six-fold symmetry of the unit cell composed of the beads k and its first neighbors. Therefore $\left|\psi_{6,k}\right| = 1$ when the unit cell follows a perfect sixfold symmetry, $|\Psi_{6,i}| < 1$ when the symmetry deviates from the perfect six-fold symmetry and $\left|\psi_{6,k}\right| = 0$ when the neighbors of the beads k are randomly orientated. The average over all the beads, excluding those near the walls, gives the global orientational order ψ_6 of the system. One has,

$$\psi_6 = \langle \left|\psi_{6,k}\right| \rangle. \tag{6.5}$$

The evolution of this global orientational order during the cooling process for $N =$ 331 beads is reported in Fig. 6.1. For each cell geometry, the order parameter ψ_6 saturates during the cooling, indicating that the maximum degree of order is

achieved by the system. For each geometry, the final state of the system exhibits a global orientational order $\psi_6 > 0.8$, ensuring that the system is in a crystalline state [36] and not trapped in an amorphous state.

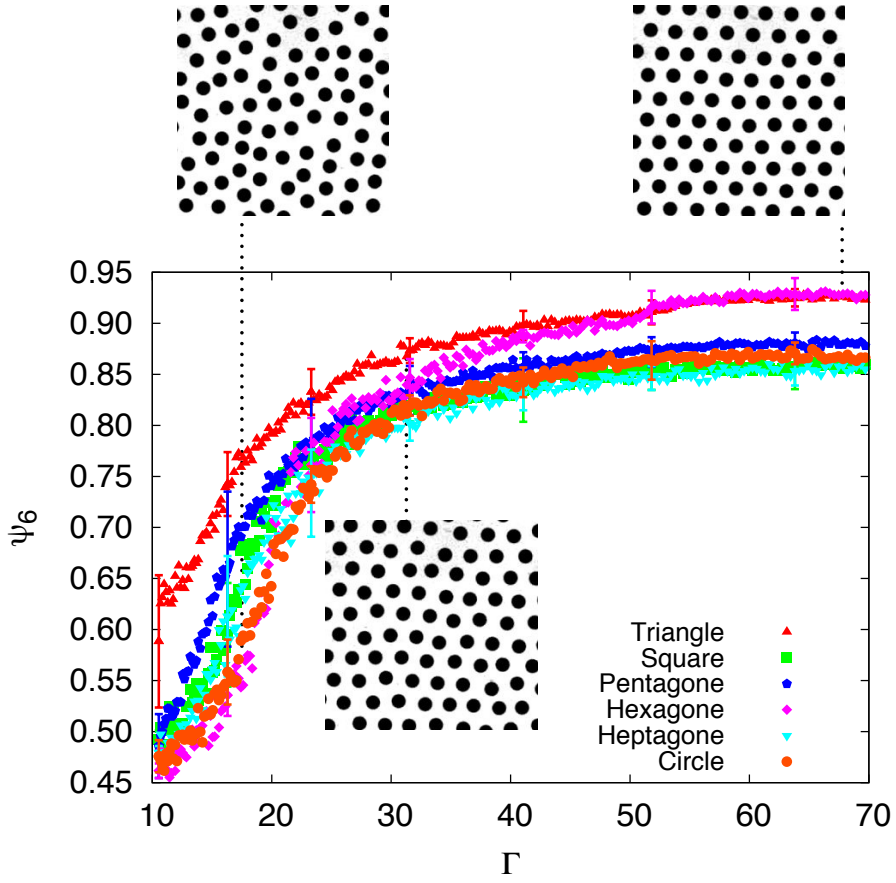

Figure 6.1 – Evolution of the global orientational order ψ_6 during the 200 seconds cooling process for N = 331 beads. For each geometry of the cell, the points correspond to an average over three independent experiments. Typical error bars corresponding to the standard deviation are indicated.

The final value of ψ_6 for each geometry is reported in Fig. 6.2. As expected, the final value of ψ_6 for both triangular and hexagonal cell shapes is higher than the value obtained with other cell geometries. Indeed, the triangular and hexagonal cell shapes are compatible with the hexagonal lattice formed by the beads. Incompatibilities between cell shape and hexagonal lattice induce the presence of defects and reduce the global orientational order ψ_6. Note that the state reached by the system is not the ground state but a low-energy state. Therefore, If the cell geometry is not compatible with the lattice, the system is frustrated which is a source of disorder leading to a competition between many low-energy states. We

show hereafter that this competition allows one to observe a wide range of defect types.

It has been checked that the equilibrium value of ψ_6 is robust for a change in the filling fraction ϕ. For a variation of ϕ from 0.20 to 0.28, the mean final values of ψ_6 and their standard deviation are equivalent to those presented in Fig. 6.2.

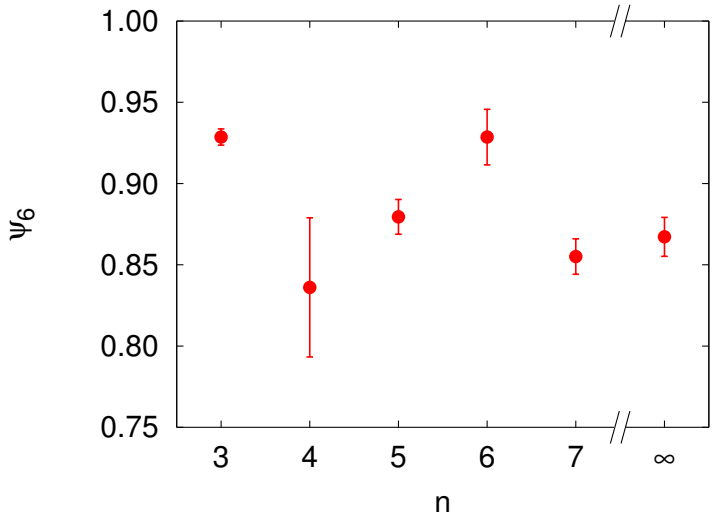

Figure 6.2 – Global bond order parameter ψ_6 at the end of the cooling process as a function of the number n of edges of the cell. The error bars are corresponding to the standard deviation of ψ_6 over three independent experiments.

6.3.2 Defects

In a hexagonal lattice, the topological charge allocated to a particle i is defined as $Q_i = 6 - n_i$ for a particle belonging to the bulk and $Q_i = 4 - n_i$ for a particle at the boundary, where n_i corresponds to the coordination number of the particle i. The coordination number is determined using the Delaunay triangulation [138]. The total topological charge of the system must satisfy the Euler condition *i.e.* $\sum_i^N Q_i = 6\chi$ where χ is the Euler characteristic and is equal to 1 for open surfaces with boundaries. We checked that this condition is always satisfied in our system whatever the confinement geometry. Fig. 6.3 shows snapshots of the system in the low-energy state for each geometry. The beads with six-fold (Q = 0), five-fold (Q = 1) and sevenfold (Q = -1) coordination numbers are respectively colored in yellow, red and green in the Voronoi tessellation. Many types of defects [121] have been observed in our system. An isolated particle with a nonzero topological charge is a disclination. A pair of five-fold and seven-fold disclinations is a dislocation. Defect chains, also called grain boundary, are alternating five-fold and seven-fold

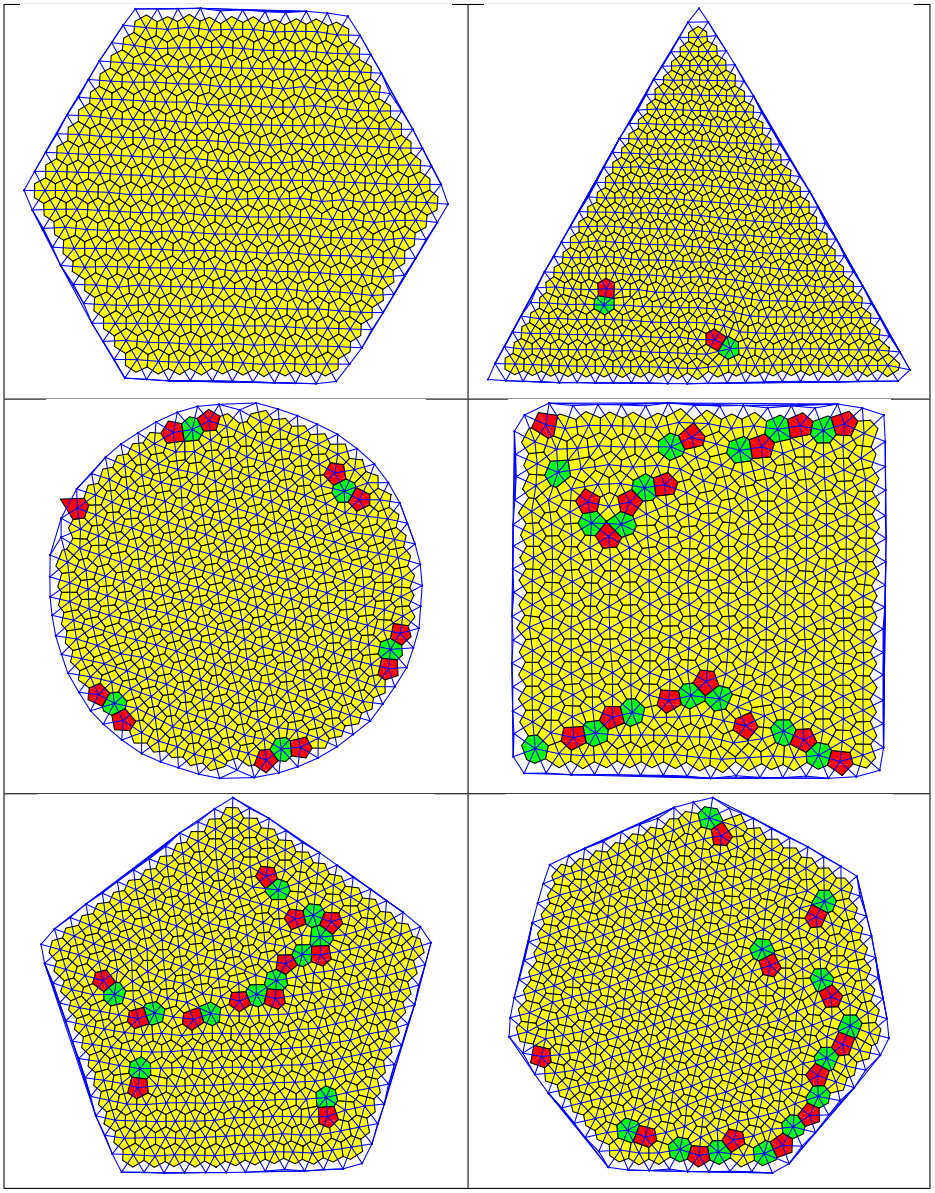

Figure 6.3 – Voronoi diagrams and Delaunay triangulations for each geometry with N = 331 beads. Beads with respectively fivefold, sixfold and sevenfold coordination are colored in red, yellow and green in the Voronoi diagram. Voronoi cells for beads at the boundary are not shown for the sake of clarity.

disclinations. These chains can be topologically neutral or charged. A scar is the most rudimentary defects chain, only composed of two five-fold and one seven-fold disclination. Most of the defects are observed as a chain with variable sizes or in the form of topologically charged cluster. Fig. 6.4 (left) shows a particularly well organized cluster with a +1 topological charge, called a rosette, with a fivefold symmetry. No neutral cluster have been observed. A topologically neutral defect is responsible for the loss of translational order and according to the KTHNY theory [45, 46, 56, 57, 58], the topologically charged particles are responsible for the loss of orientational order. A charged defect tends to create curvature in crystal lines [114, 139]: a lattice line is concave near a +1 defect and convex near a −1 defect as illustrated in Fig. 6.5. The more two particles of opposite charges are close, the less it affects the overall orientation order. It should be noted that a positive (resp. negative) defect induces a curvature of the lattice lines identical to those of a lattice wrapped on a curved surface such as a paraboloid (resp. a saddle) [114].

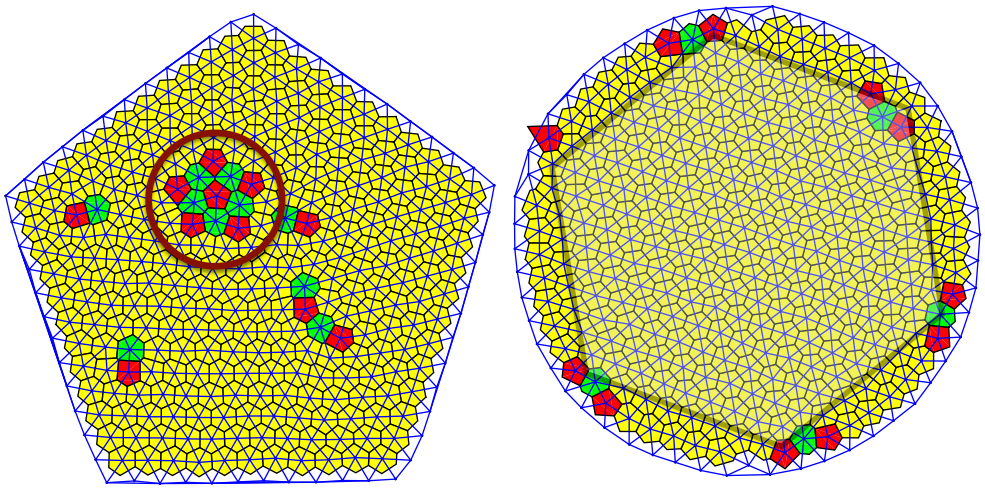

Figure 6.4 – (Left) Rosette defect in a pentagonal confinement. (Right) Six topologically charged defects near the boundary drawing a hexagon with the same orientation as the lattice.

The observation probability of a topologically charged particle in the bulk belonging to a defect type, as described below, is reported in Fig. 6.6. The defects are at least counted over 993 particles for each geometry. The cell geometry influences both the number and the distribution of defects among the different types listed. The mean number of topologically charged particles $\langle N_D \rangle$ depends on the geometry of the confinement and can be directly related to ψ_6.

We have observed that the cell geometry influences the spatial distribution of the defects in the system. Fig. 6.7 presents the cumulated radial distribution

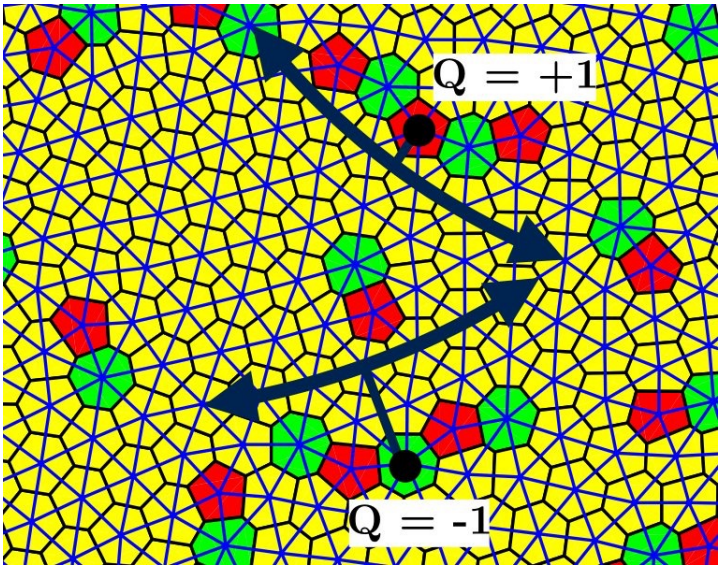

Figure 6.5 – Defect chains with $Q = +1$ and $Q = -1$, black points are the center of the chains. Solid lines highlight the curvature of lattice lines near these defects.

of the topologically charged particle $N_D(r)$ for 331 beads and for each geometry. Hexagonal and triangular cell geometries are not shown due to the lack of defects in these geometries. The cell geometry is found to affect significantly the radial distribution $N_D(r)$. In pentagonal cells, the defects are distributed everywhere in the cell with the exception of the outer region containing only a few defects (mostly dislocations) which do not belong to a large chain or to a cluster. In contrast, all the defects in a circular cell are located in the outer region. Defects in squared or heptagonal cells are located everywhere but are more rare in the center.

Since the selected bead number satisfies Eq. (6.3), almost no defects have been observed in the hexagonal cell with the exception of rare dislocations because the system is not in the ground-state. Therefore, a nonzero probability to observe dislocation exists. In any case, the total topological charge in the bulk is $Q_{bulk} = 0$ and the defects to at the boundary appear at the six corners of the cell in order to respect the Euler theorem.

Even if the triangular geometry is compatible with the hexagonal lattice, some dislocations are observed. Indeed, to fit a perfect hexagonal lattice within a triangular cell, the number of beads should follow the relation $N = p(p+1)/2$ which is not satisfied. As dislocations are topologically neutral, the total topological charge in the bulk is $Q_{bulk} = 0$ and two charged particles per corner are present at the boundary.

Crystals confined in a circular geometry has been widely studied, and our

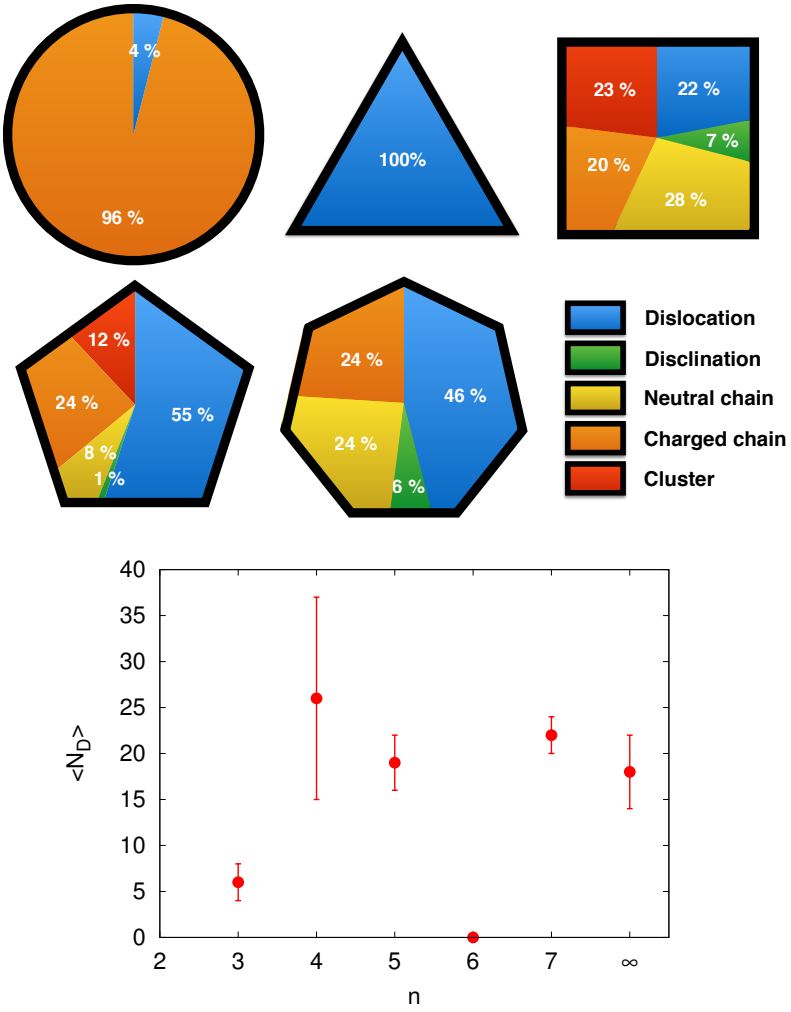

Figure 6.6 – (Top) Observation rate of a topologically charged particle in the bulk belonging to a dislocation, a disclination, a neutral chain, a charged chain, or a cluster for each geometry with an $N = 331$ beads system. (Bottom) $\langle N_D \rangle$ is the averaged number of topologically charged particles observed in an experiment. Error bars are the standard deviation over three independent experiments.

results are in agreement with the observations reported previously [132, 130, 131, 134, 121]. Defects are drained out to the boundary, thus a monodomain crystal with a hexagonal lattice is well defined in the bulk. Near the boundary, six defects with a +1 topological charge draw a hexagon with the same orientation as the lattice (see Fig. 6.4 (right)). Unlike the hexagonal and triangular cells which fix the crystal orientation, the circular cell does not impose any privileged crystal orientation. For each independent experiment, a random global orientation of the crystal is observed.

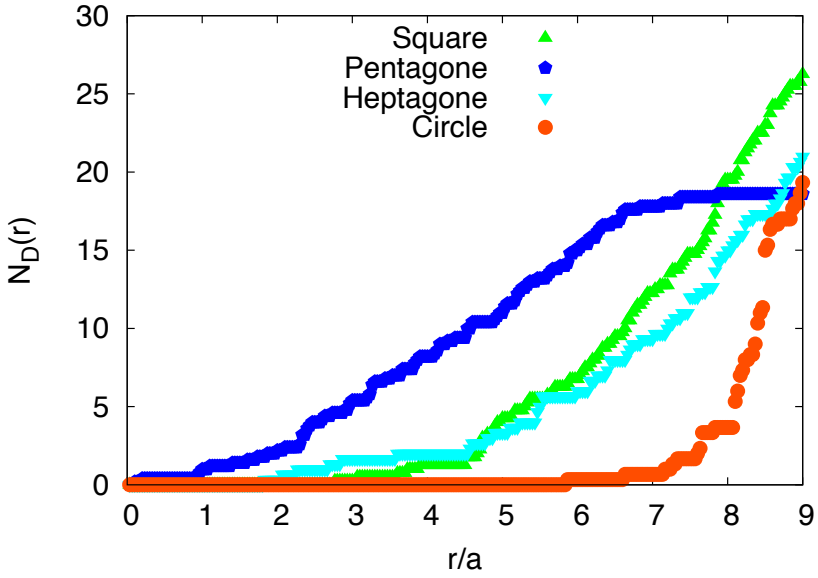

Figure 6.7 – Cumulated radial distribution of defects $N_D(r)$ after the cooling process for square, pentagonal, heptagonal and circular geometries for N = 331 beads. The distance r from the center is normalized by lattice spacing a.

In the square cell, the orientation of the lattice is directed by two parallel edges among the four edges of the cell because the cell and the lattice are sharing a mirror symmetry. As a consequence, the defects are situated near the two frustrated edges and are aligned to form two grain boundaries. Despite these defects near the edges, we observe a large monodomain following a hexagonal lattice between the two grain boundaries, as illustrated in Fig. 6.3. In this geometry, the defect positions are well determined, but the nature of the defects is diversified: dislocations, neutral and charged grain boundaries and clusters have similar occurrence probabilities. The global bond order parameter ψ_6 is associated with a large error bar for the squared cell (see Fig. 6.2) because the structure of the system significantly changes from one experiment to another, meaning that the square confinement represents a strong frustration for a hexagonal lattice.

For each experiment in the pentagonal cell, five topologically charged particles are found at the boundary: one at each corner of the cell. Therefore, the total topological charge in the bulk is $Q_{bulk} = +1$, in agreement with the Euler condition. This positive residual defect usually takes the form of a positively charged chain of defects or a more exotic defect as the rosette in Fig. 6.4(left). As a consequence, this residual defect curves the lines of the lattice which appears thus distorted. In the other geometries, this phenomenon is not observed because charged defects are rather located close to the boundaries or close to a defect with an opposite charge. Moreover, a long chain of defects situated in the middle of the bulk is actually a

grain boundary which divides the crystal into two distinct domains with different orientations.

In the heptagonal cell, the observation of one positive boundary defect at each corner associated with a negative defect in the bulk could be expected. However, this defect distribution has not been observed. In all experiments, positive boundary defects are localized only at six of the seven cell corners and in the condition $Q_{bulk} = 0$ is always respected. In each independent experiment with a heptagonal cell, we observe one positive defect and one negative defect separated by a significant distance ($\approx 10a$). Both the positive and negative defect alters the orientational order leading to a global distortion in the lattice.

6.3.3 Cell size effect

The effect of the confinement size has been studied. Fig. 6.8 showsl value of ψ_6 after the cooling for pentagonal, hexagonal and circular geometries for N = 169, 331 and 721 beads with an identical filling fraction $\phi = 0.24$. The lines are guides for the eyes and correspond to a linear fit for the hexagonal, pentagonal and circular geometries. For each geometry, ψ_6 converges to a unique value for large systems. Nevertheless, the finite size of the system affects the particle ordering.

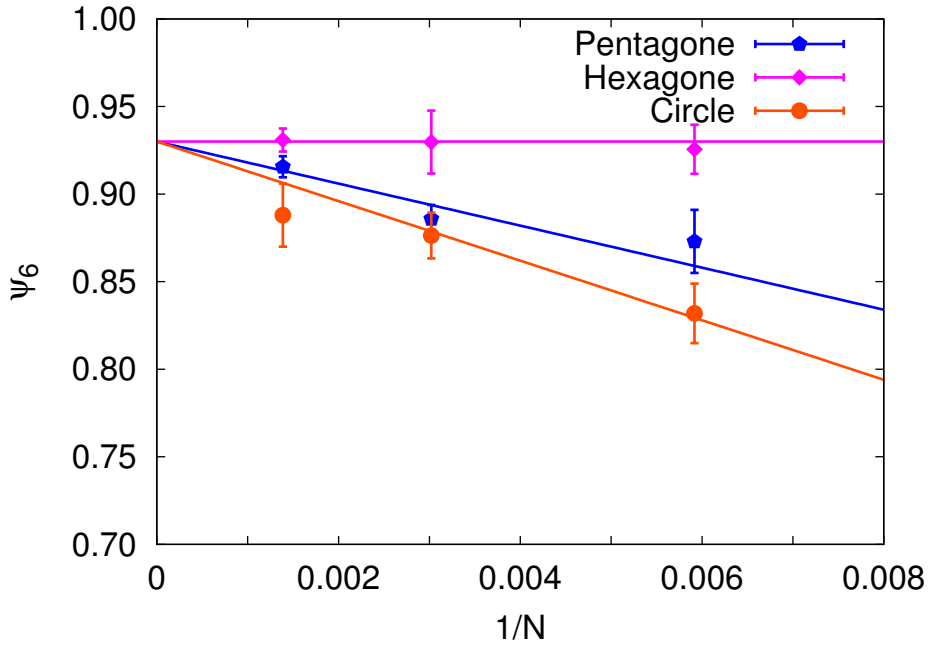

Figure 6.8 – Final value of ψ_6 for pentagonal, hexagonal and circular geometries for N = 169, 331 and 721 beads at constant filling fraction. Solid lines correspond to a linear fit.

As discussed in subsection 6.3.2, the nature of the defects depends on the cell geometry. Therefore, it is not surprising to observe that the finite-size effect is different for hexagonal, pentagonal and circular geometries. No finite-size effect is observed for the hexagonal confinement because this cell geometry induces the formation of a nearly perfect lattice. Indeed, the selected bead numbers N = 169, 331 and 721 are in agreement with Eq. (6.3).

The global order of the systems is more affected for small cell sizes in circular confinement than in pentagonal confinement because in a curved boundary, the smaller the system is, the more the radius of curvature increases and prevents the hexagonal order.

6.4 Conclusion

The model experimental setup, previously validated to study 2D phase transitions [67, 68], has been used to perform a systematic study of the confinement effect on the crystallization of a magnetized beads monolayer. The temperature is simulated by a mechanical agitation inducing Brownian motion of the beads. A slow cooling process from a liquid state to a solid state is used to reach the low energy state of the system. We show that the geometry of the cell affects the type and the number of defects in the systems. In particular, the influence of both cell size and cell shape on the global bond order parameter ψ_6 is analyzed. This order parameter is higher for triangular and hexagonal cells compared to squared, hexagonal, heptagonal and circular shaped cells. Moreover, the order increases with the grain number N for constant filling fraction.

The type of defects (disclinations, dislocations, defects chain, and also more exotic defects like a rosette) and their occurrence has been analyzed for the different cell geometries. Only few dislocations, that do not degrade significantly the ordering, are observed in hexagonal and triangular cells due to the compatibility between the grain lattice symmetry and the cell shape symmetry. Moreover, no finite size effects are observed for these confinements. The other cell geometries (squared, hexagonal, heptagonal and circular) display more complex defects modifying the ordering of the system. Topologically charged defects affect consequently the ordering of the system and destroy orientational order as predicted by the KTHNY theory. Moreover, distortion in the system is observed if topologically charged defects are isolated in the bulk and the long-sized defects tend to divide the system in different domains.

6.5 Control of defects?

Frustrations from boundaries modify the state of the crystal but the number and the position of topological defects are not controlled. In this experiment, long range hexagonal order is impossible due to its incompatibility with confinement geometry forcing therefore topological defects. What about the reciprocal effect? How defects affect global order? To tackle this question, one has to control the number and the position of topological defects. In the next chapter, we introduce beads of different size in the assembly to induce pointlike frustrations leading to punctual defects, and we study their consequence on the order.

7 Binary mixtures

7.1 Introduction

As a geometric fact, the ground state of a 2D assembly of identical particles interacting through a central pair potential is the hexagonal lattice. However, as predicted first by Peierls [140] then proved by Mermin and Wagner [43], such a 2D system is unstable to thermal fluctuations as soon as the temperature becomes nonzero. The main consequence is the absence of conventional long range order, and the low temperature crystal has the following structure: only a quasi-long range translational order but more surprisingly, a long range orientational order [44]. By increasing the temperature, the crystal melts but follows a different scenario than in 3d. The most famous model to describe melting is the KTHNY theory [45, 46, 56, 57, 58] which predicts two distinct continuous transitions mediated by topological defects. After the first transition, dislocations are not paired anymore leading to the destruction of translational order and the dynamics becomes similar to a liquid, however, orientational order persists giving an anisotropic liquid called hexatic phase. Actually, a dislocation is made of a pair of opposite disclinations and the unbinding of these disclinations with the increase of temperature causes the loss of orientational order corresponding to the transition to a classical isotropic liquid (see Sec. 5.2). This subject has been extensively studied in the last 20 years and nowadays the ground-state and low-temperature structures are well known as well as how the order vanishes during melting whatever the nature of particles and the interaction [92].

In parallel, glassy materials are an intensive area of research. While glass has been used for centuries, their properties and the glass transition are still poorly understood. Luckily, general features of glass appear to be similar (i) whether in 2D than in 3D [141, 142, 143] and (ii) whatever the nature of the system. Thus, experimentally, 2D granular or colloidal materials quickly became a trendy tool for the study of glasses due to the easiness to access both dynamics and

structure by simple image analysis. To behave like a glass, a system needs geometric frustrations to prevent crystalization at low temperature. In many works, this frustration is induced by polydispersity, more particularly by bidispersity. All possible ground-states of binary systems for long and short-ranged interactions are well known since the work of Assoud *et. al.* [144, 145]. The resulting phase diagram show that the ground-state crystal structure strongly depends on the mixing ratio, called here stochiometry, and the interaction strength asymmetry between the different types of beads. At nonzero temperature, frustrations produce many degenerate low-energy states and the global order can quickly vanish but this is still poorly reported in the literature. Furthermore, the mechanism causing the loss of order with change in the stochiometry is elusive. Only few studies examine this issue but are focused on high interaction strength asymmetry between components [98, 118, 146]. The aim of the presented study is, among others, to explore the structure at low temperature in a new range of interaction asymmetry.

In this chapter, we are also at the crossroads of several current topics. Indeed, discussing loss of order in a material is necessarily linked to topology. First, topological defects and their proliferation can be at the origin of phase transitions (see Nobel prize 2016 [91]), KTHNY scenario is a typical example. Secondly, topological defects play a key role in properties of many materials, like mechanical resistance, photonic properties, electrical and thermal conductivity, etc. Defect engineering is actually an important challenge in materials science. The emergence of 2D materials with extraordinary characteristics, like graphene, is a motivation to deepen our understanding on the link between 2D lattice and defects. As an example, dislocations in graphene cause structural distortion stiffening suspended monolayers of graphene, moreover these distortion are also strongly coupled to electrical conductivity, see [70] for details review and more examples about graphene. Many techniques already exist to manipulate defects: topological tweezers [147, 148], substrate curvature [114], geometrical confinement [85] or introduction of heteroclite particles by their mobility [149], their size [118, 119] or the nature of the interaction [150].

We present here experimental results concerning the influence of bidispersity on the order of a 2D crystal made of millimetric beads with magnetic dipole-dipole interactions and submitted to an external agitation. In the first part, the global order of the system is studied by only changing the stochiometry. A model is proposed and discussed to catch the phenomenology. Two types of beads are used such that their size ratio induces a dipolar moment ratio equal to $1/2$ which correspond to an unexplored configuration for binary mixtures at nonzero temperature. In the second part, we investigate how the difference in size between beads induces geometrical frustration at local scale and how it is linked to specific topological defects, bearing out that bidispersity is an efficient method to control defects.

7.2 Experimental details

For the study of binary mixture of beads is laid horizontally at the surface of a flat frosted glass plate and confined in a 2D hexagonal cell with ferromagnetic walls. The beads are excited horizontally, using two perpendicular shakers, such as the beads acquire a 2D Brownian motion. Equilibrium-like state is reached following the same protocol as in Chapter 6. The total number of beads is fixed to $N = 919$ and the particle area density is $\rho = 365000$ beads/m^2. The binary mixture is composed two types of beads, A and B, with diameters $d_A = 1$mm and $d_B = 0.78$mm giving a volume ratio $\upsilon = 0.47$, also called the dipolar ratio because magnetic dipole moments depend linearly on the volume $m_{A/B} = V_{A/B}\chi H_0$. The mixture is characterized by the number fraction of B-type particles, namely the stochiometry

$$\xi = \frac{N_B}{N_A + N_B}. \tag{7.1}$$

Two 19 cm diameter coils in Helmholtz configuration produce an external and vertical magnetic field H_0, up to 12000 A/m, in which beads are immersed. Both types are made with AISI 52100 chrome steel with an effective susceptibilty $\chi = 3$. As a consequence, the repulsive potential between two beads separated by a distance r_{ij} depends on the nature of the pair, A-A, B-B or A-B

$$U_{ij} = \frac{\mu_0}{4\pi}\frac{V_i V_j \chi^2 H_0^2}{r_{ij}^3}. \tag{7.2}$$

It is shown in Sec 3.3 that the mean magnetic interaction energy between two beads can be written

$$\langle U \rangle = \frac{\mu_0}{4\pi}\chi^2 V_A^2 H_0^2 \left[\upsilon\xi + (1-\xi)\right]^2 \left(\frac{\sqrt{3}}{2}\rho\right)^{3/2}. \tag{7.3}$$

Here, the control parameter is the stochiometry ξ. In comparison with results in previous chapters, the density is significantly increased for purely technical reasons. Indeed, as the pair interaction depends on ξ, between pure systems $\xi = 0$ and $\xi = 1$, the mean interaction drops by a factor $\upsilon^2 \sim 0.22$. The external magnetic field is limitate, a high area density is thus chosen to guarantee a perfect hexagonal crystal state for both pure states.

A CCD camera records series of images after the cooling process at a typical rate of 15 frames per second during 20 seconds. Each measure is averaged over these last 300 images. The system is backlighted with a lattice of LEDs and a diffuser. Therefore, the neat contrast between the beads and the background allows an accurate discrimination of A and B-type beads in function of their apparent diameters. Due to out of horizontality, even very slight, a demixing

process can occur near boundaries at the beginning of the cooling protocol because under low magnetic field, interactions with small beads are weak enough to allow them to move almost freely in the magnetic energy landscape because of the gravity. To fix this issue, we define a region of interest at the center of the cell, where demixing does not significantly appear. Each presented measurement is done within this region of interest.

7.3 Results

7.3.1 Global scale

At first sight on Fig. 7.1, the increase of the binarity destroy global order. Notice that ranging from a stochiometry $\xi = 0$ to $\xi = 1$ actually corresponds to two distinct but symmetric ways to see the experiment:

- $\xi = 0 \rightarrow 1/2$: small B-beads are considered as impurities in an array of big A-beads (Fig. 7.1(left)).
- $\xi = 1 \rightarrow 1/2$: big A-beads are considered as impurities in an array of small B-beads (Fig. 7.1(right)).

Monodisperse assemblies, $\xi = 0$ and $\xi = 1$ display a well established hexagonal order as confirmed by the pair correlation function $g(r)$ (Fig. 7.2). See Chapter 5 for a definition of $g(r)$. When the concentration of impurity increases until equimolarity, translational order is destroyed at both short and long ranges. Indeed, the peaks of $g(r)$ become wider and smaller until merging together. Therefore, $g(r)$ becomes quickly flat at long distance. For $0.12 < \xi < 0.90$, $g(r)$ exhibits the typical structure of an amorphous solid or a liquid. In the monodisperse case, the first peak of $g(r)$ can be fitted by a Gaussian function centered in the spacing lattice a [151]. However, for a mixture, the first peak of $g(r)$ is distorted and not fully centered around $1r/a = 1$. This is due to the bidispersity. Indeed, three types of pairs are present in the system: $A-A$, $B-B$ and $A-B$ and they are characterized by a typical distance d_{AA}, d_{BB} and d_{AB} with

$$d_{BB} < d_{AB} < d_{AA}. \tag{7.4}$$

The first peak is thus a sum of three Gaussian functions centred in these typical distances. This observation will be discussed in more detail in Sec. 7.3.2.

To quantify the effect of the stochiometry on the macroscopic scale, the bond order parameter

$$\psi_{6,k} = \frac{1}{n} \sum_{j=1}^{n} e^{i6\theta_{kj}}, \tag{7.5}$$

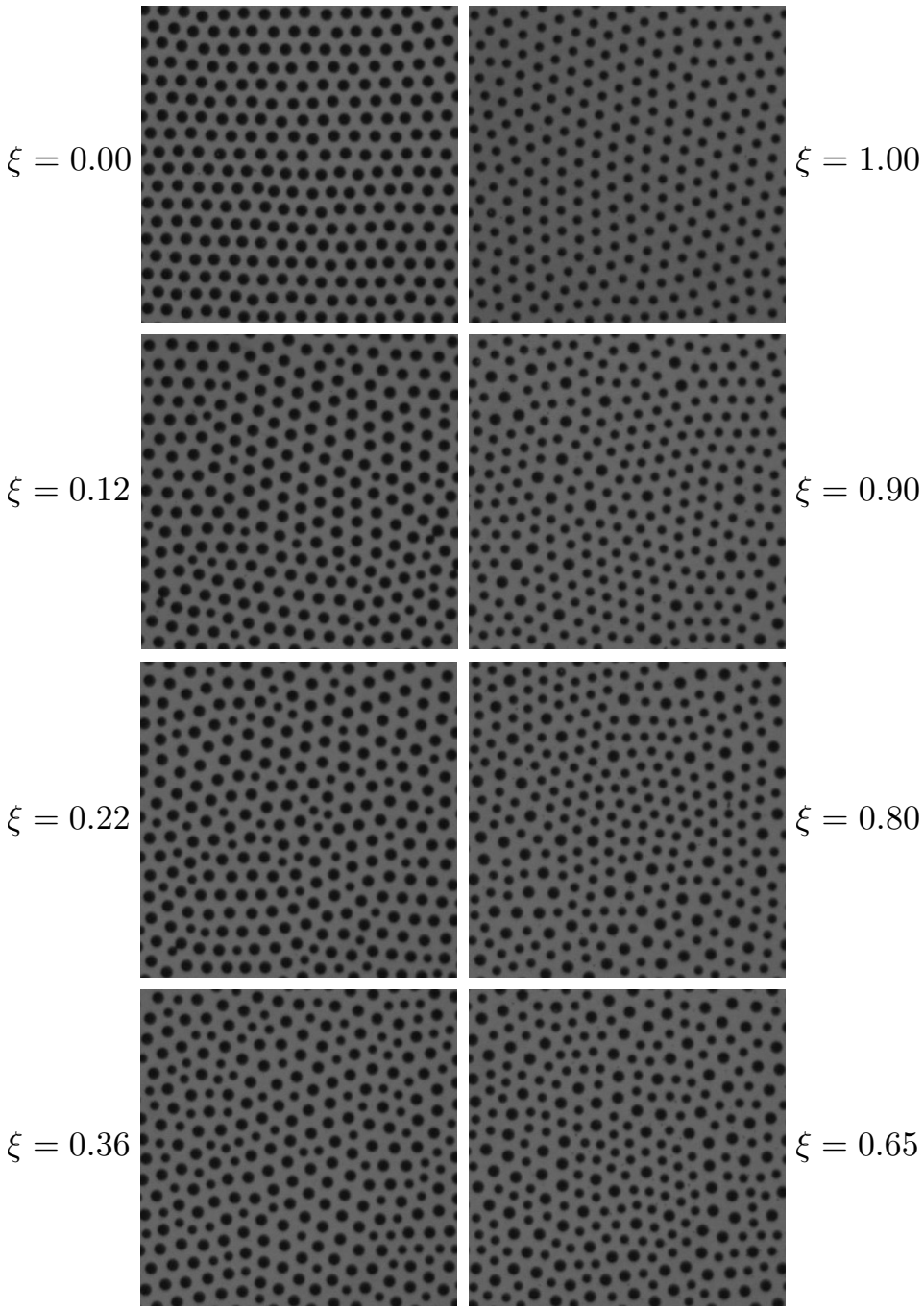

Figure 7.1 – Snapshots of the system for many stochiometries.
Left column: $\xi = 0 \to 1/2$. Righ column: $\xi = 1 \to 1/2$.

is computed for each particles k with n nearest neighbors. Remember that the modulus $\mid \psi_{6,k} \mid$ gives the degree of local six-fold symmetry, $\mid \psi_{6,k} \mid = 1$ for a perfect

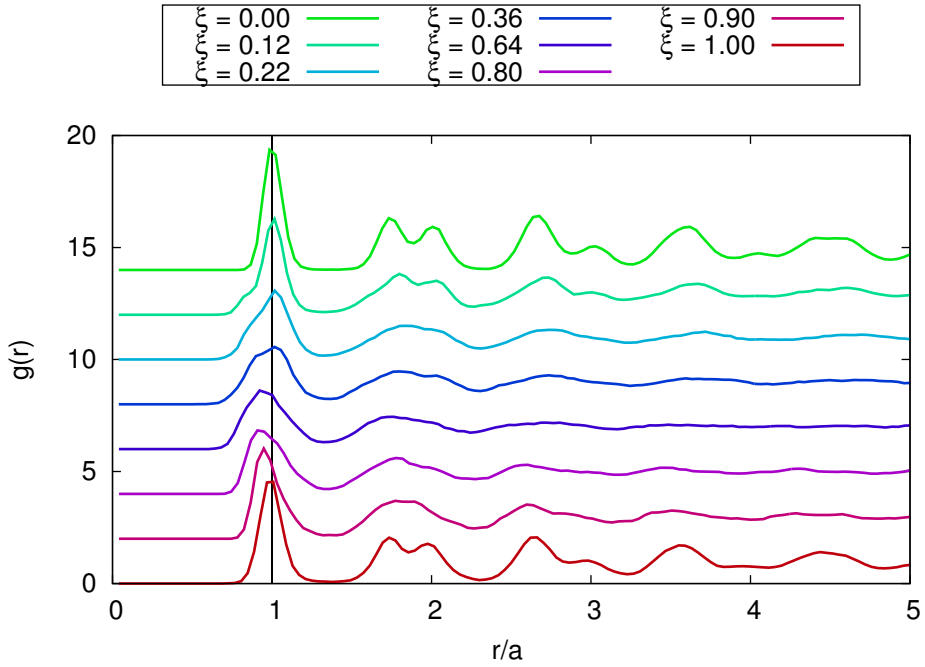

Figure 7.2 – Pair correlation function $g(r)$ for different stochiometries ξ. The function is calculated without distinction between A beads and B beads. Curves are shifted for readability. a is the lattice spacing for a hexagonal lattice.

hexagonal unit cell and tends to zero for a unit cell with a random symmetry. The global orientational order of the system is obtained by averaging the modulus of the bond order parameter over each particle in the region of interest

$$\psi_6 = \left\langle \left| \, \psi_{6,k} \, \right| \right\rangle . \tag{7.6}$$

Fig. 7.3 shows that the global order strongly depends on the stochiometry ξ. When the number of impurities increases ($\xi = 0 \to 1/2$ or $\xi = 1 \to 1/2$) the global order collapses and reaches a minimum value at equimolarity. Let us remark that the plot is not symmetric on both side of $\xi = 0.5$ due to the expression of the mean pair interaction in Eq. (7.3). Indeed, as the area density ρ is fixed, mean interaction in a system of big beads is higher than for a system of small beads, the maximum order reached is not identical.

To show that the loss of global order due to binarity is a phenomenon of a different nature than a classical melting, Fig. 7.4 makes the comparison between the ψ_6 distribution of binary mixture at $\xi = 0.35$ and the distribution of a classicaly melted monodisperse system presenting the same averaged bond order parameter. The monodisperse case presents a flat distribution indicating that local order is lost for each bead and almost uniformly distributed between 0.3 and 0.8. Whereas the binary case presents two distinct peaks which is a sign of ordered and disordered areas.

The top of Fig. 7.5 displays the distribution of ψ_6 in the system for many stochiometries, two distinct populations appears. There are beads with ordered environment with $\psi_6 \approx 0.9$ and beads with disordered environment with $\psi_6 \sim 0.3$. The size of the peaks of the distribution changes with the stochiometry. When the number of impurities increases, ordered peak reduces and disordered one grows up. Bottom of Fig. 7.5 shows that ordered environment is exclusively composed of beads with six-fold coordinate number ($n = 6$) but disordered environment is due to defects ($n = 5$ or $n = 7$) or distorted hexagonal neighborhood.

In Fig. 7.6, the system is represented with Voronoi tesselation colored in black for beads with a disordered environment ($\psi_{6,k} < 0.6$) and in white for ordered environment ($\psi_{6,k} > 0.6$). For the three stochiometries presented ($\xi = 0.11$, $\xi = 0.21$ and $\xi = 0.35$), we observe clusters of black Voronoi cells and clusters of white Voronoi cells. The arrangement of clusters closely look like pattern observed in Ising model with coupling interaction.

These observations motivate us to propose a simple and conceptual two states model, inspired of Ising model, to understand the global behaviour of the system by increasing the number of impurities. Instead of up and down spins, we assume that a bead is either in a hexagonal ordered (O) environment or in a disordered (D) environment. At temperature T, the probability for a bead to be in an ordered ground state is

$$P_O = \frac{1}{Z} \exp\left(\frac{-E_O}{k_B T}\right), \tag{7.7}$$

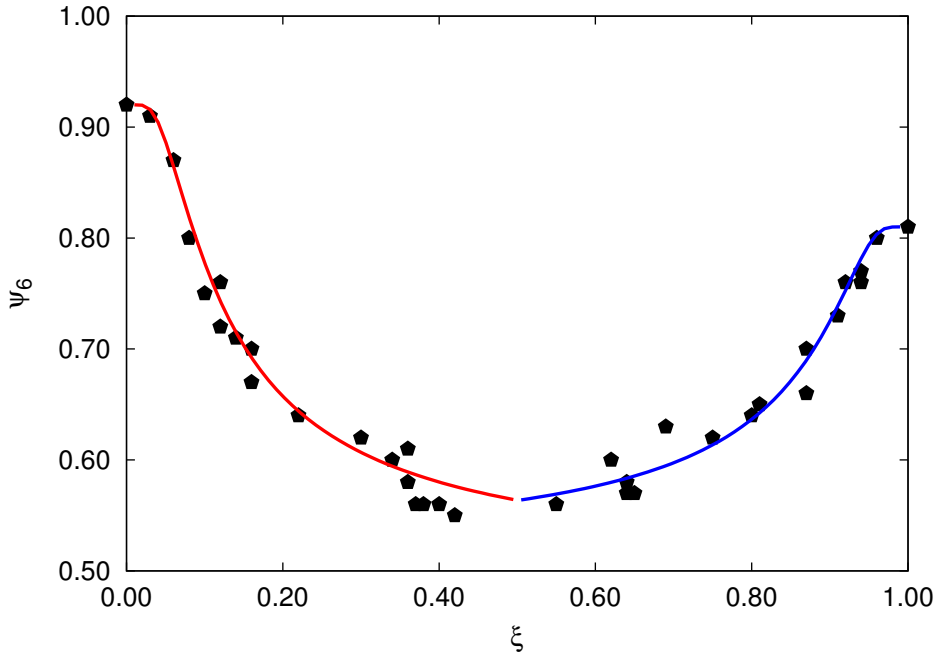

Figure 7.3 – Mean bond order parameter ψ_6 in the system as a function of the stochiometry ξ. Solid lines correspond to Eq. (7.13), the red curve corresponds to $\psi_6(\xi)$ from $\xi = 0$ to 0.5 and the blue corresponds to $\psi_6(1-\xi)$ from $\xi = 1$ to 0.5.

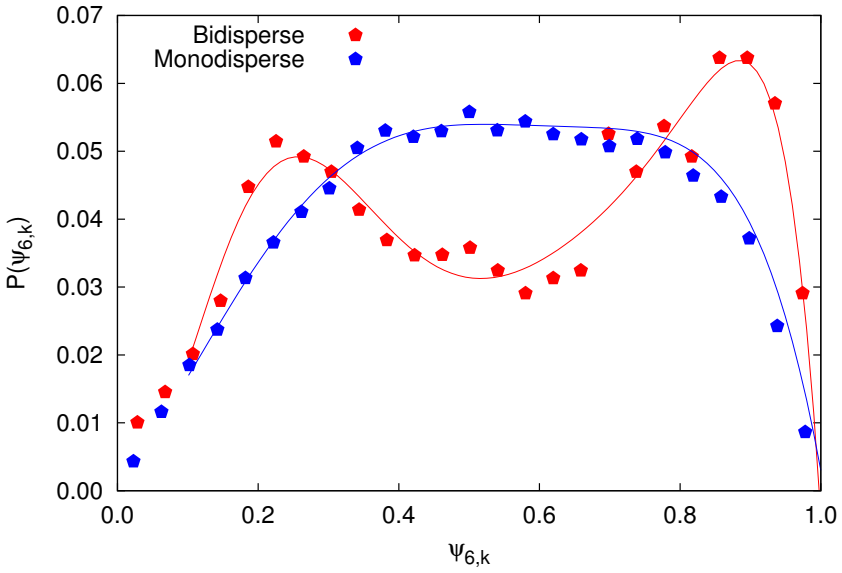

Figure 7.4 – Distribution of bond order parameter for a binary mixture ($\xi = 0.35$) in red and for a melted monodisperse system ($\Gamma = 10$) in blue. The mean value of the bond order parameter is identical for both systems: $\psi_6 = 0.6$.

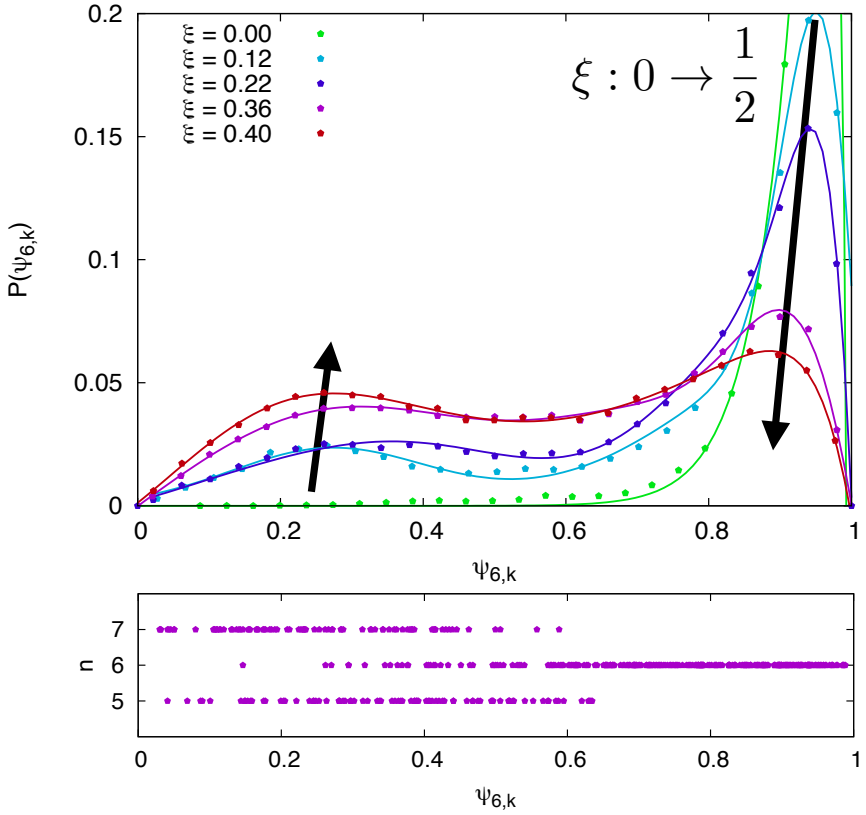

Figure 7.5 – (Top) ψ_6 distribution measured for several stochiometries ξ between 0 and 1/2. Lines are arbitrary fit to guide eyes. (Bottom) Coordinate number n of a bead as a function of its bond orientational parameter $\psi_{6,k}$.

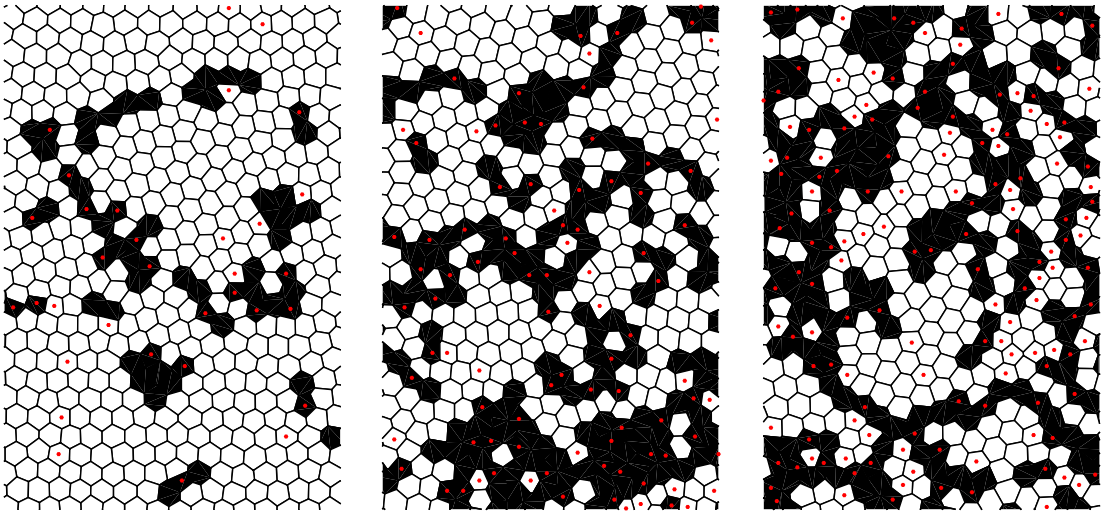

Figure 7.6 – Voronoi tesselation with black cells for beads with a disordered environment ($\psi_{6,k} < 0.6$) and white cells with an ordered environment ($\psi_{6,k} > 0.6$). From left to right, $\xi = 0.11$, $\xi = 0.21$ and $\xi = 0.35$. Red dots correspond to the location of impurities.

and in the disordered excited state

$$P_D = \frac{1}{Z} \exp\left(\frac{-E_D}{k_B T}\right), \tag{7.8}$$

where E_O and E_D are respectively energies associated with beads in ordered and disordered environment and Z is the partition function

$$Z = \exp\left(\frac{-E_O}{k_B T}\right) + \exp\left(\frac{-E_D}{k_B T}\right). \tag{7.9}$$

The mean value of the bond order parameter can thus be estimated

$$\psi_6 = \frac{\psi_{6,O} P_0 + \psi_{6,D} P_D}{Z}. \tag{7.10}$$

Combining Eqs (7.7), (7.8), (7.9) and (7.10) gives

$$\psi_6(T) = \psi_{6,O} + \frac{\psi_{6,O} - \psi_{6,D}}{2}\left[\tanh\left(\frac{\Delta E}{2k_B T}\right) - 1\right] \tag{7.11}$$

with $\Delta E = E_D - E_0$. The control parameter causing the loss of order is the temperature T. In our experiment, the control parameter is the stochiometry ξ which also causes the loss of order, we assume thus an equivalence between T and ξ and we propose the transformation

$$\frac{\Delta E}{2k_B T} \longleftrightarrow \frac{\xi_c}{\xi}, \tag{7.12}$$

giving

$$\psi_6(\xi) = \psi_{6,O} + \frac{\psi_{6,O} - \psi_{6,D}}{2}\left[\tanh\left(\frac{\xi_c}{\xi}\right) - 1\right], \tag{7.13}$$

where ξ_c is a characteristic stochiometry behind which the order declines quickly. As shown is Fig. 7.5, this hyperbolic tangent function fit closely the evolution of the mean bond order parameter ψ_6 as a function of the stochiometry ξ. In addition, the characteristic stochiometry can be estimated to $\xi_c = 0.08$ and agrees with the previous discussion about $g(r)$. The value of ξ_c is found to be nearly identical for red and blue curves of Fig. 7.3. Parameter $\psi_{6,O}$ is obtained from pure system then the fit is performed for $\xi = 0 \to 1/2$ (red curve) and $\xi = 1 \to 1/2$ (blue curve) letting ξ_c and $\psi_{6,D}$ free but the bond order parameter is forced to be identical at equimolarity whether it comes from $\xi = 0$ or $\xi = 1$. Note that $\psi_{6,D}$ could be measured but the uncertainties are significant due to fluctuation of ψ_6 in disordered environment. The quantitative agreement between data and the model means that increasing the number of impurities plays the role of increasing the temperature. To scale the stochiometry ξ with temperature T, we do not consider the temperature as a kinetic temperature, *i. e.* $k_B T = 1/2m^2$, but rather according to the thermodynamic definition:

$$\frac{1}{T} = \left(\frac{\partial S}{\partial U}\right)_{N,V}, \tag{7.14}$$

which is the variation of the entropy due to a change of the internal energy at constant volume V and total number of particle N. Adding impurities increases the number of possible configurations, we thus consider a mixture entropy

$$S = -Nk_B\left[\ln(1-\xi) - \xi\ln\left(\frac{1-\xi}{\xi}\right)\right], \tag{7.15}$$

where N is the total number of particles. The internal energy is estimated by summing the mean pair interaction from Eq. (7.3) over each pair of nearest neighbors

$$U = N_p u_0 \left[\upsilon\xi + (1-\xi)\right]^2, \tag{7.16}$$

where u_0 is the mean pair interaction in the monodisperse case $\xi = 0$ and N_p is the number of pair in the system which is $N_p = 3N$ in a hexagonal lattice. Then, using the relation

$$T = \frac{\partial U}{\partial \xi}\frac{\partial \xi}{\partial S} \tag{7.17}$$

we find

$$k_B T = \frac{6u_0(\upsilon - 1)\left[\upsilon\xi + (1-\xi)\right]}{\ln\left(\frac{1-\xi}{\xi}\right)}. \tag{7.18}$$

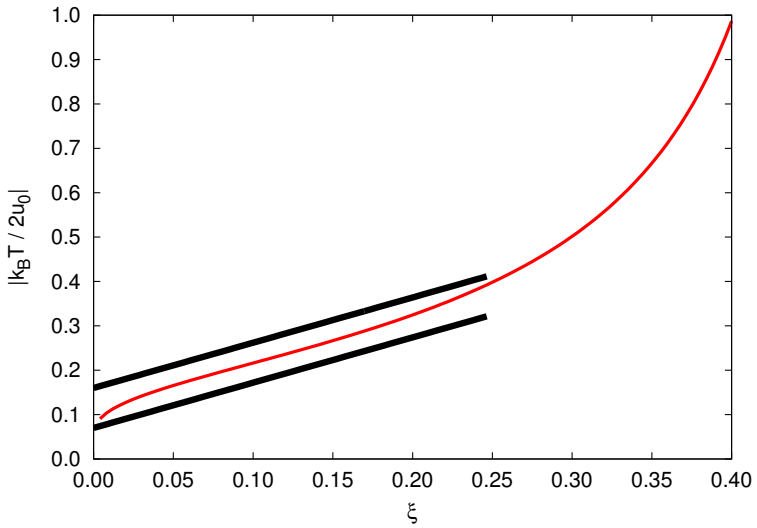

Figure 7.7 – Plot of Eq. (7.18) for a dipolar ratio $\upsilon = 0.5$. Quasi-linear regime is indicated from $\xi = 0 \rightarrow 0.25$.

The transformation from Eq. (7.11) to Eq. (7.13) is assumed to be a linear relation between temperature and stochiometry. Fig. 7.7 shows that this assumption can be considered correct far from equimolarity, giving the scaling

$$| \, k_B T \, | \sim 6 u_0 \xi. \tag{7.19}$$

The use of a thermodynamical definition of the temperature can appear to be inappropriate as energy is constantly injected in the system by the mechanical agitation. However, the good agreement between our granular experimental system and thermal systems indicates that this approximation is suitable. Actually, the system is said to be in a non-equilibrium steady state [36, 34], meaning that the rate of injected energy is equal to the rate of dissipated energy.

Now a linear relation between ξ and T is established so according to the transformation proposed in Eq. (7.12), there should be a linear relation between ΔE and ξ_c. In an Ising model under external magnetic field, the difference in energy between the two states corresponds to the cost in energy needed to flip a spin from parallel to anti-parallel. This energy is independent from the repartition of the up and down populations. By analogy, we state that the difference of energy ΔE between ordered and disordered states does not depend on the stochiometry ξ. In our model, the positions of particles in ordered state are forced as a hexagonal lattice, ΔE corresponds here to the cost in energy to introduce a singularity in the displacement field of the lattice which generates disorder in the environment of a particle. An estimation of this energy could be tried using tools from elasticity theory: extra elastic energy is stored in the bonds deformed by the disorder (see

Sec. 7.3.2). Combining Eqs. (7.12), (7.19) and the best fit parameter $\xi_c = 0.08$ gives the order of magnitude $\Delta E \sim u_0$ suggesting that the difference between an ordered and a disordered environment correspond to the energy to add or remove one bond. From $\xi = 0 \rightarrow 1/2$ the internal energy decreases because big beads are replaced by small beads which carry less magnetic energy, but the number of configuration increases and so the entropy. This fact means that the defined temperature Eq. (7.14) is negative which is a typical observation in two states systems with an inversion of population. Consequently, ΔE must be also negative to fit data suggesting that it corresponds to an energy to remove a bond to a hexagonal unit cell. This corresponds to the introduction of a five-fold disclination. From $\xi = 1 \rightarrow 1/2$, temperature is positive thus also ΔE, suggesting that it corresponds to an energy to add a bond corresponding to a seven-fold disclination. The toy model presented here must be tested for more mixture with different dipolar ratio υ because this parameter is expected to play a significant role in the loss of order even if we can not highlight it in the presented experiment. At the limit of the model, we expect that for a dipolar ratio $\upsilon \sim 1$, particles becomes indistinguishable and thus the order is not impacted. Contrarily, for $\upsilon <<$ we expect a quicker decay of order.

Although the model assumptions seem to be far more restrictive than reality, the quantitative agreement between the experiment and a two-level model teaches us that the loss of order is due to the increase of the configurational entropy with the binarity. In the monodisperse case, only one stable configuration is accessible, the hexagonal order, but due to binarity the number of accessible configurations, at a given temperature, increases and the hexagonal order becomes less probable. From this model, one can also extract a characteristic stochiometry ξ_c behind which it appears to be impossible to crystallize in a hexagonal lattice. Yet, no clear transition is observed and the parameter ξ_c only represents an indicative order of magnitude. While the model is suitable for macroscopic properties of our system, light must still be shed on the behavior of the system a local scale.

7.3.2 Local scale

Introducing a bead of different size into a monodisperse assembly creates very locally geometric frustration. It appears that this is a very effective way to generate topological defects with some control over its nature. Indeed, in the 2D monodisperse case at low temperature, the natural lattice is hexagonal but when an impurity is introduced, its coordinate number is observed to be different from 6. A larger bead tends to be surrounded by 7 neighbors, and a smaller bead tends to be surrounded by 5. These are considered as topological defects, namely disclinations. Fig. 7.8 supports this observation. In function of the stochiometry ξ, Fig. 7.8 (top) shows the conditional probabilities that a five-fold defect is carried

by a big A-type bead $p_5(A)$ or a small B-type bead $p_5(B)$. Likewise Fig. 7.8 (bottom) shows the probabilities that a seven-fold defect is carried by a big A bead $p_7(A)$ or a small B bead $p_7(B)$. We observe that five-fold defects are mostly carried by small beads while seven-fold defects are mostly carried by big beads. From $\xi = 0 \rightarrow 1/2$, a cross reading of both Fig. 7.8 top and bottom indicates that if a small bead generates a defect, it is necessarily a five-fold defect because $P_5(B) \neq 0$ and $P_7(B) = 0$. Similarly, from $\xi = 1/2 \rightarrow 1$, if a big A bead generates a defect, it is necessarily a seven-fold defect because $P_7(A) \neq 1/2$ and $P_5(A) = 0$. A defect caused by introduction of a different sized bead is called extrinsic point defect while a defect caused by the majority is called intrinsic point defect.

To understand this result, mean bond lengths of possible pairs d_{AA}, d_{BB} and d_{AB} are measured. Pairs are determined using a Delaunay triangulation. We find $d_{AA}/d_{AB} = 1.14$ and $d_{BB}/d_{AB} = 0.89$. Identical values are obtained by the method of the fit of $g(r)$ by a triple Gaussian function. As illustrated in Fig. 7.9, with these three typical lengths, one can construct four fundamental triangles: AAA, BBB, ABB, BAA. In the case of a homogeneous triangle, each vertex of the triangle forms an angle of 60° which is perfectly compatible with a hexagonal lattice. However, heterogeneous triangles are not compatible with a hexagonal lattice, leading to frustrations. Indeed, for AAB triangle, the B-bead sustains, an angle of 70°, indicating a mean coordinate number $n_B = 5.1$. And for BBA triangle, the A-bead sustains an angle of 53°, indicating a mean coordinate number $n_A = 6.7$. Big A beads are thus surrounded by 6 or 7 neighbors while small B beads are surrounded by 5 or 6 neighbours, which is indeed observed in Fig.7.8. The very good agreement between observations and this simple geometric argument thus suggest a strong link between topological defects and local density inhomogeneities. It also demonstrates how easy it is to produce topological defects by the use of polydispersity. To create disclinations with coordinate number greater than 7, we just need to increase the strength of AA pair interaction compared to AB pair, by changing the dipolar moment ratio. For a low dipolar moment ratio ($\upsilon < 0.1$), Bonales *et. al.* [118] observe, disclination with up to 10 neighbors.

To study the influence of an impurity on the lattice, we introduce a single small B-bead in a set of large A-beads, and two scenarios are observed. Either for 20% of cases, the small bead has 6 neighbors and does not disturb the hexagonal order. The surrounding lattice is locally stable enough to ignore the frustration, like an arch in a silo[5]. Either the bead has five neighbors and disrupts the order. It is known from the global scale study that a single impurity does not affect the global order, so how does the lattice recovers from a local frustration? The bond order parameter ψ_6 of a particle is suitable to quantify the deformation of its environment with respect to a hexagonal order. Fig. 7.10(top) shows the mean value of ψ_6 in function of the distance from the local frustration. Error bars correspond to the standard deviation over four independent experiments. The

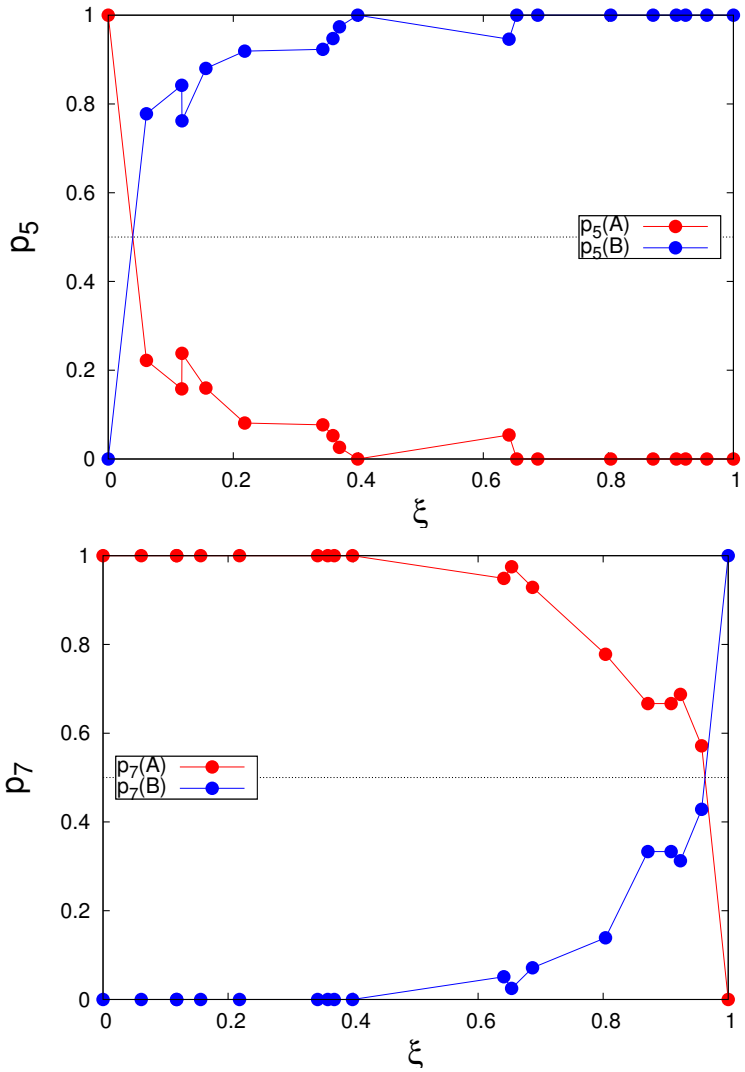

Figure 7.8 – (Top) Probabilities $p_5(A)$ and $p_5(B)$ that a five-fold defect is carried by a big A bead in red or a small B bead in blue. (Bottom) The probabilities $p_7(A)$ and $p_7(B)$ that a seven-fold defect is carried by a big A bead or a small B bead.

left insert is an example of a typical observed deformation field, blue and red bonds are respectively compressed and extended bonds in regards to the ideal bond length. Color intensity is proportional to elastic energy stocked in the bond calculated as a Hook's law $E_{el} \sim (\Delta l/l_0)^2$ which is a good approximation for small deformations. The drawn hexagon corresponds to the smallest closed contour (with a Burger's vector equal to zero) enclosing the impurity. The right insert is the Voronoi tesselation of the same situation, defects are represented using red

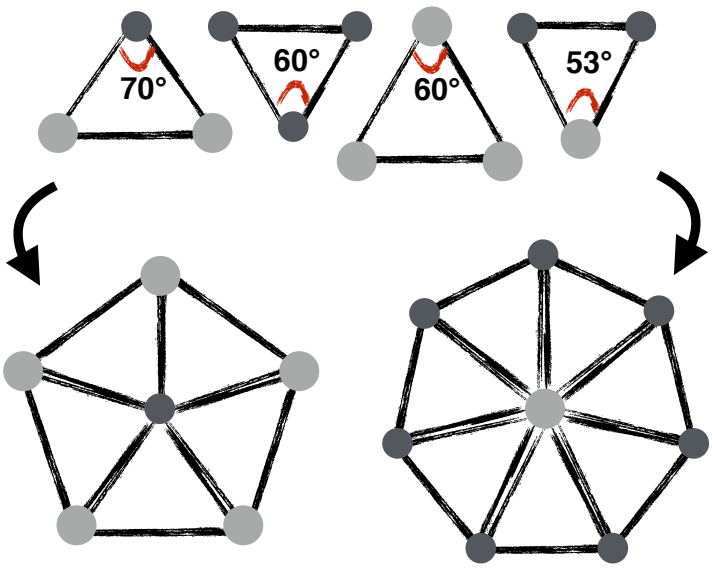

Figure 7.9 – The four fundamental triangles AAA, BBB, ABB, BAA constructed from measured average distance d_{AA}, d_{BB} and d_{AB} and resulting pentagonal (resp. heptagonal) pattern for B (resp. A) beads surrounded by A (resp. B) beads. The large dark grey circle corresponds to A-beads and the small light grey corresponds to B-beads.

and green cells respectively corresponding to a particle with five-fold and seven-fold coordinate number. Additional information about the deformation field is given by representing six-fold cells on a gray scale from black ($\mid \psi_{6,k} \mid = 0$) to white ($\mid \psi_{6,k} \mid = 1$). The impurity is a defect due to geometrical reasons discussed above but near the impurity, the hexagonal lattice undergoes a series of elastic deformations, favoring the appearance of additional topological defects. However, the strain field is spatially limited, and the hexagonal order is quickly restored, meaning that the system prefers to pay locally a penalty in elastic energy rather than rearranging at global scale. This behaviour is supported by the evolution of ψ_6 which increases from the impurity to reach quickly the global mean value of ψ_6. An isolated different size bead, therefore, has only a local impact on the lattice. From a topological point of view, the defect due to the impurity forces regular beads to become a defect such that the total topological charge and the sum of Burger's vectors vanish to preserve long range order. Only three kinds of defects are observed, the most common defect is in the insert of Fig. 7.10(top), where two dislocations of opposite direction, and therefore of opposite Burger's vector, are close. Fig. 7.10(bottom) shows the two other kinds of defects which are also observed. On left, a 4-fold defect (topological charge +2) flanked by two seven-fold defects (topological charge −1), this defect is topologically neutral and

equivalent to a pair of opposite dislocations except that the two five-fold defects merged to give a 4-fold defect. On the right, the defect is composed of three dislocations around the impurity whose sum of the Burger's vectors is zero.

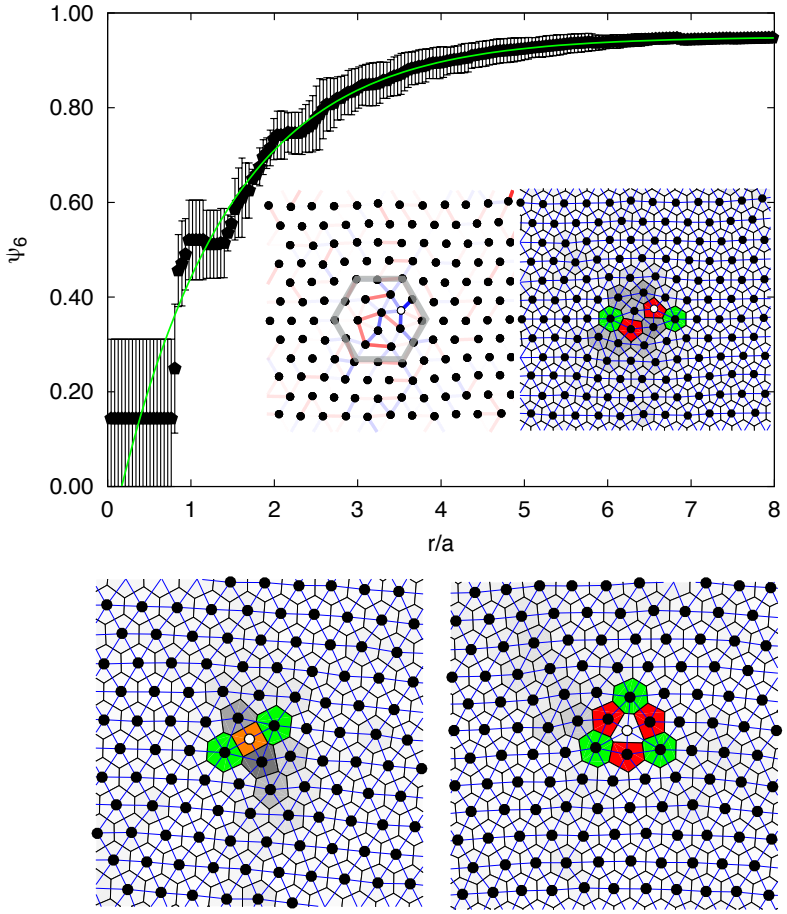

Figure 7.10 – (Top) Mean bond order parameter ψ_6 of particles in function of the distance from an isolated impurity. Dots and errorbars respectively correspond to the average and the standard deviation over several experiments, green curve in an arbitrary fit for eye guide. (Insert-left) Illustration of the elastic deformation of bonds near an impurity, blue for compression and red for extension. The color intensity is proportional to elastic energy. The grey hexagon is the smallest closed contour that encloses the impurity. (Insert-right) Voronoi tesselation near an impurity. Six-fold cells are represented on a gray scale proportional to $\mid \psi_{6,k} \mid$ and white dot is the impurity. The two inserts are two different graphic interpretations of the same situation. (Bottom) Other typical defects encountered near an impurity.

The discussion above holds for isolated impurities. To remain isolated, the area of deformation of two impurities must not overlap. At a given stochiometry,

the average distance between two small B-beads is $(\xi\rho)^{-1/2}$ which must be smaller than the size of the area of deformation, approximate to be circular

$$2R_D < (\xi\rho)^{-1/2}. \tag{7.20}$$

Fig. 7.10(top) displays a continuous evolution of ψ_6 from impurity to bulk meaning that the radius R_D of the area of deformation cannot be clearly identified, but it is observed that the typical smallest hexagonal closed contour around the impurity has a side of 2 times the typical distance $1/\sqrt{\rho}$, we thus take $R_D = 2/\sqrt{\rho}$. Using this value in Eq. (7.20) gives a limit stochiometry $\xi_L = 0.06$ beyond which impurities are not considered as isolated. Note that ξ_L is close to the fit parameter ξ_c from Eq. (7.13), suggesting that the overlap of the areas of deformation triggers the loss of order at global scale.

When areas of deformation overlap, topological defects become more complex. Just above ξ_L, the spatial extension of defects around an impurity is not isotropic but oriented as well as to connect two impurities by a straight sequence of dislocations forming a grain boundary. We thus observe macroscopic grain boundaries, each articulated around two or more impurities. These grain boundaries encapsulate domains of ordere crystallites. Consequently, for $\xi > \xi_L$, the system is considered as a polycrystal. Beyond an angular threshold between the orientations of the domain and the bulk, the formation of a clear grain boundary becomes energetically more favorable than accumulating shear energy in the vincinity of the domain [148]. Domains are illustrated in Fig. 7.11(top) for $\xi = 0.07$. On the left, the Voronoi tesselation let clearly appear the grain boundary and the presence of impurities within it. On the right, beads are colored in function of the projection of the complex number $\psi_{6,k}$ along an arbitrary direction from 1 (red) to -1 (blue) which gives information about the local orientation of the system. Domains are well displayed, red and blue corresponds to well-ordered domains but with different orientations. Green and yellow correspond to beads with random orientation or low degree of order and actually mark the fronteers between domains. As shown in Fig. 7.11(bottom), when the density of impurities increases, and consequently the density of defects, we observe an increase of the number of domains, a decrease of their size and frontiers between them becoming more blurred. Indeed, as the defect points increase, the number of grain boundaries increases which isolates more domains, but their length decreases encapsulating smaller domains. The frontiers become more blurred because the grain boundaries becomes broader or more folded, therefore the grain boundaries become less clear and are more and more transformed in a cluster of defects.

Instead of these observations, the domains never totally vanish meaning that in the whole range of ξ, the system remains a polycrystal, a strictly liquidlike structure is thus never observed.

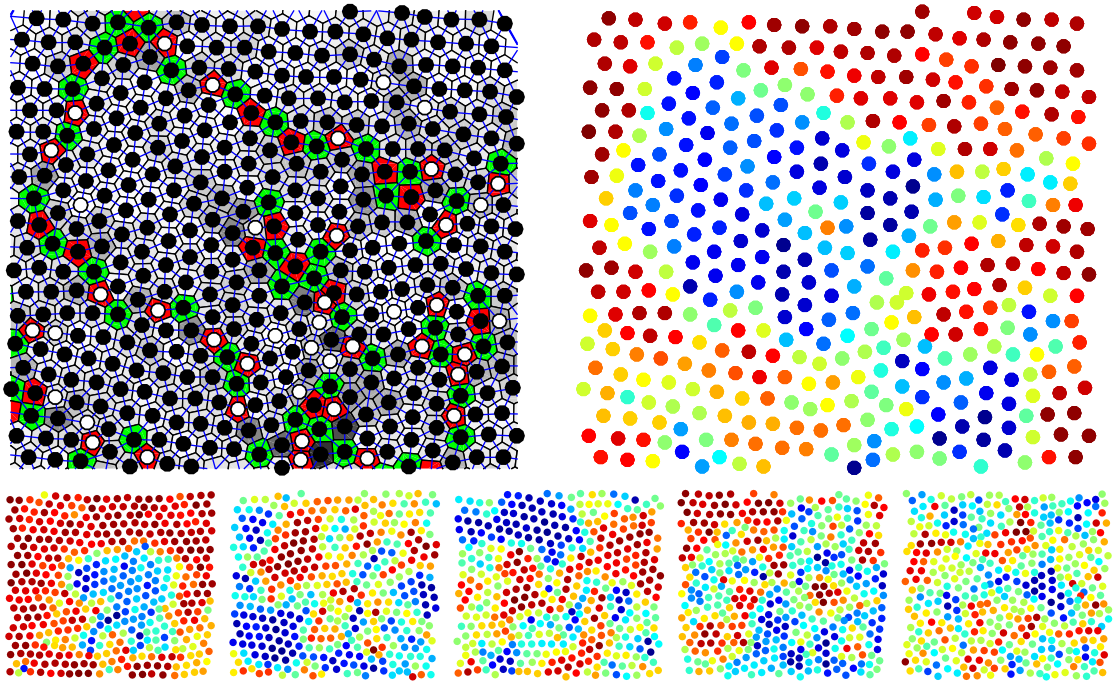

Figure 7.11 – (Top-left) Voronoi tesselation with same colorcode as Fig. 7.10 for $\xi = 0.07$. (Top-right) Projection of $\psi_{6,k}$ along an arbitrary direction, running from 1 (red) to -1 (blue) to illustrate the local orientation of the system at $\xi = 0.07$. Bottom: $Re(\psi_{6,k})$ for $\xi = 14$, $\xi = 20$, $\xi = 30$ and $\xi = 40$.

7.4 Conclusion

We have explored the structure of a 2D binary system by only changing the proportion of big and small beads. The study of the pair correlation function $g(r)$ shows that the structure becomes liquidlike by increasing the rate of impurities and simultaneously, the first peak is distorted. This observation points out that adding impurities in a pure system affects global order through the action of local frustrations. However, the system is not uniformly disordered like a liquid, indicating the loss of order follows a different mechanism that melting. The observations at global scale agree qualitatively with a two-levels model where the rate of impurities plays the role of the temperature by changing the configurational entropy.

Studying the role of impurities at local scale reveals that they force topological defects whose type depends on the size of the impurity. Small beads are mainly five-fold defects while big beads are rather seven-fold defects. Moreover, it seems that this coordinate number can be tuned by changing the relative pair interaction between small and big beads. Being able to create and control the nature of a single defect allowed us to study its influence on the lattice. It is found that, in the immediate vicinity of the introduced impurity, additional defects are created due to elastic deformation of the lattice aimed at restoring order over few interparticle distances. As the number of impurities increases, deformation areas overlap and defects assemble in more complex structure, like grain boundaries, to isolate ordered domains of increasing numbers and smallness.

8 Conclusion and perspectives

Conclusion

The challenge of this thesis is to develop an original and macroscopic experiment to study the state of 2D matter. Actually, 2D materials are not abundant in nature and thus poorly known but yet worthy of interest given the recent technological progress and the universality features for a large number of quasi-2D physical systems. In particular, the melting scenario is far different from its 3D counterpart and topological defects play a crucial role in 2D systems. These subjets are precisely the focus of the presented work.

Basically, state of matter is dictated by the competition between ordering and disordering effects, respectively due to interactions and thermal agitation. Inspired from this fact, our experimental model system is designed such that particles are submitted to two controlled contradictory effects. On one hand, the horizontal monolayer of beads is immersed in a vertical magnetic field inducing magnetic dipole-dipole interactions. Due to the confinement, produced by the repulsive wall of the cell, the interactions tend to order the system. As shown in **Chapter 3**, the magnetic field produced by a uniformly magnetized sphere is perfectly equivalent to a punctual dipole meaning that the bead-bead interaction is well defined. Despite we did not find an analytic relation of the bead-wall interaction, it has been well modelized and the repulsive wall guarantees a homogeneous density within the cell. On the other hand, the beads are submitted to a mechanical agitation which produces an erratic motion of the beads and thus creates disorder. **Chapter 4** is dedicated to the study of this agitation, it is shown that the motion of the beads is uniform and agrees with the Langevin description of brownian motion: ballistic motion at short time scale and diffusive motion or caging at long time scale for respectively free particle and non-free particles. As the dipole-dipole interaction cancels the inelastic collisions between beads, the probability distribution function of the velocity follows closely a Maxwell-Boltzmann distribution.

This thermal-like behaviour allows us to use the equivalence between mean kinetic energy and temperature and therefore we can confront directly our results to thermal systems.

By adjusting the ratio between pair interaction and kinetic energy, *i.e.* the coupling parameter, we are able to control the order of the system. In **Chapter 5**, we have shown that the observed transition from crystal to liquid agrees with the well admitted 2D melting scenario: the KTHNY theory. The signature of each predicted phases (crystal-hexatic-liquid) has been highlighted with the use of both static and dynamic order parameters. In addition, for identical coupling parameters, structures obtained match quantitatively with structures obtained in colloidal systems and numerical simulations. We therefore conclude that our experiment can be considered as a suitable model system to study the state of 2D matter. From there, we focused on the study of topological defects: their influence on the order and the way of generating them.

The confinement is essential to our experience, otherwise the beads would not be ordered. So we have studied the influence of the geometry of the confinement on the system at low temperature, where the system is supposed to be a crystal without external frustrations. It has been shown in **Chapter 6** that the cell geometry strongly affects the ordering of the system. Global order, given by the bond order parameter ψ_6, is higher for triangular and hexagonal cells compared to squared, pentagonal, heptagonal and circular shaped cells. The symmetry of these last is not compatible with the crystal symmetry inducing frustrations which result in the appearance of topological defects. Moreover, many kinds of defects, whose observation rate is linked to the geometry, have been observed: disclinations, dislocations, defects chain, and also more exotic defects such as a rosette. Finally, the influence of confinement size has been investigated, and we point out that no finite-size effect occurs for a hexagonal cell, but the finite-size effect changes from one geometry to another. In short, an inadequate confinement prevents the hexagonal order from being established everywhere, leading to the appearance of topological defects.

In **Chapter 7**, the opposite question is tackled: how topological defects affect crystal order. It is shown that topological defects can be artificially created by introducing beads of different size. Adding a small (resp. big) bead in an array of big (resp. small) beads corresponds to add an impurity in the system. This creates a very localized frustration inducing topological defect that affects the order in its vicinity. In particular we have studied the order of the low temperature state as a function of the impurity concentration. Using global order parameter, we have shown that increasing the number of impurities and thus the number of defects reduces the order until reaching liquidlike structure near equimolarity. We have also pointed out that, unlike melting, the loss of order due to impurities is not homogeneous but present domains of ordered or disordered crystallites. We

have thus proposed a two-levels model where beads are whether in an ordered or a disordered environment and where the concentration of impurities act as a temperature. A quantitative agreement between the model and the observations has been found. We have studied the local influence of an impurity on the order. It has been shown that the type of defect generated by the impurity is strongly related to its size: a big bead tends to be a seven-fold defect and a small bead rather a five-fold defect. It also appears that one can tune the coordinate number of a bead by only changing its size which is actually defect engineering. Finally, it is observed that the global order of a crystal is not affected by isolated impurities but due to an association of impurities which generate complex defects like grain boundaries.

Perspectives

The potential of this experimental model system is still not yet fully exploited. In this section, we propose a non-exhaustive list of technical enhancements and possible further works.

- Adjusting the horizontality is a delicate part of the experiment because the beads are very sensitive to the slope, even for a very slight one and unfortunately, the beads are more sensitive than any used inclinometers. Consequently, a significant drift of the system is observed for long acquisition times. Moreover, this drift is faster if the interaction between the balls is weak making the study of the liquid phase more tricky. To fix that problem, a solution would be to track the position of each bead in real time to know the instantaneous position of the center of mass of the assembly. The horizontality can thus be adjusted until the center of mass stop drifting.

- Once manufactured, the surface of the confinement cell can not be changed. The system is therefore intended for the study of isochoric processes. A new cell has been designed (Fig. 8.1(a)) to modify continuously the confinement surface during acquisition. This cell is a mechanical iris where the blades do not overlap, which does not change the thickness of the cell. The advantage of such a device is that the crystal can be compressed or dilated parallelly to its principal axes of symmetry, contrarily to a basic piston. This adjustable cell has not been used experimentally yet.

- The KTHNY theory is supposed to be applied to infinite systems. We have observed this melting scenario (**Chapter 5**), however, because it has been found that there is no finite size effect for hexagonal confinement (**Chapter 6**). Thus, the following question can be asked: what is the melting scenario for a crystal under frustrated confinement and can we find the hexatic phase?

- The model for binary mixture proposed in **Chapter 7** matches well our data. However, it has only been tested for one very specific dipole ratio, imposed by the choice of beads. Today, too few related studies exist and we still do not know if the proposed model has a universal character. Intuitively, it is expected that the closer the types of beads are, the less the global order is affected by the mixture as illustrated in Fig. 8.1(b) but it remains not clear how to include it in the model. Unfortunately, the sizes of beads available on the market are limited, an exhaustive study of the influence of dipole ratio seems thus difficult experimentally. Numerical simulations appear thus to be a suitable tool to improve our model and consequently acquire a better knowledge about mechanisms that destroy order in binary mixture.

- Binary mixture are effective to prevent crystalization at low temperature, being thus a relevant tool to study glasses. In our study, we only focused on static parameters to study the order. Nonetheless, our experiment is a priori suitable to study the dynamics and help to understand the glassy behavior which remains an elusive domain. Indeed, if we improve the adjustment of the horizontality as mention above, one could record the dynamics over a long period and study the dynamical heterogeneities related to the glass transition.

- Binary mixture combines with the adjustable cell could allow us to study the mechanical response of a glass under compression.

- The ground state of a monolayer of the isotropic repulsive particles immersed in a uniform gravitational field is called a *gravity rainbow* [152]. More generally, each lattice undergoing a distortion due to an external field is called a conformal crystal and are consequently inhomogeneous. At finite temperature, these spatial inhomogeneities induce the appearance of new topological defects (comparable to those caused by a curved surface [153]) and also inhomogeneous dynamics where the system can exhibit solid dynamics in denser regions and liquid dynamics in less dense regions. To our knowledge, the behaviour of conformal crystals at finite temperature is still poorly studied, and our experimental set-up appears to be a good candidate for this study. Indeed, a tilted confinement cell allows us to produce a controlled density profile. Fig. 8.1(c) is a snapshot which comes from a preliminary work.

- Our experiment is suitable to study the relaxation of the system after an ultrafast quenching. Indeed, switching off the agitation corresponds to an instantaneous jump to a zero temperature.

- Our experiment allows us to study the structure of the system where pair interaction is anisotropic. Anisotropic interactions can be induced by tilting the external magnetic field in regards to the vertical [154]. This new geometrical configuration is summed up in Fig. 8.1(d). Special attention would be given to a tilted angle of $\phi = 55°$ which is the transition between repulsive and attractive interaction.

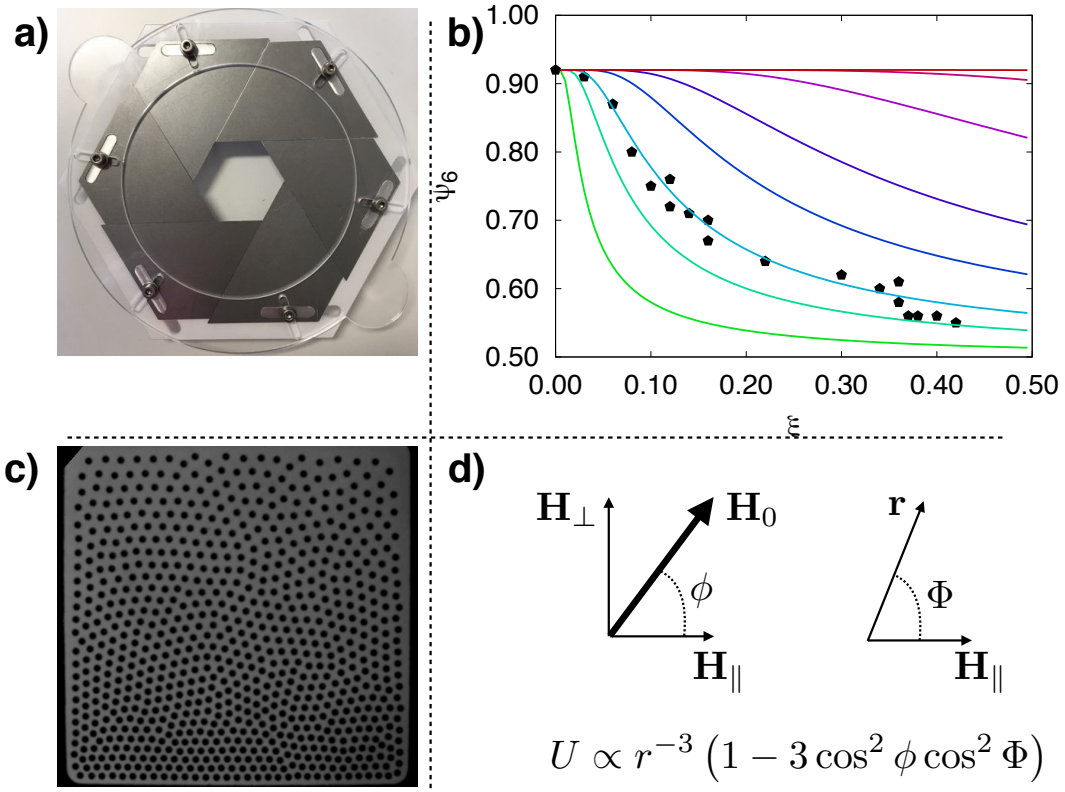

Figure 8.1 – a) Picture of the designed adjustable cell. b) Expected decay of the order with the rate of impurity for many dipolar ratios. From green to red, bead types become more similar. c) Snapshot of the tilted system. d) Schematic representation of the interaction anisotropy characterized by angles ϕ and Φ.

A Colloidal-granular similarities

R. Messina, S. Aljawhari, L. Bécu, J. Schockmel, G. Lumay and N. Vandewalle,
Quantitatively mimicking wet colloidal suspensions with dry granular media
Scientific Report **5**, 10348 (2015).

A.1 Introduction

As shown in Chapter 5, the key pictures of the KTHNY theory appear with our experiment model system. In a fruitful collaboration with René Messina, Sarah Aljawhari and Lydiane Bécu, we go further and show that structures observed in our granular experiment is quantitatively equivalent to those obtained in a magnetic colloidal suspension and with Monte Carlo simulations. From these, pair correlation functions $g(r)$ and orientational correlation functions $g_6(r)$ are confronted and an excellent quantitative agreement appears.

As the pair interaction is very similar for colloids and for magnetized beads, the crucial difference is that thermal fluctuations are negligible for granular materials. However, the remarkable property of our experiment to mimick Brownian motion (see Chapter 4) allows us to make a bridge between the average particle kinetic energy $\frac{1}{2}m\langle v^2\rangle$ and some effective temperature k_BT. Here, the link between colloidal and granular systems is made by using a common coupling parameter Γ

$$\frac{\langle U\rangle}{k_BT} = \Gamma = \frac{\langle U\rangle}{\frac{1}{2}m\langle v^2\rangle} \tag{A.1}$$

This parameter can therefore be measured in both colloidal and granular systems. Moreover, the magnetic coupling parameter Γ is also a natural input parameter in the numerical simulations.

A.2 Magnetic colloids

This part was entirely realized by the team of R. Messina. Superparamagnetic colloids of diameter 4.5 μm and mass density 1.7×10^3 kg/m^3 (Invitrogen) are dispersed in a Sodium Dodecyl Sulfate solution in order to prevent their aggregation. The suspension is filled in a cylindrical cell of diameter 5 mm glued on a glass slide. A 2D monolayer is obtained by the sedimentation of the particles on the glass/water interface. The large volume of water above the array of particles prevents any drift lead by the thermal gradient or disturbance of the air-water interface. The cell is then placed at the center of a coil in order to generate a magnetic field perpendicular to the glass-water interface. Thereby vertical magnetic moments in the particles are induced, leading to a repulsive pair potential perfectly equivalent to the pair potential between two of our magnetized beads. The particles are light enough to be submitted to thermal agitation and thus undergo Brownian motion. As temperature is kept constant in the experimental cell, the coupling parameter Γ is only tuned by playing with the magnetic field strength B. To reach the desired coupling parameter, the magnetic interaction is increased in small steps followed by an equilibration time of several hours. After equilibration the particles positions are determined using an inverted microscope equipped with a CCD camera. Typically, the field of view 560×480 μm^2 contains about 1400 particles.

A.3 Monte Carlo simulations

This part was entirely realized by the team of R. Messina. The Monte Carlo (MC) method is a generic name corresponding to a wide range of numerical simulation based on a repetition of random samples and takes its name from the famous Monte Carlo casino in Monaco. Here, the Metropolis algorithm [155] is used. First, the N particles are initialized in a given configuration. Then, each particle is successively moved randomly and the change in the total energy of the system ΔU is calculated. If the energy has decreased, the displacement is conserved, otherwise the displacement is only conserved with a probability $\exp(-\Delta U/k_B T)$. The MC simulation is carried out in the following configuration: a number of particles $N = 547$ and an area densityρ identical to the granular experiment, all confined in a hexagonal box. The constitutive particles are initially arranged as a perfect hexagonal lattice. The pair interaction is

$$\frac{U(r)}{k_B T} = \Gamma \left(\frac{1}{r\sqrt{\rho}} \right)^3 . \tag{A.2}$$

At equilibrium, $r\sqrt{\rho}$ reaches 1. Typically 10^6 MC steps are used to equilibrate the system and 10^6 additional MC steps are conducted to gather statistics for the computation of the required observables. It is carefully checked that upon starting with a perfect lattice or a fully randomly generated configuration, identical properties are obtained within the statistical uncertainties. This warranties that equilibrium is indeed reached.

A.4 Results

Comparative snapshots are displayed in Fig. A.1 for different values of the coupling parameter Γ. A first visual inspection shows qualitatively identical ordering in experiments and simulations at given Γ. As expected the ordering increases with Γ and a nearly perfect triangular lattice is recovered at the highest value of $\Gamma = 53.5$. This striking agreement is going to be analyzed now more quantitatively.

The first observable we consider to quantify the ordering is the pair distribution function $g(r)$ and is plotted in Fig. A.2 for different values of Γ.

To further investigate the ordering of the magnetized particles, we have monitored the bond-orientational function $g_6(r)$ The bond-orientational functions are plotted in Fig. A.3 for different values of Γ. At moderate coupling, good agreement between the three approaches (granular, colloidal, and simulated systems) is achieved. Upon increasing Γ, $g_6(r)$ increases and becomes close to unity at $\Gamma = 53.5$. Clearly, at high dipolar coupling (here $\Gamma = 41$ and $\Gamma = 53$) $g_6(r)$ tends to a constant in accordance with the KTHNY theory predicting (asymptotically) a constant value in the crystalline phase. For the lower values of Γ (here $\Gamma = 16.3$ and $\Gamma = 21$), it can be seen that $g_6(r)$ tends to decay algebraically. Following the KTHNY theory, this feature is a signature of the hexatic phase. Given the limited finite number of beads in the granular systems, a quantitative comparison with the KTHNY theory that holds for infinite systems is restricted.

Finally, let us remark that the coupling parameters Γ obtained with the granular experiment in Chapter 5 must be shifted up by 30% to ensure quantitative agreement with numerical simulations. This is probably due to a systematic error in the experimental measurement of Γ.

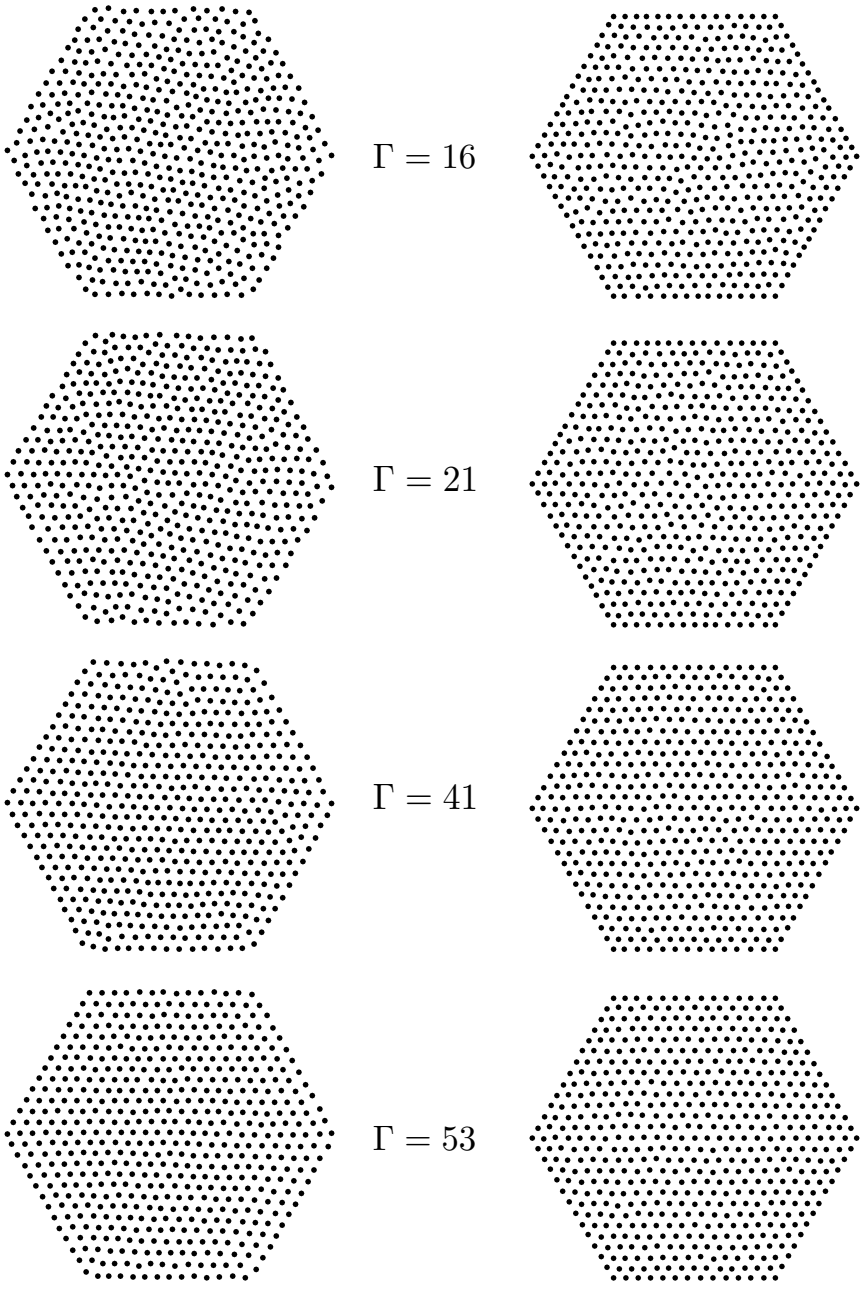

Figure A.1 – Representative microstructures of magnetic particles for two different values of the magnetic coupling parameter Γ. The left panel corresponds to experimental data, whereas the right one corresponds to simulation data.

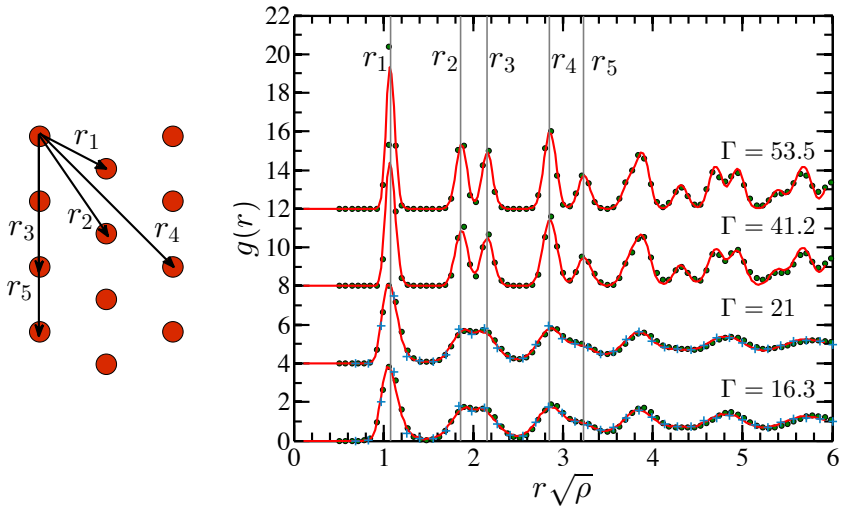

Figure A.2 – Pair distribution functions for different values of the magnetic coupling parameter Γ. Curves are shifted upwards upon increasing Γ (16, 21, 41, and 53). Full lines correspond to MC simulation data, whereas dots ($\bullet$) and stars ($*$) represent granular and colloidal experimental data, respectively. Vertical lines indicate the distances between nearest neighbors for a perfect triangular lattice as illustrated in the left panel. Thereby the shortest distance between two neighbors is given by $r_1 = \left(\frac{2}{\sqrt{3}}\right)^{1/2} \frac{1}{\sqrt{\rho}} \simeq 1.075 \frac{1}{\sqrt{\rho}}$. The other distances between further neighbors appear in the following sequence: $r_2 = \sqrt{3} r_1$, $r_3 = 2r_1$, $r_4 = \sqrt{7} r_1$, $r_5 = 3r_1$, and $r_6 = 2r_2 = 2\sqrt{3} r_1$.

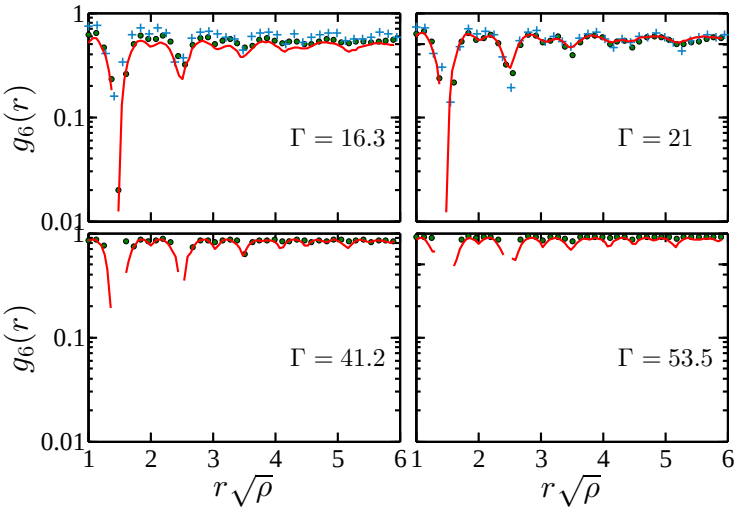

Figure A.3 – Bond-orientational correlation functions for different values of the magnetic coupling parameter Γ.

Bibliography

[1] H. M. Jaeger, S. R. Nagel and R. P. Behringer. *Granular solids, liquids and gases.* Rev. Mod. Phys. **68**, 1259 (1996).

[2] P. G. De Gennes. *Granular matter: a tentative view.* Rev. Mod. Phys. **71**, 374 (1999).

[3] G. Lumay, F. Boschini, K. Traina, S. Bontempi, J. C. Remy, R. Cloots and N. Vandewalle. *Measuring the flowing properties of powders and grains.* Powder Tech. **224**, 19 (2012).

[4] G. Lumay, J. Schockmel, N. Vandewalle and F. Boschini. *Method to measure the ability of a flowing powder to electrostatically charge and measurement device* (2014).

[5] G. Lumay, J. Schockmel, D. Hernandez-Enriquez, S. Dorbolo, N. Vandewalle and F. Pacheco-Vazquez. *Flow of magnetic repelling grains in a two-dimensional silo.* Papers in Physics **7**, 070013 (2015).

[6] A. Rescaglio, J. Schockmel, J. Vandewalle and G. Lumay. *Combined effect of moisture and electrostatic charges on powder flow.* EPJ Web of Conferences **140**, 13009 (2017).

[7] S. Aumaitre, R. Behringer, A. Cazaubiel, E. Clement, J. Crassous, D. Durian, E. Falcon, S. Fauve, D. Fischer, A. Garcimartin, Y. Garrabos, M. Hou, X. Jia, C. Lecoutre, S. Luding, D. Maza, M. Noirhomme, E. Opsomer, F. Palencia, T. Poschel, J. Schockmel, M. Sperl, R. Stannarius, N. Vandewalle and P. Yu. *An instrument for studying granular media in low-gravity environment.* Review of Scientific Instruments **89**, 075103 (2018).

[8] M. Noirhomme, A. Cazaubiel, A. Darras, E. Falcon, D. Fischer, Y. Garrabos, C. Lecoutre-Chabot, S. Merminod, E. Opsomer, F. Palencia, J. Schockmel, R. Stannarius and N. Vandewalle. *Threshold of gas-like to clustering transition in driven granular media in low-gravity environment.* EPL **123**, 14003 (2018).

[9] P. Bak, C. Tang and K. Wiesenfeld. *Self-organized criticality: An explanation of the 1/f noise*. Phys. Rev. Lett. **59**, 381 (1987).

[10] P. Bak, C. Tang and K. Wiesenfeld. *Self-organized criticality*. Phys. Rev. A **38**, 364 (1988).

[11] W. Clauss, A. Kittel, U. Rau, J. Parisi, J. Peinke and R. P. Huebener. *Self organized critical behaviour in the low temperature impact ionization breakdown*. EPL **12**, 423 (1990).

[12] G. Blatter, M. Feigel'Man, V. Geshkenbein, A. Larkin and V. Vinokur. *Vortices in high-temperature superconductors*. Rev. Mod. Phys. **66**, 1125 (1994).

[13] W. A. Moeur, P. K. Day, F.-C. Liu, S. T. P. Boyd, M. J. Adriaans and R. V. Duncan. *Observation of self-organized criticality near the superfluid transition in* ^{4}He. Phys. Rev. Lett. **78**, 2421 (1997).

[14] P. J. Cote and L. V. Meisel. *Self-organized criticality and the barkhausen effect*. Phys. Rev. Lett. **67**, 1334 (1991).

[15] J. S. Urbach, R. C. Madison and J. T. Markert. *Interface depinning, self-organized criticality, and the barkhausen effect*. Phys. Rev. Lett. **75**, 276 (1995).

[16] S. Hainzl, G. Zöller, J. Kurths and J. Zschau. *Seismic quiescence as an indicator for large earthquakes in a system of self-organized criticality*. Geophys. Res. Lett. **27**, 597 (2000).

[17] N. Vandewalle and N. Ausloos. *The robustness of self-organized criticality against extinctions in a tree-like model of evolution*. EPL **32**, 613 (1995).

[18] K. Linkenkaer-Hansen, V. Nikouline, J. Palva and R. Ilmoniemi. *Long-range temporal correlations and scaling behavior in human brain oscillations*. Int J Neurosci. **21**, 1370 (2001).

[19] H. M. Jaeger, C.-h. Liu and S. R. Nagel. *Relaxation at the angle of repose*. Phys. Rev. Lett. **62**, 40 (1989).

[20] V. Frette, K. Christensen, A. Malthe-Sorenssen, J. Feder, T. Jossang and P. Meakin. *Avalanche dynamics in a pile of rice*. Nature **379**, 49 (1996).

[21] T. A. J. Duke, G. C. Barker and A. Mehta. *A monte carlo study of granular relaxation*. EPL **13**, 19 (1990).

[22] K. Binder and J. Reger. *Theory of orientational glasses models, concepts, simulations.* Adv. Phys. **41**, 547 (1992).

[23] J. B. Knight, C. G. Fandrich, C. N. Lau, H. M. Jaeger and S. R. Nagel. *Density relaxation in a vibrated granular material.* Phys. Rev. E **51**, 3957 (1995).

[24] J. Berg and A. Mehta. *Glassy dynamics in granular compaction: Sand on random graphs.* Phys. Rev. E **65**, 031305 (2002).

[25] C. S. O'Hern, S. A. Langer, A. J. Liu and S. R. Nagel. *Force distributions near jamming and glass transitions.* Phys. Rev. Lett. **86**, 111 (2001).

[26] G. Marty and O. Dauchot. *Subdiffusion and cage effect in a sheared granular material.* Phys. Rev. Lett. **94**, 015701 (2005).

[27] O. Dauchot, G. Marty and G. Biroli. *Dynamical heterogeneity close to the jamming transition in a sheared granular material.* Phys. Rev. Lett. **95**, 265701 (2005).

[28] E. Facon, J.-C. Bacri and C. Laroche. *Equation of state of a granular gas homogeneously driven by particle rotations.* EPL **103**, 64004 (2013).

[29] J. S. Olafsen and J. S. Urbach. *Clustering, order, and collapse in a driven granular monolayer.* Phys. Rev. Lett. **81**, 4369 (1998).

[30] J. S. Olafsen and J. S. Urbach. *Velocity distributions and density fluctuations in a granular gas.* Phys. Rev. E **60**, R2468 (1999).

[31] W. Losert, D. Cooper, J. Delour, A. Kudrolli and J. Gollub. *Velocity statistics in excited granular media.* Chaos **9**, 689 (1999).

[32] F. Rouyer and N. Menon. *Velocity fluctuations in a homogeneous 2d granular gas in steady state.* Phys. Rev. Lett. **85**, 3676.

[33] P. M. Reis, R. A. Ingale and M. D. Shattuck. *Forcing independent velocity distributions in an experimental granular fluid.* Phys. Rev. E **75**, 051311 (2007).

[34] P. M. Reis, R. A. Ingale and M. D. Shattuck. *Caging dynamics in a granular fluid.* Phys. Rev. Lett. **98**, 188301 (2007).

[35] J. S. Olafsen and J. S. Urbach. *Two-dimensional melting far from equilibrium in a granular monolayer.* Phys. Rev. Lett. **95**, 098002 (2005).

[36] P. M. Reis, R. A. Ingale and M. D. Shattuck. *Crystallization of a quasi-two-dimensional granular fluid.* Phys. Rev. Lett. **96**, 258001 (2006).

[37] F. Moučka and I. Nezbeda. *Detection and characterization of structural changes in the hard-disk fluid under freezing and melting conditions.* Phys. Rev. Lett. **94**, 040601 (2005).

[38] A. S. Keys, A. R. Abate, S. C. Glotzer and D. J. Durian. *Measurement of growing dynamical length scales and prediction of the jamming transition in a granular material.* Nat. Phys. **3**, 260 (2007).

[39] A. Seguin and O. Dauchot. *Experimental evidence of the gardner phase in a granular glass.* Phys. Rev. Lett. **117**, 228001 (2016).

[40] T. Müller, D. de las Heras, I. Rehberg and K. Huang. *Ordering in granular-rod monolayers driven far from thermodynamic equilibrium.* Phys. Rev. E **91**, 062207 (2015).

[41] M. Gonzalez-Pinto, F. Borondo, Y. Martinez-Raton and E. Velasco. *Clustering in vibrated monolayers of granular rods.* Soft Matter **13**, 2571 (2017).

[42] K. Safford, Y. Kantor, M. Kardar and A. Kudrolli. *Structure and dynamics of vibrated granular chains: Comparison to equilibrium polymers.* Phys. Rev. E **79**, 061304 (2009).

[43] N. D. Mermin and H. Wagner. *Absence of ferromagnetism or antiferromagnetism in one- or two-dimensional isotropic heisenberg models.* Phys. Rev. Lett. **17**, 1133 (1966).

[44] N. D. Mermin. *Crystalline order in two dimensions.* Phys. Rev. **176**, 250 (1968).

[45] J. M. Kosterlitz and D. J. Thouless. *Ordering, metastability and phase transitions in two-dimensional systems.* J. Phys. C **6**, 1181 (1973).

[46] J. M. Kosterlitz. *The critical properties of the two-dimensional xy model.* J. Phys. C **7**, 1046 (1974).

[47] M. Chester, L. C. Yang and J. B. Stephens. *Quartz microbalance studies of an adsorbed helium film.* Phys. Rev. Lett. **29**, 211 (1972).

[48] D. J. Bishop and J. D. Reppy. *Study of the superfluid transition in two-dimensional* ^{4}He *films.* Phys. Rev. Lett. **40**, 1727 (1978).

[49] S. Stock, Z. Hadzibabic, B. Battelier, M. Cheneau and J. Dalibard. *Observation of phase defects in quasi-two-dimensional bose-einstein condensates.* Phys. Rev. Lett. **95**, 190403 (2005).

[50] D. J. Resnick, J. C. Garland, J. T. Boyd, S. Shoemaker and R. S. Newrock. *Kosterlitz-thouless transition in proximity-coupled superconducting arrays.* Phys. Rev. Lett. **47**, 1542 (1981).

[51] A. F. Hebard and A. T. Fiory. *Critical-exponent measurements of a two-dimensional superconductor.* Phys. Rev. Lett. **50**, 1603 (1983).

[52] C. C. Grimes and G. Adams. *Evidence for a liquid-to-crystal phase transition in a classical, two-dimensional sheet of electrons.* Phys. Rev. Lett. **42**, 795 (1979).

[53] J. F. Fernández, M. F. Ferreira and J. Stankiewicz. *Critical behavior of the two-dimensional xy model: A monte carlo simulation.* Phys. Rev. B **34**, 292 (1986).

[54] Q. M. Zhang and J. Z. Larese. *Melting of monolayer argon adsorbed on a graphite substrate.* Phys. Rev. B **43**, 938 (1991).

[55] E. Small, R. Pugatch and Y. Silberberg. *Berezinskii-kosterlitz-thouless crossover in a photonic lattice.* Phys. Rev. A **83**, 013806 (2011).

[56] B. I. Halperin and D. R. Nelson. *Theory of two-dimensional melting.* Phys. Rev. Lett. **41**, 121 (1978).

[57] D. R. Nelson and B. I. Halperin. *Dislocation-mediated melting in two dimensions.* Phys. Rev. B **19**, 2457 (1979).

[58] A. P. Young. *Melting and the vector coulomb gas in two dimensions.* Phys. Rev. B **19**, 1855 (1979).

[59] K. Zahn, R. Lenke and G. Maret. *Two-stage melting of paramagnetic colloidal crystals in two dimensions.* Phys. Rev. Lett. **82**, 2721 (1999).

[60] K. Zahn and G. Maret. *Dynamic criteria for melting in two dimensions.* Phys. Rev. Lett. **85**, 3656 (2000).

[61] H. H. von Grünberg, P. Keim, K. Zahn and G. Maret. *Elastic behavior of a two-dimensional crystal near melting.* Phys. Rev. Lett. **93**, 255703 (2004).

[62] C. Eisenmann, U. Gasser, P. Keim, G. Maret and H. H. von Grünberg. *Pair interaction of dislocations in two-dimensional crystals.* Phys. Rev. Lett. **95**, 185502 (2005).

[63] P. Keim, G. Maret and H. H. von Grünberg. *Frank's constant in the hexatic phase.* Phys. Rev. E **75**, 031402 (2007).

[64] U. Gasser, C. Eisenmann, G. Maret and P. Keim. *Melting of crystals in two dimensions.* ChemPhysChem **11**, 963 (2010).

[65] R. A. Segalman, A. Hexemer, R. C. Hayward and E. J. Kramer. *Ordering and melting of block copolymer spherical domains in 2 and 3 dimensions.* Macromolecules **36**, 3272 (2003).

[66] F. Boyer and E. Falcon. *Two-dimensional melting of a crystal of ferrofluid spikes.* Phys. Rev. Lett. **103**, 144501 (2009).

[67] J. Schockmel, E. Mersch, N. Vandewalle and G. Lumay. *Melting of a confined monolayer of magnetized beads.* Phys. Rev. E **87**, 062201 (2013).

[68] R. Messina, S. Aljawhari, L. Bécu, J. Schockmel, G. Lumay and N. Vandewalle. *Quantitatively mimicking wet colloidal suspensions with dry granular media.* Sci. Rep. **5**, 10348 (2015).

[69] K. S. Novoselov, A. K. Geim, S. V. Morozov, D. Jiang, Y. Zhang, S. V. Dubonos, I. V. Grigorieva and A. A. Firsov. *Electric field effect in atomically thin carbon films.* Science **306**, 666 (2004).

[70] A. H. Castro Neto, F. Guinea, N. M. R. Peres, K. S. Novoselov and A. K. Geim. *The electronic properties of graphene.* Rev. Mod. Phys. **81**, 109 (2009).

[71] L. Liu, M. Qing, Y. Wang and S. Chen. *Defects in graphene: Generation, healing, and their effects on the properties of graphene: A review.* J. Mater. Sci. **31**, 599 (2015).

[72] L. S. Hirst, A. Ossowski, M. Fraser, J. Geng, J. V. Selinger and R. L. B. Selinger. *Morphology transition in lipid vesicles due to in-plane order and topological defects.* PNAS **110**, 3242 (2013).

[73] Z. Song, V. I. Artyukhov, J. Wu, B. I. Yakobson and Z. Xu. *Defect-detriment to graphene strength is concealed by local probe: The topological and geometrical effects.* ACS Nano **9**, 401 (2015).

[74] Y. Yao, S. Wang, J. Bai and R. Wang. *Buckling of dislocation in graphene.* Physica E **84**, 340 (2016).

[75] C. Alba-Simionesco, B. Coasne, G. Dosseh, G. Dudziak, K. E. Gubbins, R. Radhakrishnan and M. Sliwinska-Bartkowiak. *Effects of confinement on freezing and melting.* J. Phys. Condens. Matter **18**, R15 (2006).

[76] E. Oguz, R. Messina and H. Löwen. *Crystalline multilayers of the confined yukawa system.* EPL **86** (2009).

[77] H. B. Eral, D. van den Ende, F. Mugele and M. H. G. Duits. *Influence of confinement by smooth and rough walls on particle dynamics in dense hard-sphere suspensions.* Phys. Rev. E **80**, 061403 (2009).

[78] A. Schella, A. Melzer, C. July and C. Bechinger. *Effect of confinement on the mode dynamics of dipole clusters.* Soft Matter **11**, 1197 (2015).

[79] K. Koga, G. Gao, H. Tanaka and X. Zeng. *Formation of ordered ice nanotubes inside carbon nanotubes.* Nature **412**, 802 (2001).

[80] R. Zangi and A. E. Mark. *Monolayer ice.* Phys. Rev. Lett. **91**, 025502 (2003).

[81] S. Han, M. Choi, P. Kumar and H. Stanley. *Phase transitions in confined water nanofilms.* Nat. Phys **6**, 685 (2010).

[82] G. Algara-Siller, O. Lehtinen, F. Wang, R. Nair, U. Kaiser, H. Wu, A. Geim and I. Grigorieva. *Square ice in graphene nanocapillaries.* Nature **519**, 443 (2015).

[83] M. Raju, A. Van Duin and M. Ihme. *Phase transitions of ordered ice in graphene nanocapillaries and carbon nanotubes.* Sci. Rep. **8**, 3851 (2018).

[84] A. Doostmohammadi, S. P. Thampi and J. M. Yeomans. *Defect-mediated morphologies in growing cell colonies.* Phys. Rev. Lett. **117**, 048102 (2016).

[85] J. Schockmel, N. Vandewalle, N. Opsomer and G. Lumay. *Frustrated crystallization of a monolayer beads under geometrical confinment.* Phys. Rev. E. **95**, 062120 (2017).

[86] P. N. Pusey, E. Zaccarelli, C. Valeriani, S. E, C. Wilson, K. Poon and M. E. Cates. *Hard spheres: crystallization and glass formation.* Phil. Trans. R. Soc. A **367**, 4993 (2009).

[87] A. Patwardhan. *Subpixel position measurement using 1d, 2d and 3d centroid algorithms with emphasis on applications in confocal microscopy.* âĂŐJ. Microsc **186**, 246 (1997).

[88] T. Li, S. Kheifets, D. Medellin and M. Raizen. *Measurement of the instantaneous velocity of a brownian particle.* Science **328**, 1673 (2010).

[89] M. Yaghoubi, M. Foulaadvand, A. Bérut and J. Luczka. *Energetics of a driven brownian harmonic oscillator.* J. Stat. Mech. Theory Exp. **2017**, 113206 (2017).

[90] S. Kheifets, A. Simha, K. Melin, T. Li and M. Raizen. *Observation of brownian motion in liquids at short times: Instantaneous velocity and memory loss.* Science **343**, 1493 (2014).

[91] J. M. Kosterlitz. *Nobel lecture: Topological defects and phase transitions.* Rev. Mod. Phys. **89**, 040501 (2017).

[92] S. C. Kapfer and W. Krauth. *Two-dimensional melting: From liquid-hexatic coexistence to continuous transitions.* Phys. Rev. Lett. **114**, 035702 (2015).

[93] A. H. Marcus and S. A. Rice. *Observations of first-order liquid-to-hexatic and hexatic-to-solid phase transitions in a confined colloid suspension.* Phys. Rev. Lett. **77**, 2577 (1996).

[94] A. Brodin, A. Nych, U. Ognysta, B. Lev, V. Nazarenko, M. Skarabot and I. Musevic. *Melting of 2d liquid crystal colloidal structure.* Condens. Matter Phys. **13**, 33601 (2010).

[95] P. Bladon and D. Frenkel. *Dislocation unbinding in dense two-dimensional crystals.* Phys. Rev. Lett. **74**, 2519 (1995).

[96] X. H. Zheng and R. Grieve. *Melting behavior of single two-dimensional crystal.* Phys. Rev. B **73**, 064205 (2006).

[97] M. Saint Jean, C. Guthmann and G. Coupier. *Relaxation and ordering processes in macroscopic wigner crystals.* Eur. Phys. J. B **39**, 61.

[98] L. Assoud, F. Ebert, P. Keim, R. Messina, G. Maret and H. Löwen. *Crystal nuclei and structural correlations in two-dimensional colloidal mixtures: experiment versus simulation.* J. Phys. Condens. Matter **21**, 464114 (2009).

[99] D. R. Nelson. *Phase Transition and Critical Phenomena.* Academic Press (1983).

[100] K. J. Strandburg. *Two-dimensional melting.* Rev. Mod. Phys. **60**, 161 (1988).

[101] R. Messina and H. Löwen. *Confined colloidal bilayers under shear: Steady state and relaxation back to equilibrium.* Phys. Rev. E **73**, 011405 (2006).

[102] G. Coupier, C. Guthmann, Y. Noat and M. Saint Jean. *Local symmetries and order-disorder transitions in small macroscopic wigner islands.* Phys. Rev. E **71**, 046105 (2005).

[103] F. Lindemann. Physica Z **7**, 609 (1910).

[104] V. M. Bedanov, G. Gadiyak and Y. Lozovik. *On a modified lindemann-like criterion for 2d melting.* Physics Letters A **109**, 289 (1985).

[105] C. A. Murray and D. H. Van Winkle. *Experimental observation of two-stage melting in a classical two-dimensional screened coulomb system.* Phys. Rev. Lett. **58**, 1200 (1987).

[106] Y. Tang, A. J. Armstrong, R. C. Mockler and W. J. O'Sullivan. *Free-expansion melting of a colloidal monolayer.* Phys. Rev. Lett. **62**, 2401 (1989).

[107] R. A. Quinn and J. Goree. *Experimental test of two-dimensional melting through disclination unbinding.* Phys. Rev. E **64**, 051404 (2001).

[108] M. J. Buehler. *Atomistic Modeling of Materials Failure.* Springer (2008).

[109] W. Y., W. J., Y. X., Y. R. and D. M. *The nature of strength enhancement and weakening by pentagon-heptagon defects in graphene.* Nature Mater. **11**, 759 (2012).

[110] R. Grantab, V. B. Shenoy and R. S. Ruoff. *Anomalous strength characteristics of tilt grain boundaries in graphene.* Science **330**, 946 (2010).

[111] O. Yazyev and S. Louie. *Electronic transport in polycrystalline graphene.* Nature Mat. **9**, 806 (2010).

[112] Z. Song, V. Artyukhov, B. Yakobson and Z. Xu. *Pseudo hall-petch strength reduction in polycrystalline graphene.* Nano Lett. **13**, 1829 (2013).

[113] A. R. Bausch, M. J. Bowick, A. Cacciuto, A. D. Dinsmore, M. F. Hsu, D. R. Nelson, M. G. Nikolaides, A. Travesset and D. A. Weitz. *Grain boundary scars and spherical crystallography.* Science **299**, 1716 (2003).

[114] W. Irvine, V. Vitelli and P. Chaikin. *Pleats in crystals on curved surfaces.* Nature **468**, 947 (2010).

[115] N. Garcia, A. Pezzutti, R. Register, D. Vega and L. Gomez. *Defect formation and coarsening in hexagonal 2d curved crystals.* Soft Matter **11**, 898 (2015).

[116] F. Jiménez, N. Stoop, R. Lagrange, J. Dunkel and P. M. Reis. *Curvature-controlled defect localization in elastic surface crystals.* Phys. Rev. Lett. **116**, 104301 (2016).

[117] E. H. Yong, D. R. Nelson and L. Mahadevan. *Elastic platonic shells.* Phys. Rev. Lett. **111**, 177801 (2013).

[118] L. J. Bonales, F. Martinez-Pedrero, M. A. Rubio, R. G. Rubio and F. Ortega. *Phase behavior of dense colloidal binary monolayers.* Langmuir **28**, 16555 (2012).

[119] Z. Yao and M. Olvera de la Cruz. *Polydispersity-driven topological defects as order-restoring excitations.* PNAS **111**, 5094 (2014).

[120] Y. Han, Y. Shokef, A. M. Alsayed, P. Yunker, T. C. Lubensky and A. G. Yodh. *Geometric frustration in buckled colloidal monolayers.* Nature **456**, 898 (2008).

[121] A. Radzvilavicius and E. Anisimovas. *Topological defect motifs in two-dimensional coulomb clusters.* J. Phys. Condens. Matter **23**, 385301 (2011).

[122] T. O. E. Skinner, H. M. Martin, D. G. A. L. Aarts and R. P. A. Dullens. *Frustrated crystallisation and melting in two-dimensional pentagonal confinement.* Soft Matter **9**, 10586 (2013).

[123] A. V. Filinov, M. Bonitz and Y. E. Lozovik. *Wigner crystallization in mesoscopic 2d electron systems.* Phys. Rev. Lett. **86**, 3851 (2001).

[124] M. Ishizuki, H. Takemiya, T. Okunishi, K. Takeda and K. Kusakabe. *Shape of polygonal quantum dots and ground-state instability in the spin polarization.* Phys. Rev. B **85**, 155316 (2012).

[125] Y. Sun, B. Mayers, T. Herricks and Y. Xia. *Polyol synthesis of uniform silver nanowires:âĂL a plausible growth mechanism and the supporting evidence.* Nano Lett. **3**, 955 (2003).

[126] M. Alcoutlabi and G. B. McKenna. *Effects of confinement on material behaviour at the nanometre size scale.* J. Phys. Condens. Matter **17**, R461 (2005).

[127] T. S. Ingebrigtsen, J. R. Errington, T. M. Truskett and J. C. Dyre. *Predicting how nanoconfinement changes the relaxation time of a supercooled liquid.* Phys. Rev. Lett. **111**, 235901 (2013).

[128] L.-W. Teng, P.-W. Tu and I. Lin. *Microscopic observation of confinement-induced layering and slow dynamics of dusty-plasma liquids in narrow channels.* Phys. Rev. Lett. **90**, 245004 (2003).

[129] K. Watanabe, T. Kawasaki and H. Tanaka. *Structural origin of enhanced slow dynamics near a wall in glass-forming systems.* Nature Mat. **10**, 512 (2011).

[130] M. Kong, B. Partoens and F. M. Peeters. *Topological defects and nonhomogeneous melting of large two-dimensional coulomb clusters.* Phys. Rev. E **67**, 021608 (2003).

[131] M. Kong, B. Partoens, A. Matulis and F. M. Peeters. *Structure and spectrum of two-dimensional clusters confined in a hard wall potential.* Phys. Rev. E **69**, 036412 (2004).

[132] Y.-J. Lai and I. Lin. *Defects and particle motions in the nonuniform melting of a two-dimensional coulomb cluster.* Phys. Rev. E **64**, 015601 (2001).

[133] V. M. Bedanov and F. M. Peeters. *Ordering and phase transitions of charged particles in a classical finite two-dimensional system.* Phys. Rev. B **49**, 2667 (1994).

[134] A. Koulakov and B. I. Shklovskii. *Charging spectrum and configurations of a wigner crystal island.* Phys. Rev. B **57**, 2352 (1998).

[135] R. Bubeck, S. Neser, C. Bechinger and P. Leiderer. *Structure and dynamics of two-dimensional colloidal crystals in confined geometry.* Adv. Colloid Interface Sci. **110**, 41 (1998).

[136] Z. Yao and M. Olvera de la Cruz. *Topological defects in flat geometry: The role of density inhomogeneity.* Phys. Rev. Lett. **111**, 115503 (2013).

[137] I. Williams, E. C. Oğuz, R. L. Jack, P. Bartlett, H. Löwen and C. P. Royall. *The effect of boundary adaptivity on hexagonal ordering and bistability in circularly confined quasi hard discs.* J. Chem. Phys. **140**, 104907 (2014).

[138] B. Delaunay. *Sur la sphère vide.* Bulletin de l'Académie des Sciences de l'URSS , 793 (1934).

[139] Z. Yao. *Topological vacancies in spherical crystals.* Soft Matter **13**, 5905 (2017).

[140] R. Peierls. *On ising's model of ferromagnetism.* Math. Proc. Camb. Philos. Soc. **32**, 477 (1936).

[141] D. N. Perera and P. Harrowell. *Stability and structure of a supercooled liquid mixture in two dimensions.* Phys. Rev. E **59**, 5721 (1999).

[142] H. König, R. Hund, K. Zahn and G. Maret. *Experimental realization of a model glass former in 2d.* The European Physical Journal E **18**, 287 (2005).

[143] M. Bayer, J. M. Brader, F. Ebert, M. Fuchs, E. Lange, G. Maret, R. Schilling, M. Sperl and J. P. Wittmer. *Dynamic glass transition in two dimensions.* Phys. Rev. E **76**, 011508 (2007).

[144] L. Assoud, R. Messina and H. Löwen. *Stable crystalline lattices in two-dimensional binary mixtures of dipolar particles.* EPL **80**, 48001 (2007).

[145] L. Assoud, R. Messina and H. Löwen. *Binary crystals in two-dimensional two-component yukawa mixtures.* J. Chem. Phys. **129**, 164511 (2008).

[146] P. Yunker, Z. Zhang and A. G. Yodh. *Observation of the disorder-induced crystal-to-glass transition.* Phys. Rev. Lett. **104**, 015701 (2010).

[147] A. Pertsinidis and X. S. Ling. *Diffusion of point defects in two-dimensional colloidal crystals.* Nature **413**, 147 (2001).

[148] W. T. M. Irvine, A. D. Hollingsworth, D. G. Grier and P. M. Chaikin. *Dislocation reactions, grain boundaries, and irreversibility in two-dimensional lattices using topological tweezers.* PNAS **110**, 15554 (2013).

[149] Z. Yao and M. Olvera de la Cruz. *Dynamics of vacancies in two-dimensional lennard-jones crystals.* Phys. Rev. E. **90**, 062318 (2014).

[150] A. T. Pham, R. Seto, J. Schönke, D. Y. Joh, A. Chilkoti, E. Fried and B. B. Yellen. *Crystallization kinetics of binary colloidal monolayers.* Soft Matter **12**, 7735 (2016).

[151] M. Antlanger, M. Mazars, L. Samaj, G. Kahl and E. Trizac. *Taking one charge off a two-dimensional wigner crystal.* Mol. Phys. **112**, 1336 (2014).

[152] F. Rothen and P. Pieranski. *Mechanical equilibrium of conformal crystals.* Phys. Rev. E **53**, 2828 (1996).

[153] V. Soni, L. R. Gómez and W. T. M. Irvine. *Emergent geometry of inhomogeneous planar crystals.* Phys. Rev. X **8**, 011039 (2018).

[154] V. A. Froltsov, R. Blaak, C. N. Likos and H. Löwen. *Crystal structures of two-dimensional magnetic colloids in tilted external magnetic fields.* Phys. Rev. E **68**, 061406 (2003).

[155] N. Metropolis, A. Rosenbluth, M. Rosenbluth, A. Teller and E. Teller. *Equation of state calculations by fast computing machines.* J. Chem. Phys. **21**, 1087 (1953).